Title
A Global Finite Element Reverse Approach for Identifying the Material Elasticity and Current State of Stress

Author
Tartibi, Mehrzad

Publication Date
2015

Peer reviewed|Thesis/dissertation

A Global Finite Element Reverse Approach for Identifying the Material Elasticity and Current State of Stress

by

Mehrzad Tartibi

A dissertation submitted in partial satisfaction of the

requirements for the degree of

Doctor of Philosophy

in

Engineering – Mechanical Engineering

and the Designated Emphasis
in

Computational Science and Engineering

in the

Graduate Division

of the

University of California, Berkeley

Committee in charge:

Professor Kyriakos Komvopoulos, Co-chair
Professor David J. Steigmann, Co-chair
Professor Tarek I. Zohdi
Professor Mohammad Mofrad

Spring 2015

A Global Finite Element Reverse Approach for Identifying the Material Elasticity and Current State of Stress

Abstract

A Global Finite Element Reverse Approach for Identifying the Material Elasticity and Current State of Stress

by

Mehrzad Tartibi

Doctor of Philosophy in Engineering – Mechanical Engineering
and the Designated Emphasis
in
Computational Science and Engineering

University of California, Berkeley

Professor Kyriakos Komvopoulos, Co-chair

Professor David J. Steigmann, Co-chair

The mechanical response of solids exhibiting complex material behavior has traditionally been determined by fitting constitutive models of specified functional form to experimentally derived force-displacement (stress-strain) data. However, characterizing the nonlinear mechanical behavior of complex materials requires a method of quantifying material behavior that is not restricted by a specific constitutive relation. To this end, a new method, termed *the reverse updated Lagrangian finite element method* (RULFEM), which is based on the three-dimensional displacement field of the deformed solid and finite element method, is developed for incrementally linear materials. In RULEFM, the body is discretized by finite elements and its material properties are determined element-wise, i.e., the properties are assumed to be uniform at the element level and may vary from one element to another. The validity of RULFEM is demonstrated by three noise-free numerical examples and three numerical examples with various input noise levels. Two methods to assess the global and local errors of the results due to error in the measured input data (noisy data) are also discussed.

The life expectancy of a solid is traditionally predicted by assessing its expected stress cycle and comparing it to the experimentally determined stress state at failure. The accuracy of this procedure is often compromised by unforeseen extremes in the loading cycle or progressive material degradation. Often residually stressed part can either produce longer or shorter lifespans than predicted. Thus determination of the current state of stress (i.e., the residual stress in the absence of external loading) and material properties is particularly important. Typically, the material properties of a solid are determined by fitting the experimental data collected from the measured response to deformations of a stress-free configuration. However, the characterization of the mechanical behavior of a residually stressed body requires, in principle, a method that is not restricted to specific constitutive models. Complementing RULFEM [28], a new method, called *estimating*

the current-state-of-stress (ECSS) is developed in this work. Similar to RULFEM, ECSS also uses as input three-dimensional full-field displacement and force data of the body, which is perturbed by small displacements. ECSS complements the first step of the incremental RULFEM method. It generates the nodal current-state-of-stress (or residual stress in the absence of external tractions) as well as the incremental elasticity tensor pertaining to each of the finite elements used to discretize the body. The ECSS method is used to simulate two noise-free examples.

The linear dynamic response of a solid body has been used for material identification and even defect detection in low-damping (negligible viscoelastic behavior) materials. RULFEM and ECSS input full-field data, obtained from the statically perturbed body, are used to determine the initial state of stress and the current material elasticity tensors. A new formulation of ECSS, called *dynamically estimating residual stress* (DERS) is developed in the fifth chapter of this dissertation. This is based on three-dimensional full-field displacement and force data of the dynamically perturbed body. In addition to nodal residual stress tensors and element-wise incremental elasticity tensor, DRES generates element-wise material density of the discretized body.

To my parents (Talieh Yousefiani and Mohammad Tartibi)

Also to my lovely fiancée and to my supportive sister and brothers

Contents

List of Figures

List of Tables

Nomenclature

$\bar{\mathbf{p}}$	The first Piola boundary traction force applied at reference configuration (referential boundary traction)
$\mathbb{C}$	The fourth-order material elasticity tensor
$\mathbb{L}$	The fourth-order material incremental elasticity tensor
β_i	The ith component condition number
$\mathbf{a}$	Material point acceleration
$\mathbf{E}_{AB}$	component AB of the symmetric part of the deformation gradient tensor $\mathbf{H}$
$\mathbf{F}$	The deformation gradient tensor $\mathbf{F} = \mathbf{I} + \mathbf{H}$
$\mathbf{G}$	The global geometrical mass matrix with decoupled elemental mass density
$\mathbf{H}$	the special deformation gradient tensor
$\mathbf{n}$	Exterior unit normal at current configuration
$\mathbf{P}$	The first Piola-Kirchoff stress tensor
$\mathbf{S}_{AB}$	Component AB of the second Piola-Kirchoff stress tensor
$\mathbf{T}_n^n$	Cauchy stress tensor at Configuration R_n
$\mathbf{u}_{n+1}^n$	Displacement vector at configuration R_{n+1} with respect to configuration R_n
$\mathbf{W}$	The skew-symmetric deformation gradient tensor
$\mathbf{X}$	The position vector of a material point at configuration R_0
$\mathbf{x}_n$	The position vector of a material point at configuration R_n
$\mathbf{Y}$	The global geometrical stiffness matrix caused by Cauchy stress tensor on the solid body surface

$\mathbf{Z}$ The global geometrical stiffness matrix caused by Cauchy stress tensor within the solid body

$[\mathbf{B}^e]$ The shape function differential operator

γ_{q0} Region of the boundary at current configuration R_0 that current traction force field $\mathring{\mathbf{t}}$ is applied

Γ_{qn} Region of the boundary at reference configuration R_0 that traction force field $\bar{\mathbf{p}}$ is applied

γ_{qn} region of the boundary at current configuration R_n that current traction force field $\mathbf{t}_n$ is applied

Γ_{un} Region of the boundary at reference configuration R_0 that displacement boundary condition $\bar{\mathbf{u}}$ is applied

$\mathring{\mathbf{b}}$ Initial body force field

$\mathring{\mathbf{S}}$ The second Piola-Kirchoff stress tensor at configuration R_0

$\mathring{\mathbf{T}}$ Initial Cauchy stress tensor

$\mathring{\mathbf{t}}$ Initial surface traction

$\{\mathbf{f}\}$ Nodal force vector

$\{\mathbf{u}\}$ Nodal displacement vector

$[\mathbf{A}]$ The global geometry stiffness times displacement vector function differential operator

$[\mathbf{K}]$ The global stiffness matrix

$[\mathbf{M}]$ The global mass matrix

$\left[\hat{\mathbf{\Psi}}\right]$ The global vector of stiffness of general form of stiffness operated on displacement vector $\mathbf{u}$

Ω A given name to a solid body

ω Excitation angular velocity

ρ Material mas density

$[\boldsymbol{\phi}^e]$ The FEA shape function matrix

dA_n Area element at configuration R_n

dV_n Volume element at configuration R_n

E^i_{loc} The local error defined for element-wise elasticity tensor prediction

J Jacobian of the deformation gradient tensor $\mathbf{F}$, $J = det\,(\mathbf{F})$

R_n Configuration name of a solid body at time t_n

r_{n+1} Linear momentum residual

Acknowledgments

I would like to thank so many people that have helped me in various ways throughout my graduate education. From my dear engineering manager in Siemens Power Generation, Dr. Hans-Juergen Kiesow, who encouraged me in continuing education, to the faculties teaching the courses, in particular Professor Stanley Burger, who word of encouragement rings in my head all the time, to the campus staff members who kept me and my paperwork on track. From my labmates to my classmates, the diverse group of people who made up my peers on campus helped me through difficult homework assignments, difficult research problems, and made my day-to-day experience at UC Berkeley much richer and more fulfilling than I have ever experienced in my lifetime.

I would especially like to thank my advisors, Professor Kyriakos Komvopoulos and Professor David Steigmann. Not only did they walked me through difficult personal life experiences, but they helped direct my efforts toward the important issues and academic goals. They taught me how to reduce difficult problems to more tractable one, and patiently seek proper solutions. They have always gave me confidence by treating and comparing my work with work of leading scientists in my field. They were not afraid to get their hands dirty and helped validating my computer codes, my manuscripts and my messy equations. They taught me all I know about what constitute a journal quality paper. But most of all they taught me the most important characteristics of a world-class university professor, i.e. to be humble, knowledgeable, kind and treat students with respect!

I particularly would like to thank my committee members, Professors Taroek Zohdi and Mohammad Mofrad, who have always believed in me and given me the best advice and directions both on my education at UC Berkeley and on my future carrier.

I would also like to thank our collaborators and lab-mates, who trained me in handling live cells and conducting fascinating experiments, namely: Professor Song Li, Professor Gang-yu Liu, Julia Chu (lab manager), and my fellow graduate students Ying Liu, Cheng Quin, Juan Pu, and Christopher Zimmer,

I would never forger my dear lab-mates and classmates, Zhichao Song, Huaming Xu, Taekwon Jee, Kenneth Lee, Pedram Hassanzadeh, Giorgio T. De Vera, and Sayna Ebrahimi, who helped me throughout my education collaborating in solving tough homework assignments and software tools and techniques, and writing my dissertation in LaTex.

My parents (Taliehd Yousefiani and Mohammad Tartibi), my siblings (Mohsen, Masoud, Mahnaz, Manoochehr and Mehrdad) and my close friends (Reza Rahimi, Babak Soltanian, Saleh Refaee and Dalileh Alaie), always provided so much support and encouragement. Their love and well-wishes kept me going much of the time.

And finally, many thanks to my loveliest fiancée, Hengameh Shams, who has believed in me the most and has been very patient with me. Also to her lovely parents (Nahid Alaie and Professor Yaha Shams) who has treated me and supported me as their own son. Hengaeh filled my heart with love, kept a smile on my face and a fire under my rear end to finish up my dissertation.

Chapter 1

Introduction

1.1 Motivation

Under what external forces does a solid part fail? What is the consequence of this failure? A vast amount of effort and resources are continuously spend to address these questions. Maximum principle stress and, von Mises criteria are among the most commonly used material failure criteria, where material fracture and yielding are commonly assessed by components of local stress tensors. Hence, stress field determination is essential. The linear momentum balance equation relates the applied forces, such as body, inertia, and surface traction, with the divergence of the stress tensor. A material constitutive model, relating stress and strain, allows solving for the displacement field and, in turn, the stresses throughout the body. Such constitutive material models are typically defined based on the experimental response of the material. Isotropic linear elastic, orthotropic, and anisotropic, are common material models. A more recent class of constitutive models, known as hyperelastic, relates stress with a material strain-energy function. To this end, defined constitutive models are incapable of determining the *current-state-of-stress (CSS)* (in particular known as *residual stress* in the absence of external loading) in a solid body. High demand for more durable, sophisticated and reliable parts has motivated the use of more complex material design, geometry, manufacturing processes and unknown loading cycle. Despite development of advanced numerical methods, such as finite element analysis, finite difference, and boundary elements, estimating the stress field in solid bodies is a challenging task. Extraction of accurate material models from standard experimental procedures does not guarantee accurate prediction of stress tensors in the actual part, or estimation of the stresses experienced by the body during manufacturing. Critical machinery solid components, such as plane and jet engine parts, are tested under the harshest loading cycles. Though, such prototype testings validate the failure criteria and provide some durability measures, they are incapable of measuring the induced stresses due to manufacturing processes and justifying statistical variations. As a result, often unrealistic safety factors are introduced to assure safe operation of the part. To minimize these safety factors and because of skyrocketing prototype testing costs, mathematical models to extract both local material constitutive models and stress tensor fields from prototype testing, or standard testing of complex composite materials must

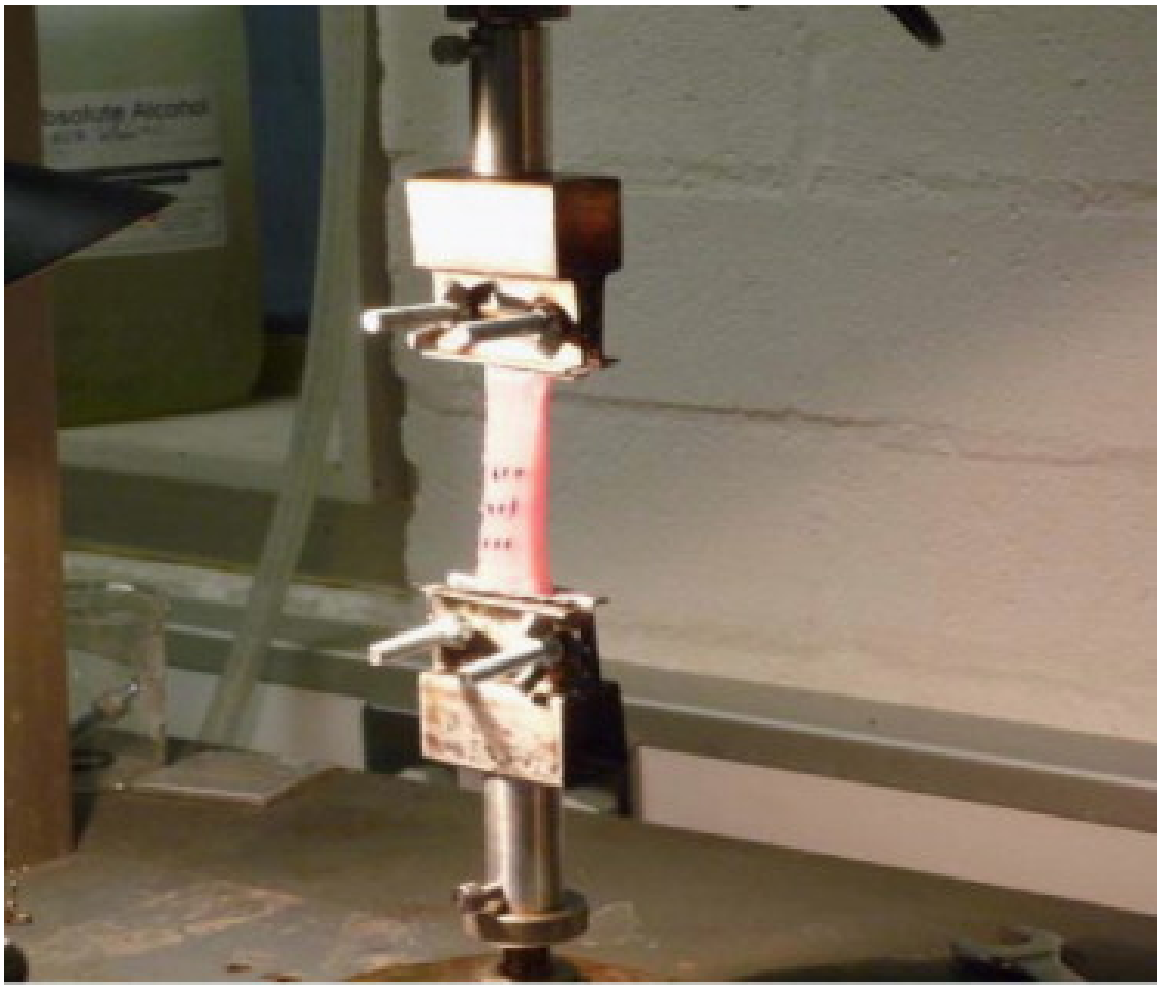

Figure 1.1: A uniaxial tensile experiment setup with specimen made of fresh Longissimus dorsi skeletal muscle tissue harvested from three month old female pigs [27].

be developed.

Mechanical capabilities and, hence, mechanical properties of many types of soft tissue affect their physiological functions. For instance the mechanical properties of healthy arteries, myocardium, tendon, ligament, and skin tissues may differ from those of unhealthy tissues. Muscle tissues are directional viscoelastic solids with nonlinear behavior in its fiber directions. Takaza et al. [27] suggested an anisotropic material model for muscle tissues. The muscle specimens were uniaxially stretched from their assumed stress-free configurations Fig. 1.1. The computed stress assumed uniform fibrous distribution throughout the specimen cross section and specimens with different fiber directions were tested. Though this study produced interesting and useful results, heterogeneity in biological tissues and the assumptions involved in this study limit the use of the applied methodology to other muscular tissues. Moreover, the stress-free condition is not fully proven to be the case in many tissues in the body.

Vaishnav and Vossoughi (1987) [30] were the first to study the existence of residual stresses in soft tissues. Many advanced hyperelastic type material constitutive models do not take into account residual stresses organs and tissues, such as myocardium and aorta [12], although residual stresses have been considered in a few studies [32].

Holzaphel and Ogden (2009) [13] conducted a thorough hybrid study measuring residual stress in the three layers of arteries (i.e., intima, media, and adventitia). The longitudinal and cylindrical slices of the artery were measured before and after cutting. Each layer was treated as a uniform material following an incompressible isotropic material constitutive model. From the measured dimensions and based on assumptions, the residual stresses throughout each layer were computed. This destructive residual stress measurement technique is known as the slicing technique, originally employed for metallic parts [24]. The heterogeneity, assumptions involved in this study, *in vitro* specimen condition, and destructive nature of this method motivate the development of nondestructive methods without any assumptions, which are purely based on measured data.

1.2 Material Identification Techniques

Accurate determination of material properties used in mathematical models is critical to the calculation of the stress and strain fields in solids of various shapes subjected to loadings more complex than those used in standardized mechanical tests. According to established standards and testing protocols, material parameters are usually extracted from experimental measurements using closed-form solutions for simple tests, such as uniaxial tension and four-point bending. The measured quantities are typically global forces and displacements, with local stress-strain fields assumed to be uniform through the gauge section of the specimen. The underlying assumption in this traditional approach is that the effect of the specimen geometry on the measured material properties is insignificant; however, this ideal situation is not always representative of the true material behavior. For example, the machining process required to produce a part with the desired shape may significantly affect the material properties. Moreover, standardized tests accounting for intrinsically heterogeneous or nonlinear behavior (e.g., biomaterials, nanocomposites, and rubbery materials) and changes in the material properties due to extrinsic factors (e.g., fabrication, environment, and aging) are lacking. Thus, it is necessary to introduce more sophisticated methods for determining the material response under real loading and environmental conditions.

Progress in imaging technology has minimized the need for standardized tests. The increased interest in localized material behavior has led to the development of several hybrid methods, which are based either on full-field or boundary-displacement measurements and use various numerical schemes to solve the continuum-based equations (i.e., balance of linear and angular momentum) and then determine the unknown material parameters. Traditional numerical techniques, such as the finite element method (FEM) and boundary element method, provide stress and strain fields for a given body force and set of boundary conditions, using constitutive relations with set material parameters. Hence, determination of material parameters requires the solution of an inverse problem. Inverse formulations for quasi-static linear elasticity with small perturbations can be grouped in five major categories [1]: (1) FEM updating method (FEMU), (2) constitutive equation

gap method (CEGM), (3) virtual field method (VFM), (4) equilibrium gap method (EGM), and (5) reciprocity gap method (RGM). The governing equations in these methods are derived from the balance of linear momentum, the principle of virtual work, the Maxwell–Betti reciprocity principle, and the total potential energy principle, using standard numerical techniques, such as the FEM and finite differences method.

FEMU compares either the measured applied force field (FEMU-F method) or the measured displacement field (FEMU-U method) with the corresponding predicted fields calculated by FEM for a set of updated material parameters. Both FEMU-F and FEMU-U formulations are based on the minimization of a scalar cost function obtained by applying a positive definite symmetric weighting matrix to the difference vector of measured and calculated quantities. FEMU-F requires full-field measurements, whereas FEMU-U requires only partially measured fields. Application of FEMU has been confined to cases where material behavior is known *a priori*. The unknown material parameters are then found by minimization of cost functions using the Gauss-Newton or Levenberg–Marquardt methods for small or moderate problems and global optimization methods (e.g., evolutionary algorithms) for larger problems. FEMU-U has been used to determine the material parameters of bodies consisting of linearly elastic, anisotropic, orthotropic, elastic- plastic, viscoelastic, and hyperelastic materials [1, 21].

CEGM is similar to FEMU. This method uses optimization functions to either implicitly or explicitly compare measured with calculated fields. This comparison (referred to as the gap) measures the distance between an assumed stress field through the body and a stress field obtained for a given constitutive model and full-field displacement measurement. Two types of cost functions are typically defined: one that minimizes the stress field gap through the entire body, which can yield at most three local material parameters per mesh discretization, and another function that minimizes a weighted norm of the difference of measured and calculated displacement fields, which is based on *a priori* assumed constitutive models [1, 2, 10]. Ladevèze et al. (1994) [18] performed vibrational experiments to measure the displacement field and minimized a cost function relating stress to displacement.

VFM relies on full-field displacement measurements to provide the strain field of the deformed body. Unlike FEMU and CEGM, this method does not depend on the solution of a minimization function to determine the material parameters of a chosen constitutive model. Instead, a set of linearly independent equations is constructed, which are equal to the unknown material parameters. Each of these equations requires a virtual displacement field and can only be obtained if the fourth-order elasticity tensor is a linear function of the material parameters in order for the latter to be decoupled from the geometrical parameters. Several methods have been developed to generate virtual displacement fields yielding linearly independent equations. VFM applications to parameter identification of constitutive equations include linear isotropic and anisotropic elasticity, nonlinear anisotropic elasticity, viscoelasticity, and elastic-plastic deformation [1, 10, 9].

EGM estimates the damage in a body in terms of one elastic material parameter, which is a function of position and decoupled from the stiffness matrix. This method also relies on the minimization of a cost function to find the local material parameter and is a special case of VFM because it uses full-field displacement measurements as an input. Therefore, EGM exhibits the same drawbacks as VFM [1, 10].

RGM relies on measured displacements and boundary tractions. In this method, a reciprocity gap function is defined from the principle of virtual work using the Maxwell–Betti reciprocity theorem, which requires the comparison of the actual state of unknown material parameters (based on *a priori* assumed constitutive model and measured boundary displacement and traction fields) and adjoint state (obtained from fictitious material parameters and a known perturbation) that yields the corresponding displacement and force fields. The constructed functional is then solved for the unknown material parameters and the interior displacement field. RGM can be regarded as a variation of VFM. However, because there is no method for extrapolating the displacement field from known boundary values, the RGM method discussed here has not been applied to material parameter identification [1, 16].

A central commonality among the aforementioned material identification methods is the *a priori* assumption of a constitutive model and the use of a numerical analysis of mechanical balance laws. Although these methods provide useful material parameter identification approaches, modeling assumptions imposed in the case of unknown or damaged materials entail a high degree of subjectivity and may yield biased results. All of the above mentioned methods rely on assumptions about the constitutive relation that may not be optimum for the material under given conditions. Moreover, none of the existing methods provides a means of estimating the overall error. In fact, a systematic methodology to assess the selection of the constitutive model and the error in the predicted parameters due to measurement errors has yet to be developed.

One of the objectives of this dissertation is to introduce a method that provides a reasonably general framework for material identification problems without *a priori* assumptions about the constitutive equations, provided the response exhibits incremental linearity (Chapter 3). The present method solves an inverse problem and is based on the updated Lagrangian form of FEM; therefore, it is referred to as the reverse updated Lagrangian finite element method (RULFEM). Similar to most existing methods, RULFEM relies on FEM and full-field displacement measurements. However, it does not require *a priori* constitutive assumptions. Instead, it directly yields the tangent elasticity tensor of each finite element. Because RULFEM generates a coefficient matrix of a linear system of equations, which may have a high condition number, a small random error in the nodal displacement measurements and/or traction vectors may generate erroneous results. Small measurement errors are inevitable even with high-resolution imaging; thus significant errors may occur in the solution of the inverse problem. However, the solution error can be assessed and bounded by errors in the input measured vector fields. The presentation of the RULFEM theory is accompanied by an implementation section where RULFEM is used to determine elasticity tensors. Both noise-free (theoretical) and noisy (actual) measured displacement and force fields are used in numerical examples to validate RULFEM method. In addition, the capability of RULFEM is evaluated by numerical tools for calculating upper-bound errors.

1.3 Residual Stress Measurement Techniques

An objective in material selection is to ensure that a part will withstand a known loading cycle. This aim cannot always be achieved by using material properties deduced from established stan-

dards and testing protocols. Thus, prototype testing is often conducted to account for the unknown effects of material processing, material handling, manufacturing processes, assembly processes, and, most importantly, unknown loading distributions, magnitudes, and cycles. Such uncontrollable effects are normally taken into consideration at the design stage by using empirical safety factors. Accurate life prediction of an existing or new design depends primarily on knowledge of (1) thermo-mechanical properties, (2) actual loading cycles, (3) current state of stress within the body, and (4) stress or strain history. It is often not possible to measure, compute, and/or predict (2) and (4), or to measure (1) and (3) throughout the body by nondestructively means. Thus, it is necessary to introduce more sophisticated methods to determine the material response and the current state of stress under real loading and environmental conditions.

Finite element analysis (FEA) is the most popular numerical method for computing stress fields in solids. The efficacy of FEA depends strongly on constitutive models, loading conditions, and the presumed state of stress at the selected reference configuration. Regardless of the method used, life predictions can be compromised if the considered part undergoes unknown loading cycles, if erroneous constitutive models are used, or if the residual state of stress is unknown. For example, typical manufacturing processes, in particular welding and cold working, can affect the constitutive material behavior via a self-equilibrated state of residual stress. This can either ameliorate or exacerbate the overall stress condition; in the latter case, failure may occur earlier than predicted. More complicated examples are biological tissues, such as arteries and heart tissue, in which constitutive models are derived from *in vitro* experiments wherein the unstressed configurations, if any, are unknown.

Withers et al. [34, 35] and more recently Rossini et al. [24] have grouped residual stress measurement techniques into destructive and nondestructive (Fig. 1.2). Some techniques are applicable to actual parts and others only to experimental specimens, such as cutouts, mock-ups and test pieces. Destructive techniques can provide the local strains responsible for local stresses by the controlled removal of material from the surface of the part, or by slicing and cutting the part into pieces. Nondestructive techniques typically furnish physical parameters that are related to the residual stress. Moreover, residual stresses can be classified into macro- and microscopic stresses, with both types possibly existing in a part [24]. Macroscopic residual stresses are operative on a scale larger than the grain size of the material, whereas microscopic residual stresses are operative on the scale of a material grain or within a grain and are attributable to the presence of dislocations or crystalline defects (Fig. 1.3).

Destructive measurement techniques, also referred to as mechanical techniques, are further categorized into semi-destructive and destructive methods [24]. The more common of these methods are: (1) hole drilling method (HDM), a semi destructive method, which provides the residual stress distribution in a specimen by fast or gradual removal of material at the center of a strain-gauge rosette (Fig. 1.3) ; (2) ring-core method (RCM), a semi destructive method. This is an "inside-out" version of HDM, wherein the deformation of the central region of a ring is measured while an annular slot in the perimeter is being made; (3) deep hole method (DHM), a semi destructive method, which is performed by first drilling through the thickness of the component and then measuring the hole diameter accurately. The residual stresses in the core are relaxed when the material is trepanned out, permitting the measurement of deep interior stresses; (4) sectioning

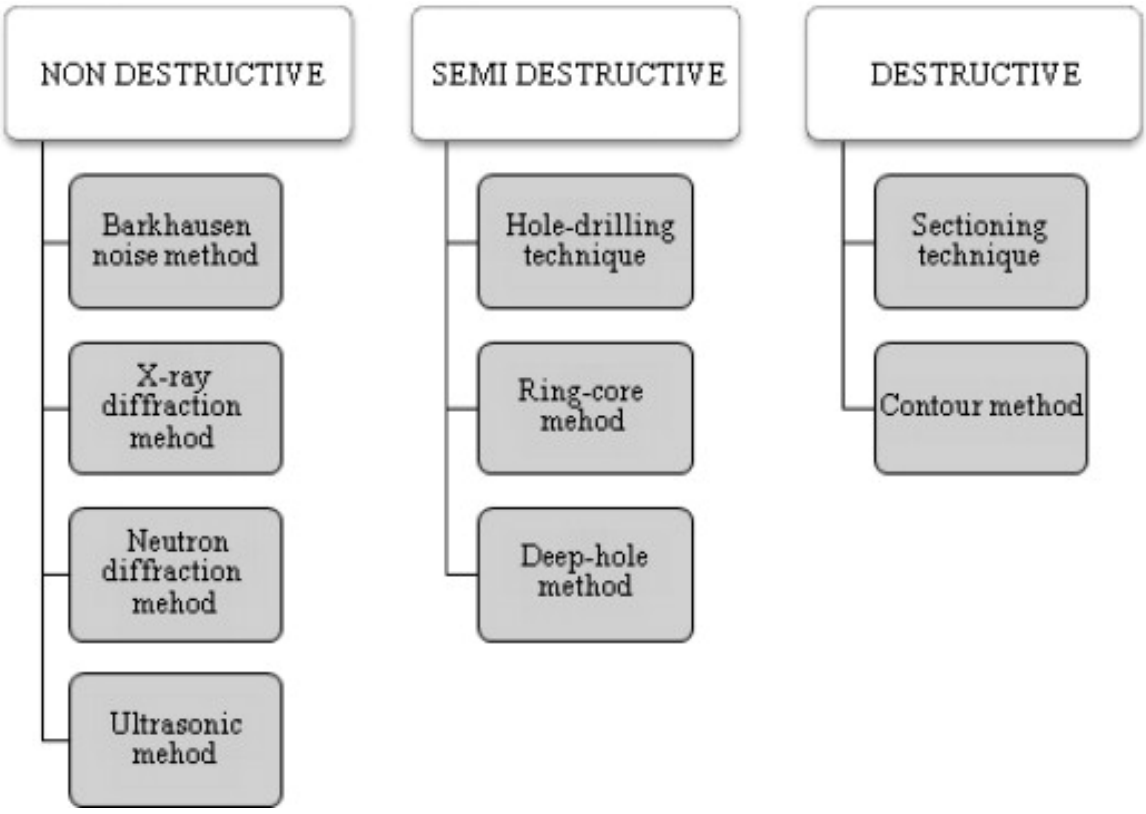

Figure 1.2: Residual stresses measuring techniques [24].

technique (ST), a destructive method in which the part is sectioned to release the residual stresses through the cutting line. The axial deformation and curvature of the cut strip reveal the membrane and bending (through thickness) residual stresses (Fig. 1.5); and (5) contour method (CM), a recently invented four-step destructive technique (specimen cut, contour measurement, data reduction, and stress analysis) that produces a 2D stress map on a cut plane (Fig. 1.6). These methods have been mainly developed to estimate residual stresses in metallic components. However, ST has been applied to biological tissues, in particular to arteries, heart tissue, etc. [17, 23, 32, 12, 31].

Some of the nondestructive techniques entail the measurement of the elastic strain of atomic lattice planes. One of the oldest techniques, X-ray diffraction, yields data only up to 5 μm below the surface of a specimen. For deeper measurement, neutron diffraction has traditionally been adopted [14]. More advanced neutron diffraction techniques are capable of probing up to 50 mm of steel specimen [7]. Some other techniques take advantage of the influence of stress on the magnetic properties of the material [15, 5]. While others monitor the influence of stress on conductivity (eddy current) [4], acoustic sound speed [8], etc. Despite their vast applications, nondestructive techniques are limited for measuring stresses in thick parts. For example, neutron diffraction yields data to a maximum depth of 10 cm [24] (Fig. 1.7).

Nondestructive techniques require a calibration step prior to use; consequently, their accuracy is material dependent. Typically a material parameter is related to the virgin mechanical properties

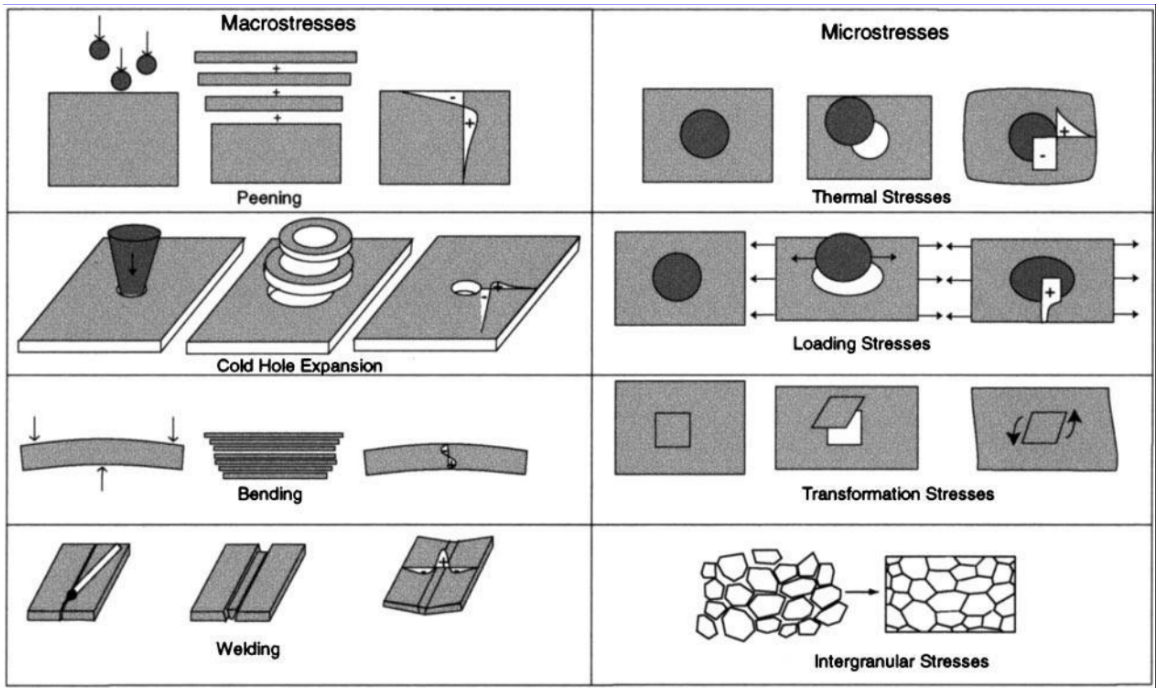

Figure 1.3: Residual stresses arise from misfits, either between different regions of a material or between different phases within the material. Examples of different types of residual macro- and micro-residual stress are illustrated schematically. In each case the process is indicated on the left, the misfit in the center and the resulting stress pattern on the right [33].

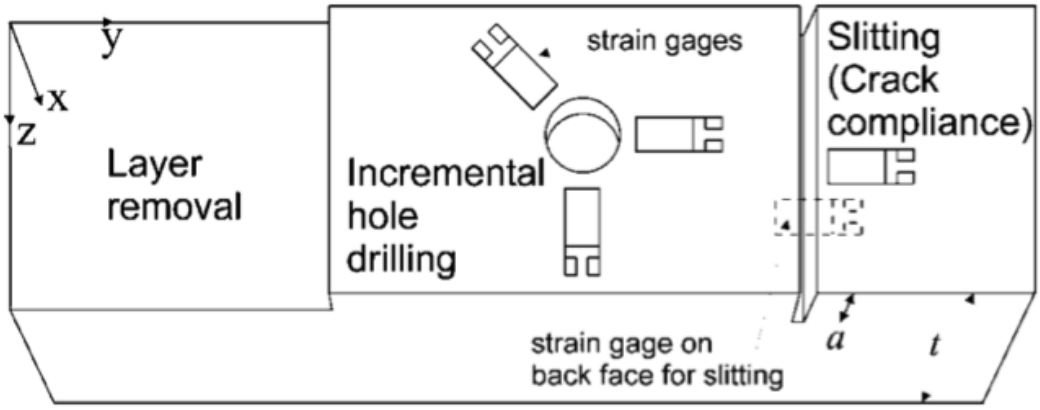

Figure 1.4: Conventional relaxation methods measure residual stress through incremental material removal [22].

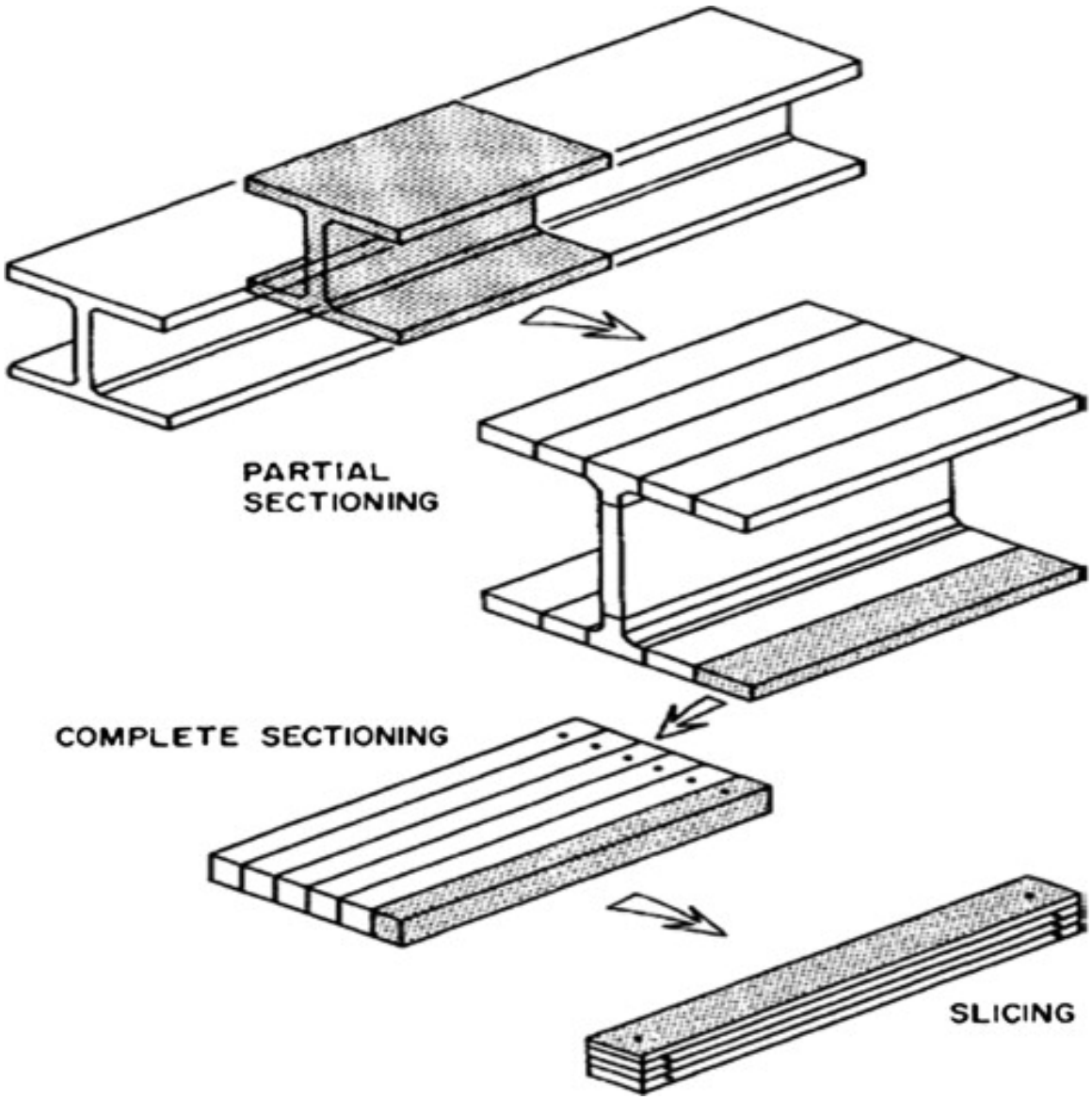

Figure 1.5: Steps of sectioning technique (ST) [29].

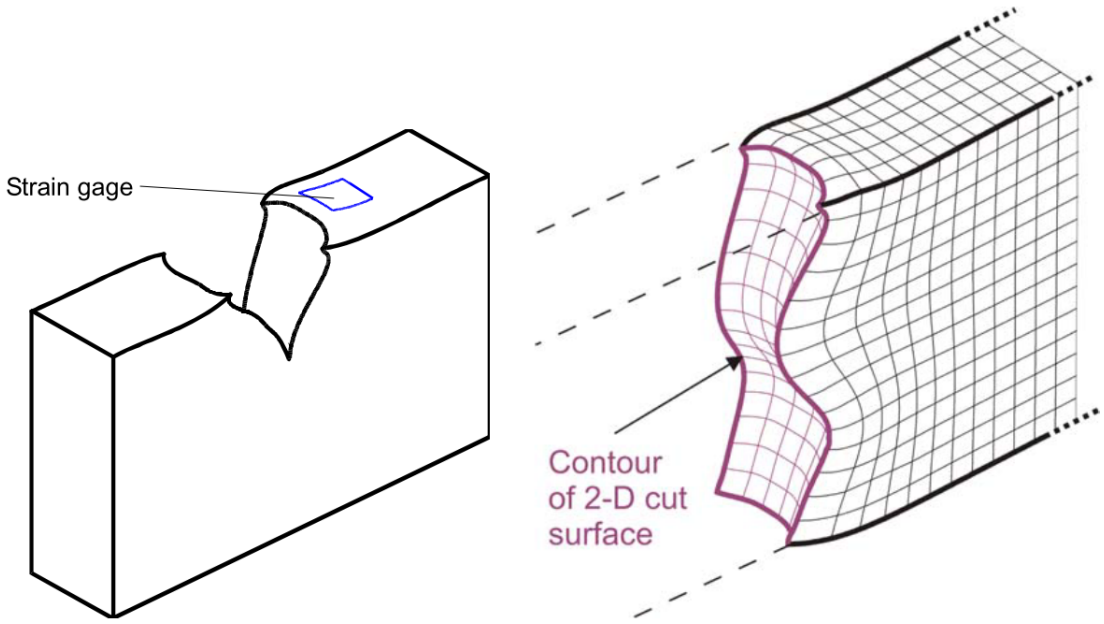

Figure 1.6: Traditional methods (left) use discrete deformation data and the contour method uses a continuous map [22].

at a stress-free state. Thus, stress is related indirectly to the base mechanical properties. Similarly, the destructive techniques rely on mechanical properties and the theory of elasticity to relate deformation to stress. Therefore, regardless of the residual stress measurement technique, accurate knowledge of the mechanical properties of the part in question at the current state of the material is necessary. However, the process history leading to the current state is largely unknown; thus, the primary assumption on which these techniques are based is open to question. Moreover, the existing techniques typically focus on measuring local stresses, or the stresses in certain directions, yielding only partial information rather than the complete state of stress. Consequently they do not provide the complete stress field throughout the body.

Consequently, another objective of this dissertation is to introduce a nondestructive inverse FEA method, termed estimating current state of stress (ECSS), that ccan predict the current state of stress at nodal points of the discretized body together with the elemental incremental elasticity tensors (Chapter 4). The input data are obtained from linear static perturbations of the body. Since the number of unknowns (i.e., nodal stress tensors and incremental elasticity tensors) are larger than the total DOF of the discretized body, more than one linear perturbations are required. Otherwise, ECSS shares the same characteristics and challenges with RULFEM. The ECSS method is developed for two perturbation types.

The study presented in Chapter 5 shares the same objective as that presented in Chapter 4 for the most part. However, the technique presented in Chapter 5 is limited to materials with negligible damping (negligible viscoelastic characteristics). Moreover, the required data are collected from dynamic perturbations. Hence, the method is termed as dynamically estimating residual stresses

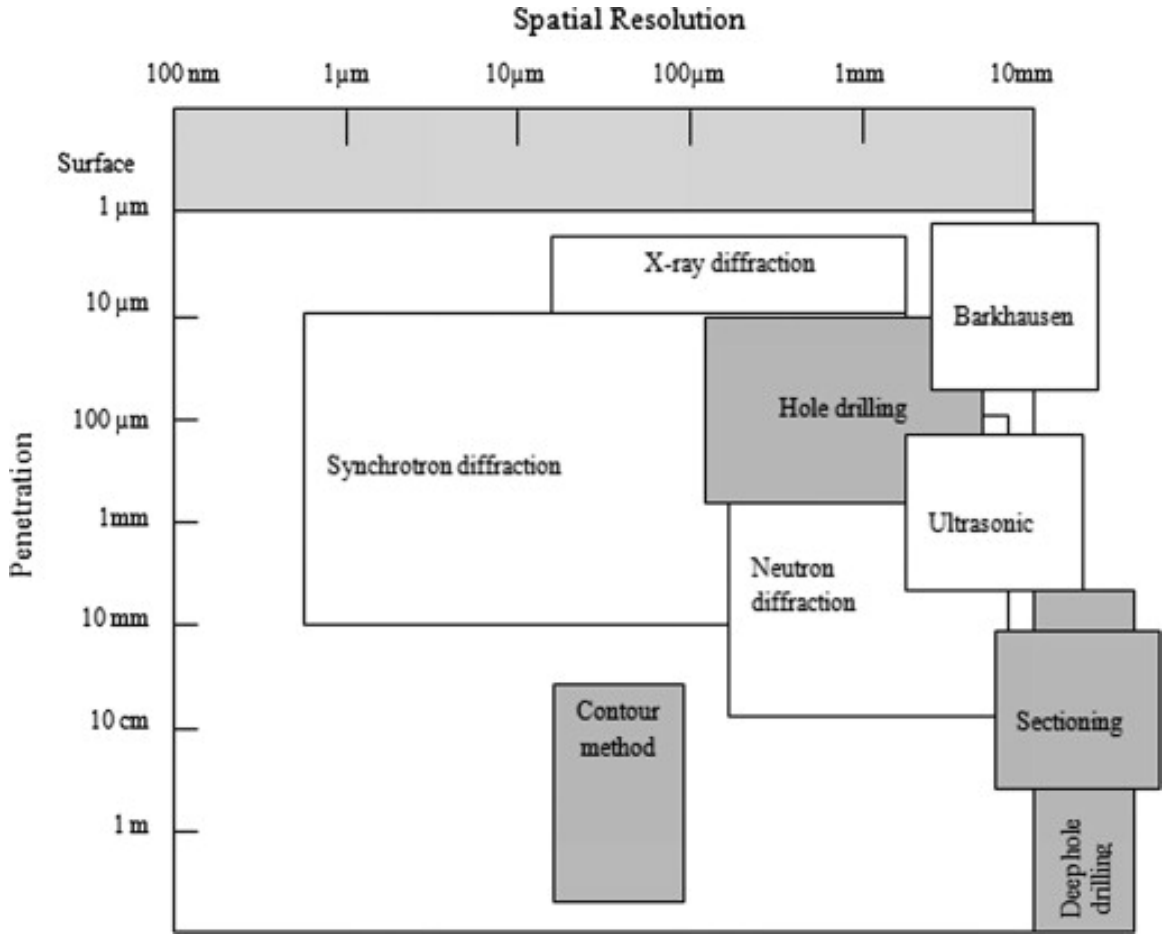

Figure 1.7: Penetration and the spatial resolution of the various techniques. The destructive and semi destructive methods are colored grey [24].

(DRES). Although, DRES is based on *a priori* assumption of negligible damping, it not only generates the same information as ECSS, but also estimates the elemental density. If the number of unknowns (i.e., nodal stress tensors, incremental elasticity tensors, and elemental mass density) are larger than the total DOF of the discretized body, more than one dynamic perturbations are required. DRES and ECSS are similar in formulation, and hence they both share the same characteristics and challenges. However, ECSS is not limited to materials with negligible damping and it does not require dynamic linear perturbations. Most importantly, ECSS predicts CSS of parts subjected to unknown loading, whereas, DRES can only predict the residual stresses in the body.

1.4 Developed Methods

RULFEM requires *one* set of measured full-field displacements and *one* corresponding set of measured tractions due to a small linear perturbation to determine local (element-wise) fourth-

order tangent elasticity tensors without any *a priori* assumptions about a particular constitutive model [28]. Similar measurements and solutions from subsequent linear perturbations generate a set of tangent elasticity tensors for each finite element that can be used to develop constitutive material models or directly used in forward FEA analysis. ECSS, however, requires at least *three* sets of measured full-field displacements and *three* corresponding sets of measured traction to determine the six components of nodal Cauchy stresses and local (element-wise) fourth-order incremental elasticity tensors without any *a priori* assumptions about a particular constitutive model. RULFEM can then be used in subsequent linear perturbations. Similar to RULFEM, ECSS does not require a cost function or a virtual displacement field. The main limitation of both methods is that each finite element is assumed to consist of a single uniform material.

As in the development of RULFEM [28] the development of the ECSS theory requires a thorough knowledge of the updated Lagrangian finite element method (ULFEM) formulation and theory of linear elasticity with initial stress under static loading. Though, a thorough presentation of the linear elasticity theory of elastic bodies under static loading has been developed by Man et al. [19] and Hogger et al. [11], part of Chapter 2 is devoted to present a brief review of the essential relationships involved in the development of RULFEM and ECSS. For completeness, a concise part of ULFEM is also included in Chapter 2. Chapter 3 presents the development of RULFEM and how to assess measurement errors. Chapter 4 provides the development of ECSS for general application to any materials. Chapter 5 demonstrates the details of developing ECSS for parts with negligible damping. Though the main difference of the two methods developed in Chapters 4 (ECSS) and 5 (DRES) seems to be in their perturbation and measurement techniques, DRES is a limited version of ECSS, with the only added advantage being its capability to yield element-wise densities.

Chapter 2

Basic Mechanics Aspects

2.1 Introduction

RULFEM [28] and ECSS rely on inverse FEM and use the theory of linear elasticity and updated Lagrangian finite element method (ULFEM). Thus, a brief overview of these topics and notations is essential, and helpful in the development of RULFEM and ECSS in the following chapters.

2.2 Linearizion of the First Piola-Kirchhoff Stress

Let E^3 be a three-dimensional Euclidean space and consider a body Ω of mass density of ρ_0 at rest in configuration R_0 $\left(R_0 : \Omega \rightarrow E^3\right)$ subjected to surface traction $\overset{\circ}{\mathbf{t}}$ acting on Γ_{q0}, and a body force field $\overset{\circ}{\mathbf{b}}$. The balance of linear momentum in the current configuration of Cauchy stress $\overset{\circ}{\mathbf{T}}\left(=\overset{\circ}{\mathbf{T}}\right)^T$ is:

$$div\left(\overset{\circ}{\mathbf{T}}\right) + \rho_0 \overset{\circ}{\mathbf{b}} = \mathbf{0}; \tag{2.1}$$

and the boundary traction is:

$$\overset{\circ}{\mathbf{t}} = \overset{\circ}{\mathbf{T}}\mathbf{n} \tag{2.2}$$

where $\mathbf{n}$ is the exterior unit normal on the boundary of Γ_{q0}, see Fig. 2.1. The Cauchy stress $\overset{\circ}{\mathbf{T}}$ is the residual stress when $\left(\overset{\circ}{\mathbf{b}}, \overset{\circ}{\mathbf{t}}\right) = (\mathbf{0}, \mathbf{0})$.

The set of second-order tensors and second-order symmetric tensors are denoted by Lin and Sym, respectively, in particular, the second Piola-Kirchhoff stress, $\mathbf{S} \in Sym$, and Cauchy stress, $\overset{\circ}{\mathbf{T}} \in Sym$.

Suppose the body Ω occupies configuration R_1 when it is subjected to a small perturbing traction $\mathbf{t}_1$ applied at Γ_{q1} and boundary condition Γ_{u1}. The Cartesian components of the second Piola-Kirchhoff stress tensor is estimated by [11, 19]:

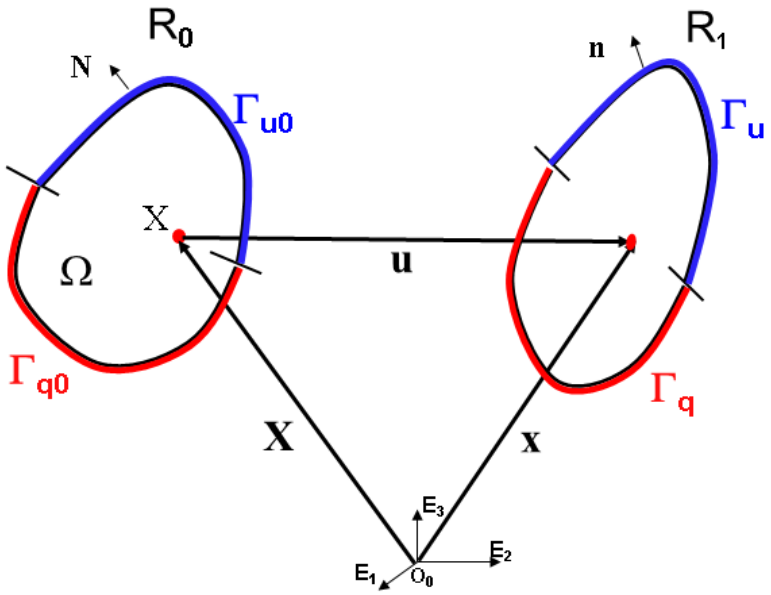

Figure 2.1: The solid body Ω shown in two configurations - reference configuration R_0 with an outward normal vector N and displacement and traction boundary conditions prescribed on Γ_{u0} and Γ_{q0}, respectively, and the deformed configuration R1 with an outward normal vector n and displacement and traction boundary conditions prescribed on Γ_u and Γ_q , respectively [28].

$$\mathbf{S}_{AB} = \mathring{\mathbf{S}}_{AB} + \mathbb{L}_{ABCD}\left[\mathbf{E}_{CD}\right] + O(\epsilon^2) \tag{2.3}$$

where $\mathring{\mathbf{S}}$ is the second Piola-Kirchhoff stress at configuration R_0, and is equal to the Cauchy stress referred to the latter (i.e., $\mathring{\mathbf{T}} = \mathring{\mathbf{S}}$). $\mathbb{L}_0 : Lin \rightarrow Sym$, is the fourth order incremental elasticity tensor at configuration R_0, and $\mathbf{E} = (\mathbf{H} + \mathbf{H}^T)/2$ is the symmetric part of the deformation gradient tensor $\mathbf{H} = \dfrac{\partial \mathbf{u}}{\partial \mathbf{X}}$, and epsilon os the norm of the incremental strain. In invariant tensor form, eq. (2.3) is:

$$\mathbf{S} = \mathring{\mathbf{T}} + \mathbb{L}_0\left[\mathbf{E}\right] + o\left(\|\mathbf{H}\|\right) \text{ as } \mathbf{H} \rightarrow \mathbf{0} \tag{2.4}$$

Consequently, the first Piola-Kirchhoff stress, $\mathbf{P}$, is:

$$\mathbf{P} = \mathbf{F}\left(\mathring{\mathbf{T}} + \mathbb{L}_0\left[\mathbf{E}\right] + o\left(\|\mathbf{H}\|\right)\right) \text{ as } \mathbf{H} \rightarrow \mathbf{0} \tag{2.5}$$

where $\mathbf{F} = \mathbf{I} + \mathbf{H}$ is the deformation gradient. Further simplification of Eq. (2.5) yields:

$$\mathbf{P} = \mathring{\mathbf{T}} + \mathbf{H}\mathring{\mathbf{T}} + \mathbb{L}_0\left[\mathbf{E}\right] + \mathbf{H}\mathbb{L}_0\left[\mathbf{E}\right] + o\left(\|\mathbf{H}^2\|\right) \text{ as } \mathbf{H} \rightarrow \mathbf{0} \tag{2.6}$$

For sufficiently small perturbations, the order of the norm of the fourth term on the right-hand side is bounded above by the norm of $\mathbf{H}$; i.e.,

$$o\left(\|\mathbf{H}\mathbb{L}_0\left[\mathbf{E}\right]\|\right) \leq o\left(\|\mathbf{H}\|\right) \tag{2.7}$$

Thus eq. (2.6) may be rewritten as:

$$\mathbf{P} = \mathring{\mathbf{T}} + \mathbf{H}\mathring{\mathbf{T}} + \mathbb{L}_0\left[\mathbf{E}\right] + o\left(\|\mathbf{H}^2\|\right) \text{ as } \mathbf{H} \rightarrow \mathbf{0} \tag{2.8}$$

Let $\mathbf{F}_1^0$ be the gradient of the deformation from configuration R_0 to configuration R_1. The associiated first Piola-Kirchhoff stress is:

$$\mathbf{P}_1^0 = \widehat{\mathbf{P}}\left(\mathbf{F}_1^0\right) = \widehat{\mathbf{P}}\left(\mathbf{I} + \mathbf{H}_1^0\right) \tag{2.9}$$

where $\widehat{\mathbf{P}}$ generally depends explicitly on the position vector $\mathbf{x}_0^0$ in configuration R_0. Consequently, the second Piola-Kirchhoff and Cauchy stress are related to the first Piola-Kirchhoff stress as:

$$\mathbf{S}_1^0 = \widehat{\mathbf{S}}\left(\mathbf{F}_1^0\right) = \left(\mathbf{F}_1^0\right)^{-1}\widehat{\mathbf{P}}\left(\mathbf{F}_1^0\right) = \left(\widehat{\mathbf{P}}\left(\mathbf{F}_1^0\right)\right)^T\left(\mathbf{F}_1^0\right)^{-T} \tag{2.10}$$

$$\mathbf{P}_1^0 = \det\left(\mathbf{F}_1^0\right)\mathbf{T}_1^1\left(\mathbf{F}_1^0\right)^{-T} = J_1^0\mathbf{T}_1^1\left(\mathbf{F}_1^0\right)^{-T} \tag{2.11}$$

where $J_1^0 = \det\left(\mathbf{F}_1^0\right) > 0$. The elemental volume dV_1 in R_1 is related to the reference elemental volume dV_0 by $d\mathrm{V}_1 = J_1^0 dV_0$.

At the reference configuration R_0, the first Piola-Kirchhoff stress is symmetric and equal to the Cauchy stress relative to that configuration; i.e., $\mathring{\mathbf{T}} = \mathbf{T}_0^0\left(= \left(\mathbf{T}_0^0\right)^T = \mathring{\mathbf{T}}^T\right)$ as $\mathbf{H}_1^0 = \mathbf{0}$. Thus,

$$\widehat{\mathbf{P}}\left(\mathbf{I}\right) = \mathring{\mathbf{T}} \tag{2.12}$$

The first Piola-Kirchhoff stress in the new configuration may be expressed as (using Eq. (2.8)):

$$\mathbf{P}_1^0 = \mathring{\mathbf{T}} + \mathbf{H}_1^0\mathring{\mathbf{T}} + \mathbb{L}_0\left[\mathbf{E}_1^0\right] = \mathbf{F}_1^0\mathring{\mathbf{T}} + \mathbb{L}_0\left[\mathbf{E}_1^0\right] \tag{2.13}$$

where $\mathbb{L}_0 = \partial\widehat{\mathbf{S}}(\mathbf{I})/\partial\mathbf{E}_1^0$, and $\mathbf{E}_1^0$ is the symmetric part of $\mathbf{H}_1^0$. An alternative from of Eq. (2.13) can be expressed as

$$\mathbf{P}_1^0 = \mathring{\mathbf{T}} + \mathbb{C}_0\left[\mathbf{H}_1^0\right] \tag{2.14}$$

where $\mathbb{C}_0$ is the fourth-order elasticity tensor, defined as $\mathbb{C}_0 = \partial\widehat{\mathbf{P}}(\mathbf{I})/\partial\mathbf{F}_1^0$.

Let $\mathbf{W} = \left(\mathbf{H} - \mathbf{H}^T\right)/2$ be the skew-symmetric part of $\mathbf{H}$. From Eqs. (2.13) and (2.14), it follows that

$$\mathbb{C}_0\left[\mathbf{H}_1^0\right] = \left[\mathbf{H}_1^0\right]\mathring{\mathbf{T}} + \mathbb{L}_0\left[\mathbf{E}_1^0\right] \tag{2.15}$$

$$\mathbb{L}_0\left[\mathbf{W}_1^0\right] = \mathbf{0} \tag{2.16}$$

Because $\mathbb{L}_0$ satisfies Eq. (2.16) and $\mathbb{L}_0\left[\mathbf{W}_1^0\right] \in \mathsf{S}_s$, where S_s is a set of second-order symmetric tensors, it may be inferred that $\mathbb{L}_0$ possesses minor symmetry when considered as a fourth-order tensor; i.e., $\mathbb{L}_{ijkl} = \mathbb{L}_{jikl} = \mathbb{L}_{ijlk}$ [19].

Similarly, suppose the body Ω occupies configurations R_2, R_3 as a result of subsequent small perturbations. The first Piola-Kirchoff stresses at each of these configurations are:

$$\mathbf{P}_2^1 = \mathbf{F}_2^1\mathbf{T}_1^1 + \mathbb{L}_1\left[\mathbf{E}_2^1\right] \tag{2.17}$$

$$\mathbf{P}_3^2 = \mathbf{F}_3^2\mathbf{T}_2^2 + \mathbb{L}_2\left[\mathbf{E}_3^2\right] \tag{2.18}$$

and the current Cauchy stresses are related to the previous-step Piola-Kirchoff stresses in a manner similar to Eq. (2.11):

$$\mathbf{T}_1^1 = \frac{1}{J_1^0}\mathbf{P}_1^0\left(\mathbf{F}_1^0\right)^T \tag{2.19}$$

$$\mathbf{T}_2^2 = \frac{1}{J_2^1}\mathbf{P}_2^1\left(\mathbf{F}_2^1\right)^T \tag{2.20}$$

Making use of Eqs. (2.8), (2.19), and the composition rule for consecutive deformation gradients (i.e. $F_n^{n-2} = F_n^{n-1}F_{n-2}^{n-1}$ and $J_2^0 = J_2^1J_1^0$), Eq. (2.17) may be rewritten as a function of $\mathring{\mathbf{T}}$, $\mathbb{L}_0$, and $\mathbb{L}_1$:

$$\mathbf{P}_2^1 = \frac{1}{J_1^0}\left(\mathbf{F}_2^0\mathring{\mathbf{T}} + \mathbf{F}_2^1\mathbb{L}_0\left[\mathbf{E}_1^0\right]\right)\left(\mathbf{F}_1^0\right)^T + \mathbb{L}_1\left[\mathbf{E}_2^1\right] \tag{2.21}$$

Similarly, the next-step Piola-Kirchoff stress,$\mathbf{P}_3^2$, can be rewritten:

$$\mathbf{P}_3^2 = \frac{1}{J_2^0}\left(\mathbf{F}_3^0\mathring{\mathbf{T}} + \mathbf{F}_3^1\mathbb{L}_0\left[\mathbf{E}_1^0\right]\right)\left(\mathbf{F}_2^0\right)^T + \frac{1}{J_2^1}\mathbf{F}_3^2\mathbb{L}_1\left[\mathbf{E}_2^1\right]\left(\mathbf{F}_2^1\right)^T + \mathbb{L}_2\left[\mathbf{E}_3^2\right] \tag{2.22}$$

and, continuing, the first Piola-Kirchoff after $n+1$ step is seen to be:

$$\mathbf{P}_{n+1}^n = \frac{1}{J_n^0}\left(\mathbf{F}_{n+1}^0\mathring{\mathbf{T}} + \mathbf{F}_{n+1}^1\mathbb{L}_0\left[\mathbf{E}_1^0\right]\right)\left(\mathbf{F}_n^0\right)^T + \sum_{i=2}^{n}\left(\frac{1}{J_i^{i-1}}\mathbf{F}_{i+1}^i\mathbb{L}_{i-1}\left[\mathbf{E}_i^{i-1}\right]\left(\mathbf{F}_i^{i-1}\right)^T\right) + \mathbb{L}_n\left[\mathbf{E}_{n+1}^n\right] \tag{2.23}$$

2.3 A Brief Review of Updated Lagrangian Method, ULFEM

One of the common finite element techniques treating nonlinear solid mechanics problems is the updated Lagrangian finite element method, ULFEM, where the final deformed configurations are achieved incrementally with each increment treated as the reference configuration for the next increment [3, 20]. A brief overview of ULFEM is presented here to establish the basic formulations for the developed techniques presented in the main chapters.

Consider the solid body Ω in the coordinate system shown in Fig. 2.1.

$$Div\,(\mathbf{P}) + \rho_0 \mathbf{b} = \rho_0 \mathbf{a} \quad \text{in } R_0 \tag{2.24a}$$

$$\mathbf{PN} = \bar{\mathbf{p}} \text{ on } \Gamma_{q_0} \tag{2.24b}$$

$$\mathbf{u} = \bar{\mathbf{u}} \text{ on } \Gamma_{u_0} \tag{2.24c}$$

where $\mathbf{P}$ is the first Piola-Kirchhoff stress, $\rho_0 = \widehat{\rho_0}\,(\mathbf{X})$ is the density, $\mathbf{b}$ is the body force, $\mathbf{a}$ us the acceleration, $\mathbf{N}$ is the unit normal vector, $\bar{\mathbf{p}}$, is the traction acting on boundary Γ_{q_0}, and $\bar{\mathbf{u}}$ is the displacement specified over boundary Γ_{u_0}.

The position vector of any material point X in the new configuration R is defined as $\mathbf{x} = \mathbf{X} + \mathbf{u}\,(\mathbf{X}, t)$, where the displacement field u is defined in the following set $\mathscr{S}_u$:

$$\mathscr{S}_u = \left\{ \mathbf{u} : R_0 \times \mathbb{R}^3 \mapsto \mathbb{R}^3 \,\middle|\, \mathbf{u} = \bar{\mathbf{u}} \text{ on } \Gamma_{u_0}, \mathbf{u}\,(\mathbf{X}, t_0) = \bar{\mathbf{u}},\ J_0 = det\left(\mathbf{I} + \frac{\partial \mathbf{u}}{\partial \mathbf{X}}\right) > 0, \frac{d\mathbf{u}\,(\mathbf{X}, t_0)}{dt} = \mathbf{0} \text{ in } R_0 \right\} \tag{2.25}$$

where $\mathbf{I}$ is the second-order identity tensor.

Consequently, the deformation gradient tensor $\mathbf{F}$ is expressed as ζ

$$\mathbf{F} = \mathbf{I} + \frac{\partial \mathbf{u}}{\partial \mathbf{X}} = \mathbf{I} + \mathbf{H} \tag{2.26}$$

where $\mathbf{H}$ is the displacement gradient tensor.

To find the displacement function of the body $\mathbf{u}\,(\mathbf{X}, t_0)$ under the given boundary conditions [Eqs. (2.24b) and (2.24c)], the weak-form of the problem is generated by applying a tangent vector field $\boldsymbol{\zeta}$ (also known as the test function), which is typically expressed as the product of a test function of time $\theta\,(t)$ and a test function of space $\boldsymbol{\xi}\,(\mathbf{X})$, i.e.,

$$\boldsymbol{\zeta} = \hat{\boldsymbol{\zeta}}\,(\mathbf{X}, t) = \theta\,(t)\,\boldsymbol{\xi}\,(\mathbf{X}) \tag{2.27}$$

for an admissible $\boldsymbol{\xi} = \boldsymbol{\xi}\,(\mathbf{X})$, i.e.,

$$\mathscr{S}_\xi = \left\{ \boldsymbol{\xi} : R_0 \times \mathbb{R}^3 \mapsto \mathbb{R}^3 \,\middle|\, \boldsymbol{\xi} = \mathbf{0} \text{ on } \Gamma_{u0} \right\} \tag{2.28}$$

Fig. 2.2 shows a body Ω in the reference configuration R_0 at time t_0, which, after n infinitesimal deformations in time increments Δt, attains configuration R_n at time $t + n\Delta t$. A solution of the

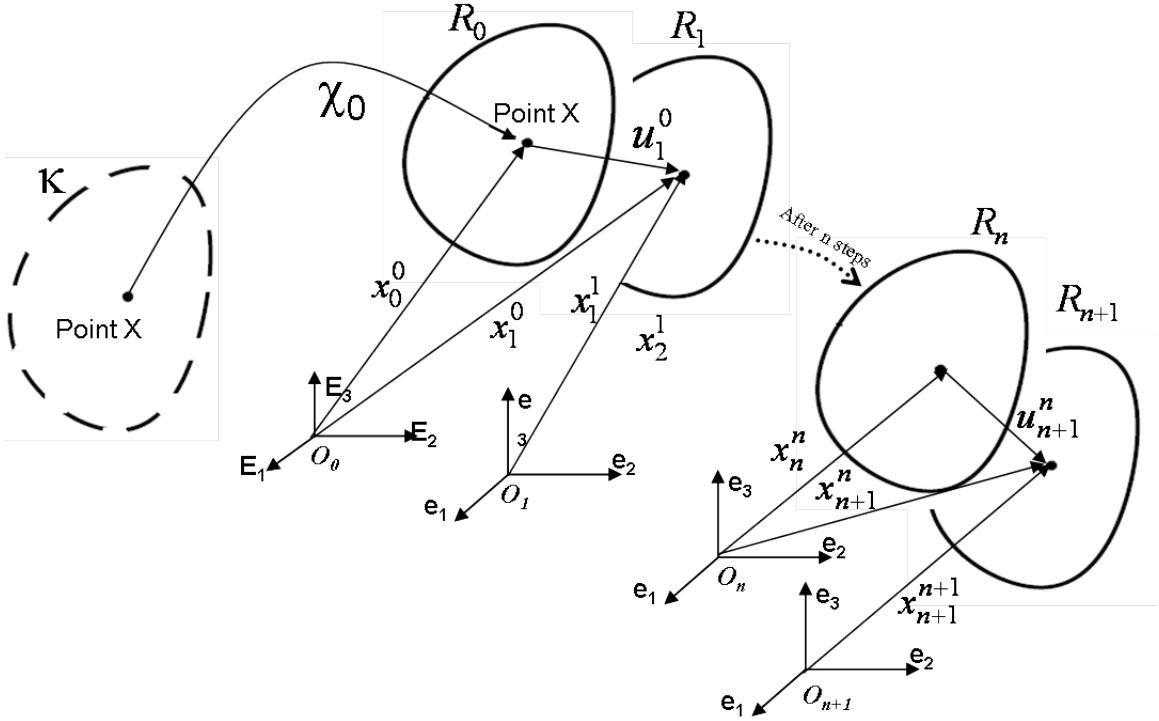

Figure 2.2: Updated Lagrangian Method

incremental displacement field $\mathbf{u}|_{n+1}^{n}$, using configuration R_n as a reference, can be obtained by considering the general updated Lagrangian weak-form [3] expressed as

$$r_{n+1} = \int_{R_n} (\boldsymbol{\xi}|_{n+1}^{n} \rho_n \, \mathbf{a}|_{n+1}^{n}) \, dV_n + \int_{R_n} \left(\mathbf{P}|_{n+1}^{n} \, \frac{\partial \boldsymbol{\xi}|_{n+1}^{n}}{\partial \mathbf{x}_n} \right) dV_n - \int_{R_n} (\boldsymbol{\xi}|_{n+1}^{n} \rho_n \, \mathbf{b}|_{n+1}^{n}) \, dV_n - \int_{R_n} (\boldsymbol{\xi}|_{n+1}^{n} \, \bar{\mathbf{p}}|_{n}^{n}) \, dA_n \tag{2.29}$$

where r_{n+1} is the residual of the weak-form at time $t_0 + (n+1)\Delta t$ (i.e., body configuration R_{n+1}), $\boldsymbol{\xi}|_{n+1}^{n}$, $\mathbf{a}|_{n+1}^{n} = \dfrac{d^2\mathbf{x}|_{n+1}^{n}}{dt^2}$, $\mathbf{b}|_{n}^{n}$, $\bar{\mathbf{p}}|_{n}^{n}$, and $\mathbf{P}|_{n+1}^{n} = \widehat{\mathbf{P}}\left(\mathbf{H}|_{n+1}^{n}, \dot{\mathbf{H}}|_{n+1}^{n}\right)$ are the tangent vector field, acceleration, body force, Piola–Kirchhoff surface traction, and the first Piola–Kirchhoff stress, respectively, is the material density of body at time $t_0 + nt$, and dV_n and dA_n are the elemental volume and area, respectively.

In addition to $\mathbf{u}|_{n+1}^{n} \in \mathscr{S}_u$ [Eq. (2.25)] and $\boldsymbol{\xi}|_{n+1}^{n} \in \mathscr{S}_\xi$ [Eq. (2.28)] for the integrals in the updated Lagrangian weak-form [Eq (2.29)] to be bounded, $\mathbf{u}|_{n+1}^{n}$ and $\boldsymbol{\xi}|_{n+1}^{n}$ must also belong to an appropriate Hilbert space $\mathbb{H}^1(R_n)$. Thus, the corresponding sets of $\mathbf{u}_h|_{n+1}^{n}$ and $\boldsymbol{\xi}_h|_{n+1}^{n}$ in the updated Lagrangian weak-form, $\mathscr{S}_{\mathbf{u}_n}^{wf}$ and $\mathscr{S}_{\boldsymbol{\xi}_n}^{wf}$, respectively, are as defined as

$$\mathscr{S}_{\mathbf{u}_n}^{wf} = \mathscr{S}_{\mathbf{u}} \cap \left\{ \mathbf{u}_h|_{n+1}^{n} \in \mathbb{H}^1(R_n) \,\middle|\, \mathbf{u}_h|_{n+1}^{n} = \bar{\mathbf{u}}|_{n+1}^{n} \text{ on } \Gamma_{u_n} \right\} \tag{2.30}$$

$$\mathscr{S}^{wf}_{\boldsymbol{\xi}_n} = \mathscr{S}_{\boldsymbol{\xi}} \cap \left\{ \boldsymbol{\xi}_h|^n_{n+1} \in \mathbb{H}^1(R_n) \,\middle|\, \boldsymbol{\xi}_h|^n_{n+1} = \mathbf{0} \text{ on } \Gamma_{u_n} \right\} \tag{2.31}$$

Assume that the domain represented by configuration R_n is discretized by N_e elements so that $R_n = \cup_1^{N_e} \Omega^e$, where Ω^e represents the element domain, and that the corresponding total number of nodes is N_n . Then, Eq. (2.29) can be solved for all nodal points of the finite element mesh. The displacement field within each element is described by N_p polynomials, known as the shape functions ϕ^e_1, ϕ^e_2, . . ., and $\phi^e_{N_p}$. Thus, the displacement field in each element can be expressed as

$$\begin{aligned} \mathbf{u}^e|^n_{n+1} &= \mathbf{x}^e_h|^n_{n+1} - \mathbf{x}^e_h|^n_n \\ &= \sum_{i=1}^{N_p} \left[\phi^e_i \left(\mathbf{x}^e_h|^n_n \right) \mathbf{u}^e_{h,i}|^n_{n+1} \right] = [\boldsymbol{\phi}^e] \{\mathbf{u}^e_h\}^n_{n+1} \end{aligned} \tag{2.32}$$

where superscript e and subscript h denote elemental quantities defined at nodal points, $[\boldsymbol{\phi}^e]$ is the elemental shape function matrix, and $\left\{\mathbf{u}^e_h\right\}^n_{n+1}$ is the vector of finite element nodal displacements. For a 3D space, the size of the elemental vectors $\left\{\mathbf{u}^e_h\right\}^n_{n+1}$ and $\{\boldsymbol{\xi}^e_h\}^n_{n+1}$ is equal to $(3N_p \times 1)$. Consequently, the size of ϕ is $(3 \times 3N_p)$. However, these vectors must belong to weak-form admissible subsets $\mathscr{S}^{wf}_{\mathbf{u}_n,h}$ and $\mathscr{S}^{wf}_{\boldsymbol{\xi}_n,h}$, such that $\mathscr{S}^{wf}_{\mathbf{u}_n,h} \in \mathscr{S}^{wf}_{\mathbf{u}_n}$ and $\mathscr{S}^{wf}_{\boldsymbol{\xi}_n,h} \in \mathscr{S}^{wf}_{\boldsymbol{\xi}_n}$ [3, 20].

The other vector and tensor quantities of each element [Eq. (2.29)]in the domain of configuration R_n can also be expressed in terms of elemental shape functions as shown below.

(i) The acceleration vector:

$$\begin{aligned} \mathbf{a}^e|^n_{n+1} &= \frac{d^2 \mathbf{X}^e|^n_{n+1}}{dt^2} = \sum_{i=1}^{N_p} \left[\phi^e_i \mathbf{a}^e_{h,i}|^n_{n+1} \right] \\ &= [\boldsymbol{\phi}^e] \{\mathbf{a}^e_h\}^n_{n+1} \end{aligned} \tag{2.33}$$

where the size of $\mathbf{a}^e|^n_{n+1}$ and nodal acceleration vector $\left\{\mathbf{a}^e_h\right\}^n_{n+1}$ is equal to (3×1) and $(3N_p \times 1)$, respectively.

(ii) The displacement gradient tensor:

$$\begin{aligned} \mathbf{H}^e|^n_{n+1}(\mathbf{u}^e|^n_{n+1}) &= \frac{\partial \mathbf{u}^e|^n_{n+1}}{\partial \mathbf{x}|^n_n} = \sum_{i=1}^{N_p} \left[\frac{\partial \phi^e_i}{\partial \mathbf{x}|^n_n} \mathbf{u}^e_{h,i}|^n_{n+1} \right] \\ &= [\mathbf{B}^e] \{\mathbf{u}^e_h\}^n_{n+1} \end{aligned} \tag{2.34}$$

Although $\mathbf{H}^e|^n_{n+1}$ is a second-order tensor and its components are typically represented by a (3×3) matrix, in the present weak formulation it is represented by a (9×1) vector, i.e., $\left\{\mathbf{H}^e_h\right\}^n_{n+1}$; therefore, $[\mathbf{B}^e]$ is formulated as a $(9 \times 3N_p)$ matrix.

(iii) The gradient of the tangent vector tensor:

$$\boldsymbol{\xi}^e|_{n+1}^n = \sum_{i=1}^{N_p} \left[\phi_i^e \boldsymbol{\xi}_{h,i}^e|_{n+1}^n\right] = [\boldsymbol{\phi}^e]\,\{\boldsymbol{\xi}_h^e\}_{n+1}^n \tag{2.35}$$

Because $\boldsymbol{\xi}_h|_{n+1}^n$ is a (3×1) vector, it's gradient is defined by

$$\mathbf{H}^e|_{n+1}^n(\boldsymbol{\xi}^e|_{n+1}^n) = \sum_{i=1}^{N_p} \left[\frac{\partial \phi_i^e}{\partial \mathbf{x}_n^n} \boldsymbol{\xi}_h^e|_{n+1}^n\right] = [\mathbf{B}^e]\,\{\boldsymbol{\xi}_h^e\}_{n+1}^n \tag{2.36}$$

(iv) The body force vector field:

$$\mathbf{b}^e|_n^n = \sum_{i=1}^{N_p} \left[\phi_i^e \mathbf{b}_{h,i}^e|_n^n\right] = [\boldsymbol{\phi}^e]\,\{\mathbf{b}_h^e\}_n^n \tag{2.37}$$

where the size of $\mathbf{b}^e|_{n+1}^n$ and the nodal body force vector, $\left\{\mathbf{b}_h^e\right\}_n^n$ are equal to (3×1) and $(3N_p \times 1)$, respectively.

(v) The Piola-Kirchhoff traction vector:

$$\mathbf{p}^e|_n^n = \sum_{i=1}^{N_p} \left[\phi_i^e \mathbf{p}_{h,i}^e|_n^n\right] = [\boldsymbol{\phi}^e]\,\{\mathbf{p}_h^e\}_n^n \tag{2.38}$$

where the size of $\mathbf{p}^e|_n^n$ and the nodal traction vector $\left\{\mathbf{p}_h^e\right\}_n^n$ are (3×1) and $(3N_p\times1)$, respectively.

The numerical form of Eq. (2.29) is obtained by substituting Eqs. (2.33)-(2.38) into Eq. (2.29), factoring out the nodal tangent vector $\{\boldsymbol{\xi}_h^e\}_{n+1}^n$, and assembling over the entire domain of the body. However, numerical approximation of Eq. (2.29) yields a nonzero residual r_{n+1} at each increment step. Therefore, an assembly operator $\mathcal{A}_{e=1}^{N_e}$ that combines all the common nodal DOF of the finite elements is introduced in the re-formulated Eq. (2.29) as shown below:

$$r_{n+1} = \mathcal{A}_{e=1}^{N_e} \left\{ \{\boldsymbol{\xi}_h^e\}_{n+1}^{n\ T} \left\{ \left[\int_{R_n} \left([\boldsymbol{\phi}^e]^T \rho_n^e [\boldsymbol{\phi}^e]\right) d\mathrm{V}_n^e\right] \{\mathbf{a}_h^e\}_{n+1}^n + \left[\int_{R_n} \left([\mathbf{B}^e]^T \widehat{\mathbf{P}}^e \left(\mathbf{H}^e|_{n+1}^n, \dot{\mathbf{H}}^{\mathbf{e}}|_{n+1}^n\right)\right) d\mathrm{V}_n^e\right] \right.\right.$$
$$\left.\left. - \left[\int_{R_n} \left([\boldsymbol{\phi}^e]^T \rho_n^e [\boldsymbol{\phi}^e] \{\mathbf{b}_h^e\}_n^n\right) d\mathrm{V}_n^e\right] - \left[\int_{\Gamma_{qn}^e} \left([\boldsymbol{\phi}^e]^T [\boldsymbol{\phi}^e] \{\bar{\mathbf{p}}_h^e\}_n^n\right) d\mathrm{A}_n^e\right] \right\} \right\} \tag{2.39}$$

A numerical solution of Eq. (2.39) that yields $r_{n+1} = 0$ is incrementally obtained at each step. Since the tangent vector $\{\boldsymbol{\xi}_h^e\}_{n+1}^n$ is an arbitrary vector that vanishes at the boundary h n+1 [Eq. (2.28)], the solution can be found by setting the terms inside the second bracket equal to zero, i.e.,

$$\mathcal{A}_{e=1}^{N_e}\left\{\left[\int_{R_n}\left([\boldsymbol{\phi}^e]^T\rho_n^e[\boldsymbol{\phi}^e]\right)d\mathrm{V}_n^e\right]\{\mathbf{a}_h^e\}_{n+1}^n+\left[\int_{R_n}\left([\mathbf{B}^e]^T\widehat{\mathbf{P}}^e\left(\mathbf{H}^e|_{n+1}^n,\dot{\mathbf{H}}^{\mathbf{e}}|_{n+1}^n\right)\right)d\mathrm{V}_n^e\right]\right.$$
$$\left.-\left[\int_{R_n}\left([\boldsymbol{\phi}^e]^T\rho_n^e[\boldsymbol{\phi}^e]\{\mathbf{b}_h^e\}_n^n\right)d\mathrm{V}_n^e\right]-\left[\int_{\Gamma_{qn}^e}\left([\boldsymbol{\phi}^e]^T[\boldsymbol{\phi}^e]\{\bar{\mathbf{p}}_h^e\}_n^n\right)d\mathrm{A}_n^e\right]\right\}=0 \tag{2.40}$$

Eq. (2.40) can be written in more concise form by introducing the mass matrix, the stiffness-displacement vector, and the force vector, defined below.

(i) The mass matrix in configuration R_n :

$$[\mathbf{M}]_n^n=\mathcal{A}_{e=1}^{N_e}\left\{\int_{R_n}\left([\boldsymbol{\phi}^e]^T\rho_n^e[\boldsymbol{\phi}^e]\right)d\mathrm{V}_n^e\right\} \tag{2.41}$$

(ii) The stiffness-displacement vector with respect to configuration R_n and displacement vector, mapping configuration R_n to configuration R_{n+1}:

$$\{\Pi(\mathbf{u})\}_{n+1}^n=\mathcal{A}_{e=1}^{N_e}\left\{\int_{R_n}\left([\mathbf{B}^e]^T\widehat{\mathbf{P}}^e\left(\mathbf{H}^e|_{n+1}^n,\dot{\mathbf{H}}^{\mathbf{e}}|_{n+1}^n\right)\right)d\mathrm{V}_n^e\right\} \tag{2.42}$$

(iii) The force vector in configuration R_n:

$$\{\mathbf{f}\}_n^n=\mathcal{A}_{e=1}^{N_e}\left\{\left[\int_{R_n}\left([\boldsymbol{\phi}^e]^T\rho_n^e[\boldsymbol{\phi}^e]\right)d\mathrm{V}_n^e\right]\{\mathbf{b}_h^e\}_n^n+\int_{\Gamma_{qn}^e}\left([\boldsymbol{\phi}^e]^T[\boldsymbol{\phi}^e]\{\bar{\mathbf{p}}_h^e\}_n^n\right)d\mathrm{A}_n^e\right\} \tag{2.43}$$

Substitution of Eqs. (2.41)-(2.43) into Eq. (2.40) yields

$$[\mathbf{M}]_n^n\{\mathbf{a}_h\}_{n+1}^n+\{\Pi(\mathbf{u})\}_{n+1}^n=\{\mathbf{f}\}_n^n \tag{2.44}$$

Hence, the problem reduces to finding a discrete deformation vector $\{\mathbf{u}_h\}_{n+1}^n$ that satisfies Eqs. (2.40) and (2.44). The integral terms can be computed by a common numerical integration method, such as Gaussian quadrature [20].

A general incrementally linear constitutive framework appropriate for static conditions is presumed. Consider a steady state or quasi-static motion of a solid body Ω , shown in Fig. 2.1, from configuration R_0 to configuration R_1 under an incremental body force of $\mathbf{b}$ and the second Piola-Kirchhoff boundary traction force of $\bar{\mathbf{s}}_0$ on Γ_{q_0} boundary with outward unit normal vector of $\mathbf{N}_0^0$ and boundary displacement of $\bar{\mathbf{u}}$ on non-overlapping boundary of Γ_{u_0}. Suppose the body is meshed with N_e elements and N_n nodes. The first weak form formulation of updated Lagrangian Finite Element Method becomes [28]

$$\underbrace{\mathcal{A}_{e=1}^{N_e}\left\{\int_{R_0}\left([\mathbf{B}^e]^T\,\widehat{\mathbf{P}}^e\left(\mathbf{H}^e|_1^0\right)\right)d\mathrm{V}_0^e\right\}}_{\{\Pi(\mathbf{u})\}_1^0}=\underbrace{\mathcal{A}_{e=1}^{N_e}\left\{\int_{R_0}\left([\boldsymbol{\phi}^e]^T\,\rho_0^e\,[\boldsymbol{\phi}^e]\,\{\mathbf{b}_h^e\}_1^0\right)d\mathrm{V}_0^e\right\}}_{\{\mathbf{f}_h^b\}_1^0}+\underbrace{\mathcal{A}_{e=1}^{N_e}\left\{\int_{\Gamma_{q0}^e}\left([\boldsymbol{\phi}^e]^T\left\{\widehat{\mathbf{P}}^e\left(\mathbf{H}^e|_1^0\right)\mathbf{N}_0^0\right\}\right)d\mathrm{A}_0^e\right\}}_{\{\mathbf{f}_h^t\}_1^0} \tag{2.45}$$

which can be written as:

$$\underbrace{\{\Pi(\mathbf{u})\}_1^0}_{3N_n\times 1}=\underbrace{\{\mathbf{f}_h\}_1^0}_{3N_n\times 1} \tag{2.46}$$

where $\mathcal{A}_{e=1}^{N_e}$ is an assembly operator that combines all the common nodal degrees of freedom (DOF) of the finite elements (with each element having N_p nodes), $[\boldsymbol{\phi}^e]$ is the elemental shape function, matrix $[\mathbf{B}^e]$ is a differential operator matrix, ρ_0^e is the elemental density at R_0 configuration, $\left\{\mathbf{b}_h^e\right\}_1^0$ is the elemental body force vector, with all equations given in the Appendix, and $d\mathrm{A}_0^e$ is the area measure of element e with respect to the reference configuration R_0. The term $\left\{\widehat{\mathbf{P}}^e\left(\mathbf{H}^e|_1^0\right)\mathbf{N}_0^0\right\}$ is the first Piola-Kirchhoff traction $\bar{\mathbf{p}}_0$ on Γ_{q0} that is related to $\bar{\mathbf{s}}_0$ (Eq. (2.10)), and its related force vector is denoted as where $\{\mathbf{f}_h\}_1^0$ is sum of nodal body forces and nodal traction forces, that is:

$$\{\mathbf{f}_h\}_1^0=\left\{\mathbf{f}_h^b\right\}_1^0+\{\mathbf{f}_h^t\}_1^0 \tag{2.47}$$

The $(n+1)$th step weak form formulation of ULFEM, in which body Ω is perturbed with respect to configuration R_n, attaining configuration R_{n+1} becomes:

$$\underbrace{\mathcal{A}_{e=1}^{N_e}\left\{\int_{R_n}\left([\mathbf{B}^e]^T\,\widehat{\mathbf{P}}^e\left(\mathbf{H}^e|_{n+1}^n\right)\right)d\mathrm{V}_n^e\right\}}_{\{\Pi(\mathbf{u})\}_{n+1}^n}=\underbrace{\mathcal{A}_{e=1}^{N_e}\left\{\int_{R_n}\left([\boldsymbol{\phi}^e]^T\,\rho_n^e\,[\boldsymbol{\phi}^e]\,\{\mathbf{b}_h^e\}_{n+1}^n\right)d\mathrm{V}_n^e\right\}}_{\{\mathbf{f}_h^b\}_{n+1}^n}+\underbrace{\mathcal{A}_{e=1}^{N_e}\left\{\int_{\Gamma_{qn}^e}\left([\boldsymbol{\phi}^e]^T\left\{\widehat{\mathbf{P}}^e\left(\mathbf{H}^e|_{n+1}^n\right)\mathbf{N}_n^n\right\}\right)d\mathrm{A}_n^e\right\}}_{\{\mathbf{f}_h^t\}_{n+1}^n} \tag{2.48}$$

which can be written as:

$$\underbrace{\{\Pi(\mathbf{u})\}_{n+1}^n}_{3N_n\times 1}=\underbrace{\{\mathbf{f}_h\}_{n+1}^n}_{3N_n\times 1} \tag{2.49}$$

where $\{\mathbf{f}_h\}_{n+1}^n$ is sum of nodal body forces and nodal traction forces, that is:

$$\{\mathbf{f}_h\}_{n+1}^n=\left\{\mathbf{f}_h^b\right\}_{n+1}^n+\{\mathbf{f}_h^t\}_{n+1}^n \tag{2.50}$$

Chapter 3

RULFEM

3.1 Introduction

The objective of the present chapter is to introduce a method that provides a reasonably general framework for material identification problems without *a priori* assumptions about the constitutive equations, provided the response exhibits incremental linearity. The present method solves an inverse problem and is based on the updated Lagrangian form of FEM; therefore, it is referred to as the reverse updated Lagrangian finite element method (RULFEM). Similar to most existing methods, RULFEM relies on FEM and full-field displacement measurements. However, it does not require a priori constitutive assumptions. Instead, it directly yields the tangent elasticity tensor of each finite element. Because RULFEM generates a coefficient matrix of a linear system of equations, which may have a high condition number, a small random error in the nodal displacement measurements and/or traction vectors may generate erroneous results. Small measurement errors are inevitable even with high-resolution imaging; thus significant errors may occur in the solution of the inverse problem. However, the solution error can be assessed and bounded by errors in the input measured vector fields. The presentation of the RULFEM theory is accompanied by two implementation sections where RULFEM is used to determine elasticity tensors. Both noise-free (theoretical) and noisy (actual) measured displacement and force fields are used in numerical examples to validate the present method. In addition, the capability of RULFEM is evaluated by numerical tools for calculating upper-bound errors.

3.2 Reverse updated Lagrangian finite element method (RULFEM)

The development of the RULFEM theory requires a thorough knowledge of the updated Lagrangian finite element method (ULFEM) formulation. For completeness, a concise derivation of ULFEM is given in the Appendix. RULFEM uses a set of measured full-field displacements and a corresponding set of measured tractions to determine local (element-wise) fourth-order tangent

elasticity tensors without any a priori assumptions about a particular constitutive model. Moreover, RULFEM does not require a cost function or a virtual dis- placement field. The main limitation of the method is that each finite element is assumed to consist of a single uniform material.

A general incrementally linear constitutive framework appropriate for static conditions is presumed. For a given infinitesimal displacement field $\{\mathbf{u}_h\}_{n+1}^n$, the body deforms from configuration R_n to a further deformed configuration R_{n+1}., where the forward ULFEM solve Eq. (2.48) or (2.49) for $\{\mathbf{u}_h\}_{n+1}^n$. The general form of the incremental first Piola–Kirchhoff stress (Eq. (2.14)) can be introduced into Eq. (2.48), provided the incremental steps are sufficiently small for Eq. (2.48) to furnish a meaningful approximation. The Cauchy stress $\mathbf{T}_n^n$ (Eq. (2.11)) in configuration R_n is then related to the first Piola-Kirchhoff stress $\mathbf{P}_{n+1}^n$ at step n by

$$\mathbf{T}_n^n = \left(det\left(\mathbf{F}_n^{n-1}\right)\right)^{-1} \mathbf{P}_n^{n-1} \left(\mathbf{F}_n^{n-1}\right)^T = \frac{1}{J_n^{n-1}} \mathbf{P}_n^{n-1} \left(\mathbf{F}_n^{n-1}\right)^T \tag{3.1}$$

From Eq. (2.14), it follows that the first Piola-Kirchhoff stress in configuration R_{n+1} can be expressed as

$$\mathbf{P}_{n+1}^n = \mathbf{T}_n^n + \mathbb{C}_n \left[\mathbf{H}_{n+1}^n\right] \tag{3.2}$$

It is noted that the Cauchy stress $\overset{\circ}{\mathbf{T}} = \mathbf{T}_0^0$ in the undeformed configuration R_0 represents residual stress. However, the state of stress in subsequent steps, e.g., the step corresponding to deformed configuration R_1, is referred to as the initial stress at step 1, which is the stress in the updated reference configuration.

Using Eqs. (3.2) and (2.34), the stiffness and displacement (the left hand-side) terms in Eq. (2.48) can be expressed as the product of a stiffness matrix $[\mathbf{K}]^n$, a displacement vector of the discretized body $\{\mathbf{u}_h\}_{n+1}^n$ in configuration R_n, and an effective force vector $\{\mathbf{f_T}\}_n^n$ obtained in the previous step, i.e.,

$$\{\Pi(\mathbf{u})\}_{n+1}^n = [\mathbf{K}]^n \{\mathbf{u}_h\}_{n+1}^n + \{\mathbf{f_T}\}_n^n \tag{3.3}$$

where

$$[\mathbf{K}]^n = \mathcal{A}_{e=1}^{N_e} \left[\int_{R_n} \left([\mathbf{B}^e]^T [\mathbb{C}^e]_n [\mathbf{B}^e] \right) d\mathrm{V}_n^e \right] \tag{3.4}$$

and

$$\{\mathbf{f_T}\}_n^n = \mathcal{A}_{e=1}^{N_e} \left[\int_{R_n} \left([\mathbf{B}^e]^T [\mathbf{T}^e]^n \right) d\mathrm{V}_n^e \right] \tag{3.5}$$

In the absence of a residual stress in configuration R0, the force vector $\{\mathbf{f_T}\}_0^0$, which is known from the previous step, is assumed to be zero in the first step.

Substitution of Eq. (3.3) into Eq. (2.48) yields a linear force-stiffness equation containing a $(3N_n \times 3N_n)$ stiffness matrix for the discretization of body Ω by N_e elements with N_n nodes, i.e.,

$$[\mathbf{K}]^n \{\mathbf{u}_h\}^n_{n+1} = \{\mathbf{F}\}^n_n \tag{3.6}$$

where $\{\mathbf{F}\}^n_n = \{\mathbf{f}\}^n_n - \{\mathbf{f_T}\}^n_n$.

In principle, the displacement vector $\{\mathbf{u}_h\}^n_{n+1}$ can be obtained by solving Eq. (3.6), provided the force vector $\{\mathbf{F}\}^n_n$ and the elasticity tensor of each element $[\mathbb{C}^e]_n$ are known, which is required for constructing $[\mathbf{K}]^n$. However, the objective in the reversed problem is to find the components of the elemental elasticity tensor $[\mathbb{C}^e]_n$, which are embedded in $[\mathbf{K}]^n$, for each measured infinitesimal force perturbation $\{\mathbf{f}\}^n_n$ and resulting displacement response $\{\mathbf{u}_h\}^n_{n+1}$. Therefore, a decoupling step is needed to extract the 81 components of $[\mathbb{C}^e]_n$, so that it can be represented as an (81×1) vector $\left\{\mathbb{C}^e_h\right\}_n$ for each element e in Eq. (3.6). That is, $[\mathbf{K}]^n \{\mathbf{u}_h\}^n_{n+1}$ in Eq. (3.6) is rearranged so that the material elasticity tensors $[\mathbb{C}^e]_n$ are decoupled from the remaining geometrical differential operators $[\mathbf{B}^e]$ in Eq. (3.6). This is accomplished by introducing 81 matrices $U_{(9\times9)}$ with ij components equal to 1 and all other components equal to 0, and then define the corresponding column vectors $\langle \mathbf{A}^e \rangle_{ij}$ by

$$\langle A^e \rangle_{ij} \left[\mathbf{C}^e_h\right]^n_{ij} = \left[\int_{R_n} \left([\mathbf{B}^e]^T [\mathbf{U}]_{ij} [\mathbf{B}^e]\right) d\mathrm{V}^e_n\right] \{\mathbf{u}^e_h\}^n_{n+1} \left[\mathbb{C}^e_h\right]_{ij}, \; i, \; j \in \{1, \, 2, \, \ldots, 9\} \tag{3.7}$$

where $\left[\mathbb{C}^e_h\right]_{ij}$ is the unknown ij entry of $\mathbb{C}^e_h$.Then, the column vectors $\langle A^e \rangle_{ij}$ arearranged to form a matrix $\mathbf{A}$.The number of columns in $\mathbf{A}$ is equal to the number of the unknown elements of elasticity tensors. This procedure converts Eq. (3.6) to a system of decoupled equations having as many unknowns as the number of columns of $\mathbf{A}$, i.e.,

$$\left[\langle A^e \rangle_{11} \langle A^e \rangle_{12} \cdots \langle A^e \rangle_{ij} \ldots\right]^n_{n+1} \{\mathbb{C}_h\}_n = \{\mathbf{f}\}^n_n - \{\mathbf{f_T}\}^n_n \tag{3.8}$$

or simply

$$[\mathbf{A}]^n_{n+1} \{\mathbb{C}_h\}_n = \{\mathbf{F}\}^n_n \tag{3.9}$$

It is noted that the system given by Eq. (3.9) is either determined or over-determined. If the condition number of $\mathbf{A}$ is relatively large (e.g., on the order of 10^3 or higher), very small errors in the displacement and force measurements may result in erroneous estimates of the elements of $\{\mathbb{C}_h\}_n$. This issue is discussed later. However, the maximum rank number of $\mathbf{A}$ is equal to the size of the $\{\mathbb{C}_h\}_n$ vector, i.e., the number of independent equations is equal to the number of unknown components of vector $\{\mathbb{C}_h\}_n$.

After the elemental elasticity tensor $\left[\mathbb{C}^e_h\right]_n$ at step n has been obtained, the elemental incremental elasticity tensor $\left[\mathbb{L}^e_h\right]_n$, if desired, can also be derived from Eqs. (2.15) and (2.16).

3.3 Validation criteria and error assessment

The input full-fields of RULFEM (i.e., displacement and traction fields) may contain noise and measurement errors. As with other inverse methods, RULFEM relies on the solution of a

system of equations containing a coefficient matrix **A** characterized by a relatively high condition number. Hence, validation criteria and error assessment in the presence of noisy input data are illustrated for examples involving error-free and noisy input data. In all the validation examples presented below, the MatLab back-slash operator (version 2013b) was used to solve Eq. (3.9). MatLab yields a least-squares solution for the rectangular matrix **A** and solves so-called "over-determined systems" using QR factorization.

The solution to Eq. (3.9) yields as many fourth-order elasticity tensors as the number of elements used to discretize the deformed body. Each fourth-order elemental elasticity tensor is represented by a (9×9) matrix $\left[\mathbb{C}_h^e\right]_n$. Since RULFEM predicts local (element-wise) properties from the solution of a global equation system [Eq. (3.9)], two levels of assessment must be used to validate the method.

The objective of local validation is to compare the predicted components of each $\left[\mathbb{C}_h^e\right]_n$ tensor with actual components. Although a component-wise comparison of matrices might be feasible when dealing with a few finite elements, the comparison is cumbersome when there are many elements. Therefore, it is preferred to assess the accuracy of RULFEM using a single error number. Here, the element error norm $E_i\left(e_i\right)|_{n+1}^n$ is used, which is defined as

$$E_i\left(e_i\right)|_{n+1}^n = \frac{\left\| \left[\mathbb{C}_{RULFEM}^{e_i}\right]_n - \left[\mathbb{C}_{actual}^{e_i}\right]_n \right\|}{\left\| \left[\mathbb{C}_{actual}^{e_i}\right]_n \right\|} \tag{3.10}$$

where e_i refers to the ith element, $\left[\mathbb{C}_{RULFEM}^{e_i}\right]_n$ representing the elasticity tensor $[\mathbb{C}^{e_i}]$ of element e_i predicted by RULFEM at step $n+1$, $\left[\mathbb{C}_{actual}^{e_i}\right]_n$ corresponds to the actual actual $n+1$ elasticity tensor $[\mathbb{C}^{e_i}]$ of element e_i at step $n+1$, and $\|.\|$ is the Euclidean norm of the enclosed matrix.

$$J\left(\{\mathbf{u}_h\}_{n+1}^n, \{\mathbb{C}_h\}_n, \{\mathbf{F}\}_n^n\right) = \left\| [\mathbf{A}]_{n+1}^n \{\mathbb{C}_h\}_n - \{\mathbf{F}\}_n^n \right\| \tag{3.11}$$

Eq. (3.11) yields $J\left(\{\mathbf{u}_h\}_{n+1}^n, \{\mathbb{C}_h\}_n, \{\mathbf{F}\}_n^n\right) = 0$ if and only if equilibrium is satisfied. Thus, EEq. (3.11) can be used to assess the accuracy of the predicted elasticity tensors for a given set of displacement and force data. In practice, however, measurement errors may not lead to exactly zero J values. Consequently, an acceptable J value threshold must be established. Also, a non-zero J value does not necessarily correlate to error in the calculated $\{\mathbb{C}_h\}_n$. Therefore, a more effective means is needed to determine the accuracy of the results obtained with RULFEM.

The error $\Delta\mathbf{A}$ in $[\mathbf{A}]_{n+1}^n$ due to errors in full-field displacement and force measurements, defined by $\Delta\mathbf{u}$ and $\Delta\mathbf{F}$, respectively, yields an error $\Delta\mathbb{C}$ in $\{\mathbb{C}_h\}_n$. In the presence of these errors, Eq. (3.9) can be written as

$$\underbrace{\left([\mathbf{A}]_{n+1}^n + \Delta\mathbf{A}\right)}_{\mathbf{A}} \underbrace{\{\mathbb{C}_h\}_n}_{\mathbb{C}} = \underbrace{\{\mathbf{F}\}_n^n + \Delta\mathbf{F}}_{\mathbf{F}} \tag{3.12}$$

The possible high condition number of **A** and errors in Eq. (3.12) , i.e., $\Delta\mathbf{A}$ and $\Delta\mathbf{A}$, yield an error in the calculation of $\mathbb{C} = \{\mathbb{C}_h\}_n$, denoted by $\Delta\mathbb{C}$. To quantify this error, a residual vector **r** is defined by

$$\mathbf{r} = \mathbf{A}\left(\mathbb{C} + \Delta\mathbb{C}\right) - \mathbf{F} \Rightarrow \Delta\mathbb{C} = \mathbf{A}^{-1}\mathbf{r} \tag{3.13}$$

Applying the Cauchy–Schwarz inequality to Eq. (3.13) and using the definition of the condition number of a matrix, i.e., $cond\,(\mathbf{A}) = \|\mathbf{A}\|\|\mathbf{A}^{-1}\|$, yields

$$\underbrace{\frac{\|\Delta\mathbb{C}\|}{\|\mathbb{C}\|}}_{E_{ac}} \leq \underbrace{cond\,(\mathbf{A})\,\frac{\|\mathbf{r}\|}{\|\mathbf{A}\|\|\mathbb{C}\|}}_{E_{ub}} \tag{3.14}$$

where the left hand-side is the actual error Eac and the right hand-side is the upper-bound error E_{ac} and the right hand-side is the upper-bound error E_{ub}.

From Eqs. (3.11)-(3.14), it follows that $J\left(\{\mathbf{u}_h\}_{n+1}^{n} + \Delta\mathbf{u}, \{\mathbb{C}_h\}_n\,\Delta\mathbb{C}, \{\mathbf{F}\}_n^n + \Delta\mathbf{F}\right) = \|\mathbf{r}\|$. Since the right hand-side of Eq. (3.14), i.e., the upper-bound error E_{ub}, can be readily obtained at each step, it provides a useful way to bound the error in the calculated $\{\mathbb{C}_h\}_n$; moreover, it is a dimensionless number that normalizes the residual (expressed in force units).

A typical approach in material testing is to perturb (deform) the specimen in one or two prescribed directions and use the response to determine the associated bulk material properties. Although Poisson effects are often observed, measurement of the specimen response in directions other than the perturbation directions could be compromised by the sensitivity of the measuring instrument and a small signal-to-noise ratio SNR. This produces different error levels in the components of $\mathbb{C}$, thus requiring additional assessments of the accuracy of the components of $\mathbb{C}$.

Chandrasekaran and Ipsen [6] assessed the accuracy of each component of $\mathbb{C}$ by a component-wise condition number β_i, which pertains to the condition number of the ith column of $\mathbf{A}$ (of size $m \times n$ and minimum rank n, where $m \geq n$), defined as $\|\mathbb{C}\|/|\mathbb{C}_i|$, where $|\mathbb{C}_i|$ is the absolute value of the ith non-zero component of $\mathbb{C}$, and defined β_i as

$$\beta_i \cong \|\mathbf{A}\|.\|\mathbf{q}_i\|, \quad 1 \leq i \leq n \tag{3.15}$$

where $\mathbf{q}_i^T$ is the ith row of matrix $\mathbf{A}^{\dagger} = \left(\mathbf{A}^T\mathbf{A}\right)^{-1}\mathbf{A}^T$.

3.4 Validation of RULFEM for noise-free input data

The capability of the present method is demonstrated in this section by three examples in which the input measurement (force and displacement) fields are not obtained from actual measurements; instead they are generated from a forward FEM analysis of a body with known elasticity tensors and prescribed displacement perturbations. These fields are regarded as effectively noise-free and are used to validate the RULFEM formulation. The first two examples are designed to validate the method for simple geometries with one ele- ment through the body thickness, whereas in the third example, the body is discretized by three elements in each direction, i.e., a total of 27 finite elements.

Example 1: A numerical experiment involving two simple materials and a simple specimen geometry is presented first for illustrative purposes. In this example, a solid body of dimensions

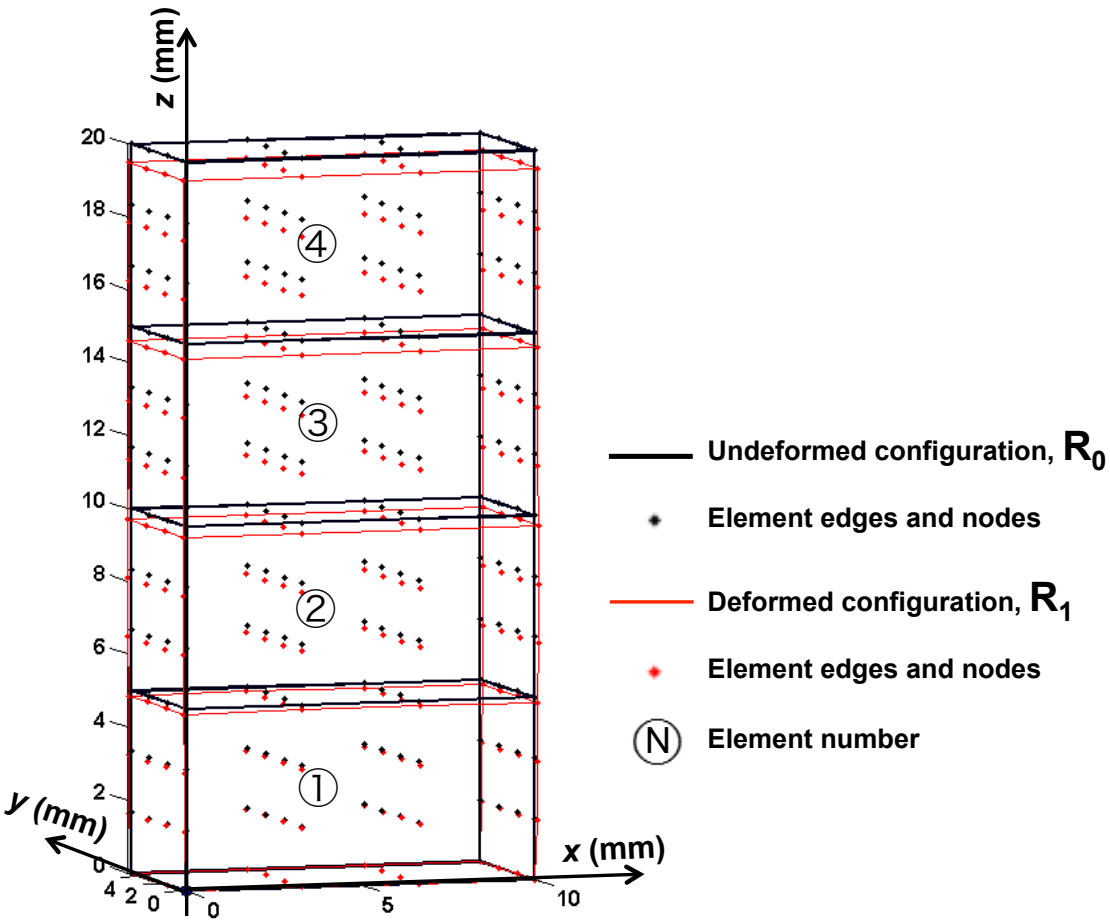

Figure 3.1: A specimen meshed with four 64-node hexagonal elements. Reference (undeformed) configuration R_0 and deformed configuration R_1 due to uniform displacement of all nodes at $z = 20mm$ by $u_z = -0.1mm$ are shown by black and red lines, respectively (magnification = ×10). (Color figure online)

5 mm ×10 mm ×20 mm is meshed with four 64-node hexagonal elements having a total of 208 nodes (Fig. 3.1). The reference configuration R_0 (black lines) is free of residual stress and all nodes at $z = 0$ are fully constrained. Deformation due to uniform static displacement $u_z = -0.1$ mm of all specimen nodes at $z = 20$ mm produces a new body configuration R_1 (red lines). The body is assumed to consist of two materials. The lower half of the body (i.e., from $z = 0$ to 10 mm) consists of an elastic material with Saint Venant–Kirchhoff constitutive model, i.e.,

$$\mathbf{S} = \lambda \, \mathrm{tr}\,(\mathbf{E})\,\mathbf{I} + 2\mu\,\mathbf{E} \tag{3.16}$$

with Lamé constants $\lambda = 3103$ MPa and $\mu = 345$ MPa, thus

$$\mathbb{L}_0\left[\mathbf{E}|_1^0\right] = \lambda \, \mathrm{tr}\left(\mathbf{E}|_1^0\right)\mathbf{I} + 2\mu\,\mathbf{E}|_1^0 \tag{3.17}$$

whereas the upper half of the body (from $z = 10$ to 20 mm) consists of an orthotropic material with normal and shear moduli $E_{xx} = 1,000$ MPa, $E_{yy} = 1,250$ MPa,$E_{zz} = 1,500$ MPa, $G_{xy} = 300$ MPa, $G_{yz} = 450$ MPa, and $G_{zx} = 550$ MPa, and Poisson's ratio $\nu_{xy} = 0.3$, $\nu_{yz} = 0.4$, and $\nu_{xz} = 0.45$, with all other Poisson's ratios calculated from the relations $\nu_{zy} = \nu_{yz}E_{zz}/E_{yy}$, $\nu_{zx} = \nu_{xz}E_{zz}/E_{xx}$, and $\nu_{yx} = \nu_{xy}E_{yy}/E_{xx}$.

For the present example and zero residual stress (i.e., $\mathring{\mathbf{T}} = \mathbf{0}$), Eq. (3.9) reduces to

$$[\mathbf{A}]_1^0 \{\mathbb{C}_h\}_0 = \{\mathbf{F}\}_0^0 \tag{3.18}$$

where the force vector $\{\mathbf{F}\}_0^0$ and the displacement vector $\{\mathbf{u}\}_1^0$, calculated from a forward FEM analysis, play the role of the measured quantities in an actual experiment.

For $\mathring{\mathbf{T}} = \mathbf{T}_0^0 = \mathbf{0}$, Eqs. (2.13) and (2.14) give

$$\mathbf{P}_1^0 = \mathbb{C}_0 \left[\mathbf{H}_1^0\right] = \mathbb{L}_0 \left[\mathbf{E}_1^0\right] \tag{3.19}$$

The actual elemental elasticity tensors $\left[\mathbb{C}^e_{actual}\right]_0$ of the two materials, which are used as inputs in the forward FEM analysis, are

$$\left[\mathbb{C}^{e_1,e_2}_{actual}\right]_0 = \begin{bmatrix} 3793 & 0 & 0 & 0 & 3103 & 0 & 0 & 0 & 3103 \\ 0 & 345 & 0 & 345 & 0 & 0 & 0 & 0 & 0 \\ 0 & 0 & 345 & 0 & 0 & 0 & 345 & 0 & 0 \\ 0 & 345 & 0 & 345 & 0 & 0 & 0 & 0 & 0 \\ 3103 & 0 & 0 & 0 & 3793 & 0 & 0 & 0 & 3103 \\ 0 & 0 & 0 & 0 & 0 & 345 & 0 & 345 & 0 \\ 0 & 0 & 345 & 0 & 0 & 0 & 345 & 0 & 0 \\ 0 & 0 & 0 & 0 & 0 & 345 & 0 & 345 & 0 \\ 3103 & 0 & 0 & 0 & 3103 & 0 & 0 & 0 & 3793 \end{bmatrix} \text{ MPa} \tag{3.20}$$

$$\left[\mathbb{C}^{e_3,e_4}_{actual}\right]_0 = \begin{bmatrix} 3517 & 0 & 0 & 0 & 2807 & 0 & 0 & 0 & 3721 \\ 0 & 900 & 0 & 900 & 0 & 0 & 0 & 0 & 0 \\ 0 & 0 & 600 & 0 & 0 & 0 & 600 & 0 & 0 \\ 0 & 900 & 0 & 900 & 0 & 0 & 0 & 0 & 0 \\ 2807 & 0 & 0 & 0 & 3788 & 0 & 0 & 0 & 3713 \\ 0 & 0 & 0 & 0 & 0 & 1100 & 0 & 1100 & 0 \\ 0 & 0 & 600 & 0 & 0 & 0 & 600 & 0 & 0 \\ 0 & 0 & 0 & 0 & 0 & 1100 & 0 & 1100 & 0 \\ 3721 & 0 & 0 & 0 & 3713 & 0 & 0 & 0 & 5794 \end{bmatrix} \text{ MPa} \tag{3.21}$$

where superscripts $e_i = 1 - 4$ indicate the elements shown in Fig. 3.1.

The elasticity vector $\{\mathbb{C}_h\}_0$, obtained with RULFEM by solving the inverse problem [Eq. (3.18)], is converted to the following matrix form $\left[\mathbb{C}^e_{RULFEM}\right]_0$ of the elasticity tensor for elements 1 – 4:

$$\left[\mathbb{C}^{e_1,e_2}_{RULFEM}\right]_0 = \begin{bmatrix} 3.793 & 0.000 & 0.000 & -0.00 & 3.103 & -0.00 & -0.00 & 0.000 & 3.103 \\ -0.00 & 0.345 & -0.00 & 0.345 & 0.000 & 0.000 & 0.000 & -0.00 & 0.000 \\ 0.000 & 0.000 & 0.345 & 0.000 & 0.000 & 0.000 & 0.345 & 0.000 & -0.00 \\ 0.000 & 0.345 & -0.00 & 0.345 & 0.000 & 0.000 & 0.000 & -0.00 & -0.00 \\ 3.103 & 0.000 & 0.000 & 0.000 & 3793 & -0.00 & -0.00 & 0.000 & 3.103 \\ -0.00 & -0.00 & -0.00 & -0.00 & -0.00 & 0.345 & 0.000 & 0.345 & 0.000 \\ 0.000 & -0.00 & 0.345 & 0.000 & -0.00 & 0.000 & 0.345 & -0.00 & -0.00 \\ 0.000 & 0.000 & 0.000 & 0.000 & -0.00 & 0.345 & -0.00 & 0.345 & -0.00 \\ 3.103 & -0.00 & -0.00 & -0.00 & 3.103 & -0.00 & 0.000 & -0.00 & 3.793 \end{bmatrix} \times 10^3 \text{ MPa} \tag{3.22}$$

$$\left[\mathbb{C}^{e_3,e_4}_{RULFEM}\right]_0 = \begin{bmatrix} 3.517 & 0.000 & 0.000 & 0.000 & 2.807 & 0.000 & 0.000 & 0.000 & 3.721 \\ -0.00 & 0.900 & -0.00 & 0.900 & -0.00 & -0.00 & -0.00 & -0.00 & -0.00 \\ -0.00 & 0.000 & 0.600 & -0.00 & 0.000 & 0.000 & 0.600 & 0.000 & -0.00 \\ -0.00 & 0.900 & 0.000 & 0.900 & -0.00 & -0.00 & -0.00 & -0.00 & -0.00 \\ 2.807 & 0.000 & -0.00 & 0.000 & 3.788 & -0.00 & -0.00 & -0.00 & 3.713 \\ 0.000 & -0.00 & -0.00 & 0.000 & 0.000 & 1.100 & -0.00 & 1.100 & 0.000 \\ 0.000 & -0.00 & 0.600 & -0.00 & 0.000 & -0.00 & 0.600 & -0.00 & -0.00 \\ 0.000 & 0.000 & 0.000 & 0.000 & -0.00 & 1.100 & -0.00 & 1.100 & -0.00 \\ 3.721 & -0.00 & 0.000 & 0.000 & 3.713 & -0.00 & 0.000 & -0.00 & 5.794 \end{bmatrix} \times 10^3 \text{ MPa} \tag{3.23}$$

A comparison of the components of the above matrices [Eqs. (3.20)– (3.23)) attests to the accuracy of the RULEFM analysis. The accuracy of the predicted components of each elasticity tensor can also be determined in terms of the element error norm $E_i\,(e_i)$ [Eq. (3.10). The error norms of elements 1–4 shown in Fig. 3.1, obtained from Eq. (3.10), are $E_1\,(e_1) = 3.1 \times 10^{-12}$, $E_1\,(e_2) = 1.9 \times 10^{-12}$, $E_1\,(e_1) = 9.7 \times 10^{-12}$, and $E_1\,(e_1) = 5.6 \times 10^{-12}$. These extremely small error values lend further support to RULFEM.

It is noted that Eq. (3.19) not only holds in the present numerical experiment but also represents the first step of analysis in the general case of consecutive perturbations. After n increments, the nodal Cauchy stresses are not zero, and Eq. (2.11) can be used to determine the Cauchy stress tensor $\mathbf{T}$. However, the elasticity tensor $\mathbb{C}$ remains constant in subsequent analysis steps of this example because the constitutive model is assumed to be linear [Eq. (3.19)].

Example 2: The previous example illustrates the validity of RULFEM for a specimen with a simple geometry consisting of two different materials subjected to one linear perturbation step. The present example demonstrates the capability of RULFEM to accurately predict the elasticity tensor of a tensile specimen (Fig. 3.2) with its gauge section undergoing elastic-plastic deformation in three linear steps. Because of symmetry in loading (uniform tension) and the specimen geometry, only one-half of the specimen is analyzed. The mesh consists of five 64-node hexagonal elements having a total of 256 nodes. All base nodes ($z = 0$) are fully constrained. Uniform tensile loading is modeled by incrementally displacing the nodes at $z = 20$ mm by a total dis-

placement u_z = 0.028, 0.0739, 0.0948, and 0.1558 mm. The original stress-free configuration and four consecutive deformed configurations of the specimen are denoted by R_0, R_1, R_2, R_3, and R_4, respectively. A piece-wise linear plastic response is modeled by changing the elastic modulus and Poisson's ratio when ε_z = 0.002, 0.0065, 0.009, and 0.02 (3.1). Stress-strain calculations (3.1) give the engineering stress-strain response shown in Fig. 3.3. Forward FEM analysis yields four displacement vectors and four associated reaction vectors used as input in RULFEM, in effect serving as surrogates of experimentally measured vectors. Because of the piece-wise linear material properties, RUFEM results are independent of perturbation size (only in this example case). At each step, RULFEM predicts five elasticity tensors (one per element), yielding a total of 20 elasticity tensors. Instead of explicitly comparing 20 actual elasticity tensors with 20 predicted elasticity tensors, the validity of RULFEM is assessed by the element error norm $E_i\,(e_i)$ [Eq. (3.10)]. The maximum $E_i\,(e_i)$ is less than $< 1.8 \times 10^{-12}$ (Fig. 3.4), which confirms the accuracy of all elemental elasticity tensors of the elastic-plastically deformed specimen determined by RULFEM.

Step	Material properties		Strain range	Displacement (mm)	
	E (MPa)	ν	$\Delta\varepsilon$	Δu_z	u_z
1	70,000	0.330	0.0–0.002	0.0280	0.0280
2	34,240	0.499	0.002–0.0065	0.0459	0.0739
3	880	0.499	0.0065–0.0099	0.0209	0.0948
4	397	0.499	0.0099–0.020	0.0610	0.1558

Table 3.1: Dependence of material properties on strain range and corresponding displacement increment and total displacement uniformly applied to all specimen nodes at z = 20 mm

Example 3: The previous two examples illustrate the accuracy of RULFEM for elastic and plastic materials. However, the specimen geometries in the former examples are discretized with only one element through the specimen thickness. Using only one element through the body thickness implies that the elements share nodes at their common interface (e.g., see Figs. 3.1 and 3.2). Hence, each 64-node element has either 48 or 56 independent nodes, i.e., 144 or 168 DOF, depending on whether it is a middle element or an end element. As discussed in Sect. 2.2, the minimum number of independent DOF needed to determine all members of an elemental elasticity tensor is 81. Although these additional DOF are redundant in the case of simple problems, such as those of the previous two examples, these additional DOF may become necessary when dealing with high mesh densities in three directions. In particular, the number of independent nodes or DOF of an element that is completely surrounded by other elements (referred to as domain middle elements) is 28 nodes or 84 DOF. These three additional DOF (or equations) can be used to improve the condition number of $\mathbf{A}$. To illustrate this case, a specimen geometry similar to that of example 2 (Fig. 3.2) was discretized by a total of 27 64-node elements, using 3 elements in each direction (Fig. 3.5). This specimen consists of an elastic material with Lamé constants $\lambda = 115,380$ MPa and $\mu = 76,923$ MPa (i.e., $E = 200,000$ MPa and $\nu = 0.3$), which are typical of steel. RULFEM yields 27 elasticity tensors (one tensor per element), with all element error norms $E_i\,(e_i)$ [Eq. (3.10)] less

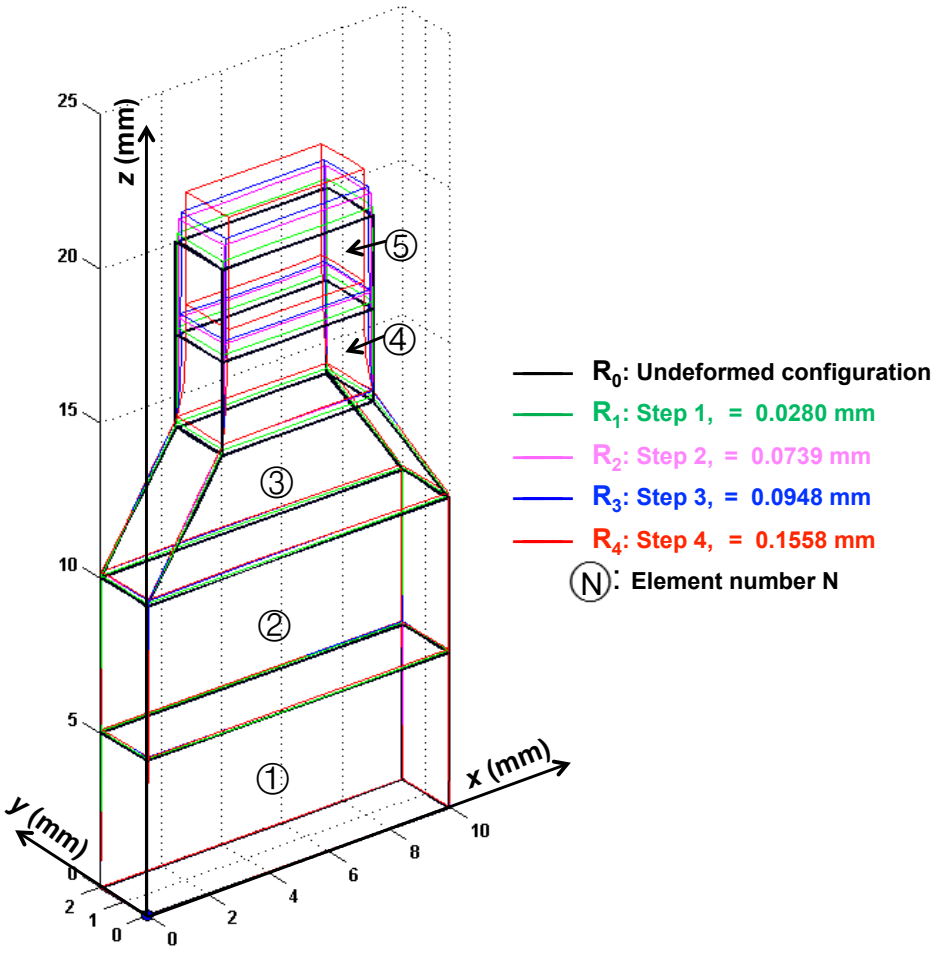

Figure 3.2: The specimen of example 2 is discretized by five 64-node hexagonal elements. All nodes at $z = 0$ are fully constrained, whereas all nodes at $z = 20$ mm are uniformly displaced in the z-direction in four displacement increments $\Delta u_z = 0.0280$, 0.0459, 0.0209, and 0.0610 mm, resulting in a total displacement $u_z = 0.1558$ mm. The reference (undeformed) configuration R_0 is shown with black lines, whereas deformed configurations corresponding to each incremental step R_1, R_2, R_3, and R_4 are shown with green, magenta, blue, and red lines, respectively. Configuration R_1 represents linear elastic deformation, whereas R_2, R_3, and R_4 configurations represent sequential linear-plastic deformations following the material response shown in Fig. 3.3. Yielding commences when all top nodes are displaced by $u_z = 0.0280$ mm, i.e., $\varepsilon_z = 0.002$ (magnification = 10×).

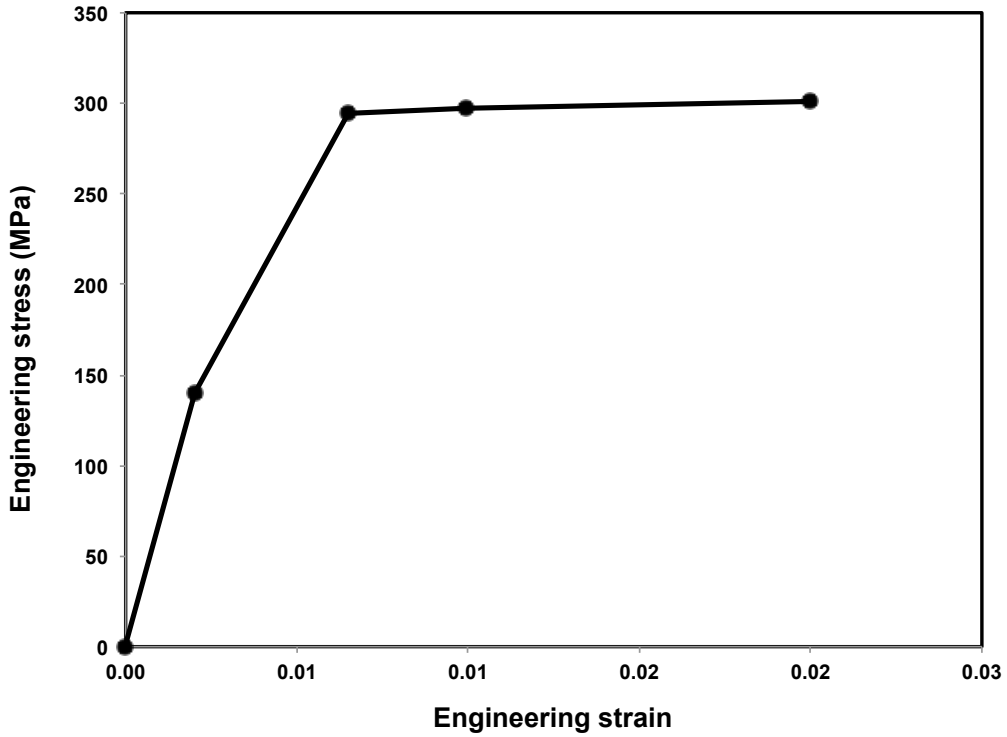

Figure 3.3: Engineering stress-strain response of the elastic-plastic specimen of example 2

than 3.5×10^{-11} (Fig. 3.6). These very small values of $E_i\,(e_i)$ illustrate the accuracy of RULFEM analysis of bodies meshed with several through-thickness elements.

3.5 Validation of RULFEM for noisy input data

The geometry and finite element discretization of example 2 (Fig. 3.2) are used in the following three example cases to assess the performance of RULFEM for noisy input displacement and force full-field vectors. In all these examples, the specimen nodes at $z = 0$ are fully constrained and a uniform perturbation $u_z = 0.1$ mm is applied to the nodes at $z = 20$ mm. The required input data fields (i.e., displacement and force full-field vectors) were obtained by solving each example using linear FEM analysis. Differences in elemental material properties (elasticity tensors) result in different displacement and force field vectors for each example case, as discussed below.

A white Gaussian noise signal generator function, referred to as "add white Gaussian noise" (AWGN; MatLab R2013b, MathWorks, Inc., Natick, MA) was used to introduce different levels of noise to error-free displacement and force full-field vectors obtained from input noise-free forward FEM analysis. AWGN generates noisy discrete vectors by using as input a noise-free vector and a given SNR.

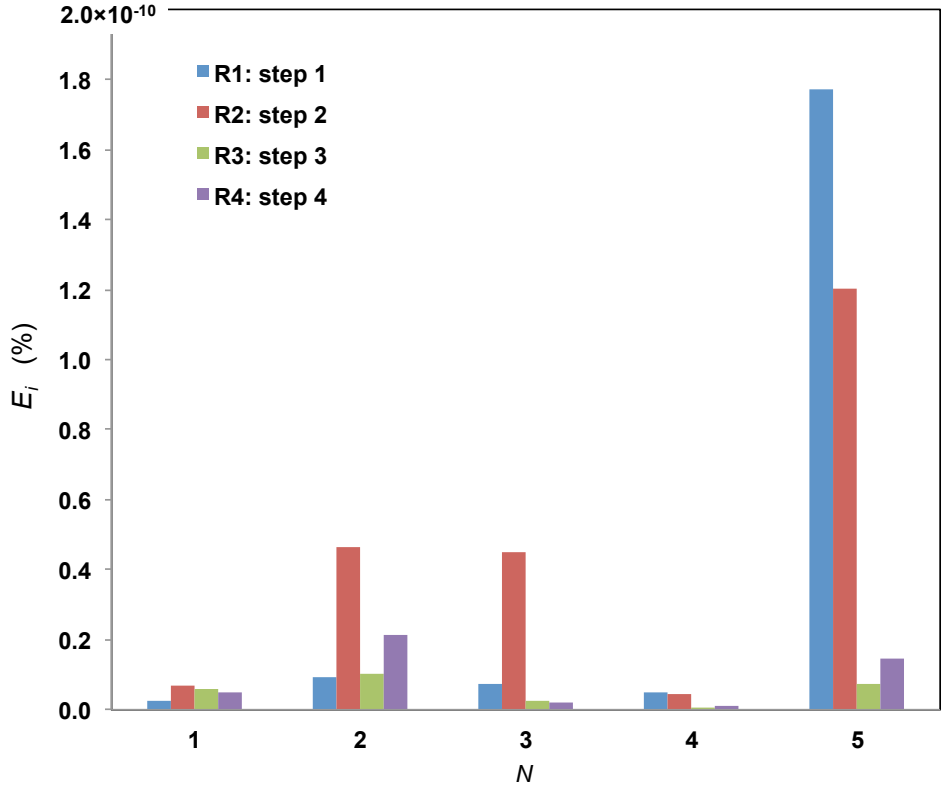

Figure 3.4: Element error norm E_i of the elements used to discretize the specimen of example 2. All E_i values are $< 1.8 \times 10^{-12}$, which confirms the accuracy of all elemental elasticity tensors of the plastically deformed specimen obtained with RULFEM.

The first step of a RULFEM analysis involving noisy input vector fields is to calculate the elemental elasticity tensors (i.e., $\mathbb{C}$) by solving Eq. (3.12). In each of the following three examples, the accuracy of RULFEM is examined for $15^2 = 225$ combinations (pairs) of displacement and force fields, specifically 15 different SNR_u values for displacement fields and 15 different SNR_f values for force fields. AWGN produces overall controlled noise levels with random local errors in displacement and force fields for given SNR_u and SNR_f . To ensure that the RULFEM results depend on the overall noise level and not the noise location in the body, RULFEM analysis was performed 15 times for each SNR pair.

Actual errors are determined by E_i [Eq. (3.10)] and E_{ac} [Eq. (3.14)]. For each displacement-force field pair, the first method produces one E_i value for each element used to discretize the body. Because of the 15 repetitions for each input pair, error tracking for each element is cumbersome; therefore, the maximum elemental error among all elements was selected for each RULFEM analysis or SNR pair. The average of the 15 repetitions and corresponding standard deviation (STD) for each displacement-force pair are plotted for each example. However, because the second method (based on E_{ac}) produces a single overall error level, the average and STD data of the 15 repetitions

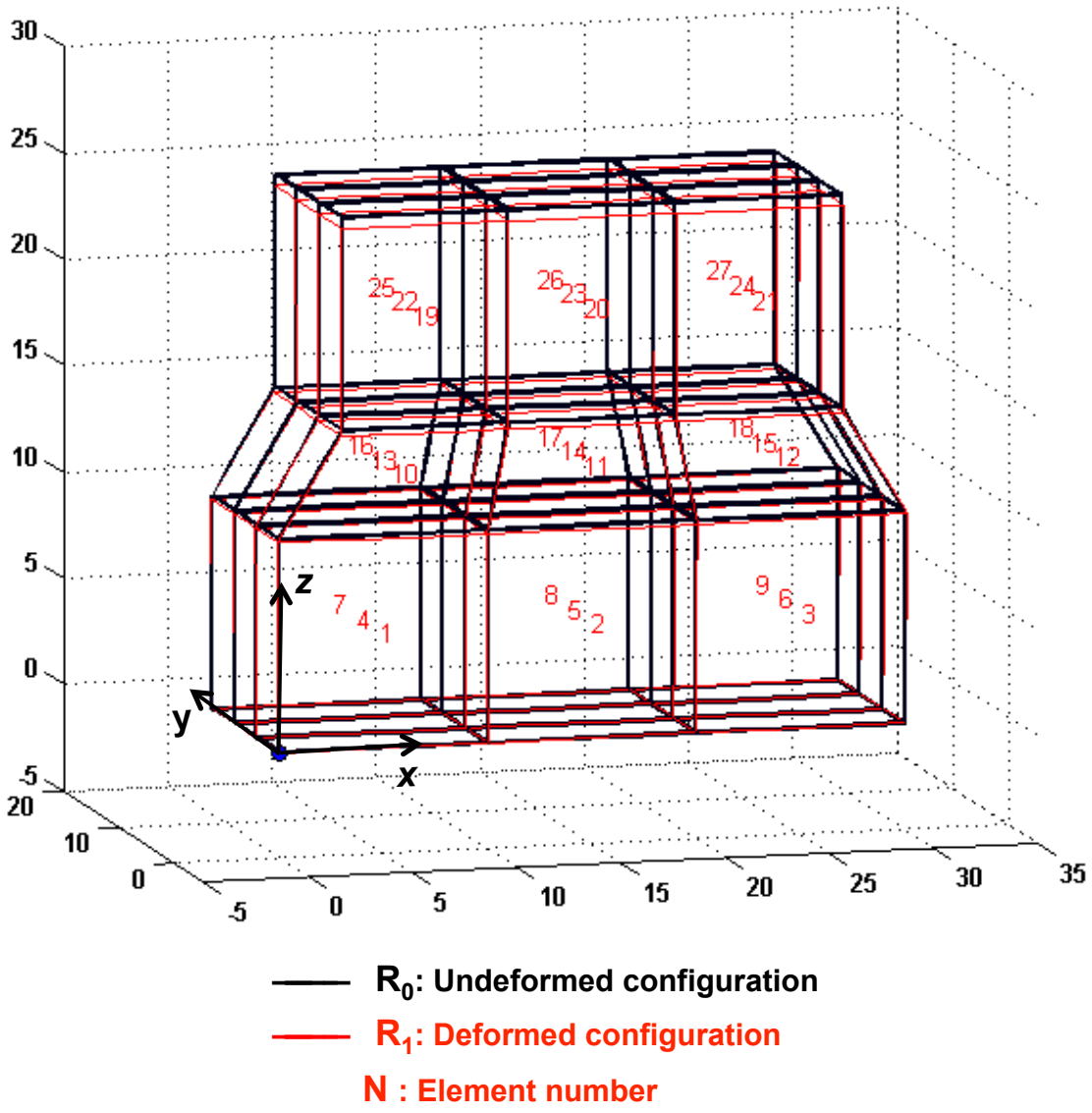

Figure 3.5: The specimen of example 3 is discretized by three 64-node elements in each direction, resulting in 27 hexagonal elements. All nodes at $z = 0$ are fully constrained, whereas all nodes at $z = 25$ mm are uniformly displaced by $u_z = -0.1$ mm. The reference configuration R_0 (black lines) is the undeformed configuration, whereas the deformed configuration R_1 (red lines) represents linear elastic deformation. Red numbers indicate the number of through-thickness elements. Element 14 has only 28 independent nodes (i.e., 84 independent DOF), while all other elements have a higher number of independent DOF in the RULFEM analysis (magnification = 10×).

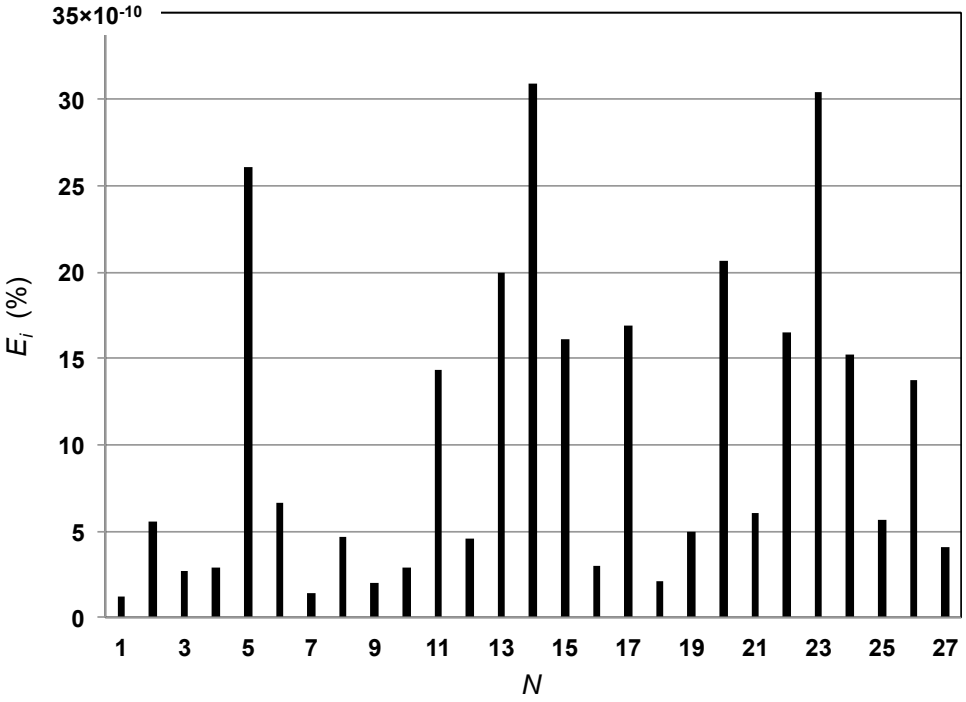

Figure 3.6: Element error norm E_i versus element number N for the specimen of example 3. All $E_i$values are $< 3.5 \times 10^{-11}$, confirming the accuracy of all elemental elasticity tensors obtained with RULFEM

are plotted for each example. These two error assessment methods can be applied only if the actual elemental material elasticity tensors are known, as in the following three examples. The purpose of calculating these actual error levels is to validate the proposed upper-bound error E_{ub} [Eq. (3.14)]. β_i [Eq. (3.15)] is also calculated for one particular SNR pair (i.e., $SNR_u = 135$ and $SNR_f = 87$S) in example 6.

Example 4: All five elements (Fig. 3.2) consist of an isotropic material with $E = 200,000$ MPa and $\nu = 0.3$. Forward FEM analysis using the aforementioned boundary conditions yields the error-free displacement and force full-field vectors. Figures 3.7, 3.8, and 3.9 show E_i , E_{ac}, E_{ub}, and corresponding STD values calculated 15 times for each SNR_f and SNR_u pair.

Example 5: All five elements (Fig. 3.2) consist of an isotropic material, but elements 1–4 have $E = 200,000$ MPa and $\nu = 0.3$, whereas element 5 has $E = 150,000$ MPa and $\nu = 0.4$. Figures 3.10, 3.11, and 3.12 show E_i , E_{ac}, E_{ub}, and corresponding STD values calculated 15 times for each SNR_f and SNR_u pair.

Example 6: Element 1 consists of an isotropic material with $E = 200,000$ MPa and $\nu = 0.3$, whereas elements 2–5 consist of different 3D orthotropic materials with elastic modulus given in Table 3.2, shear modulus equal to one-half of their corresponding elastic modulus, and identical

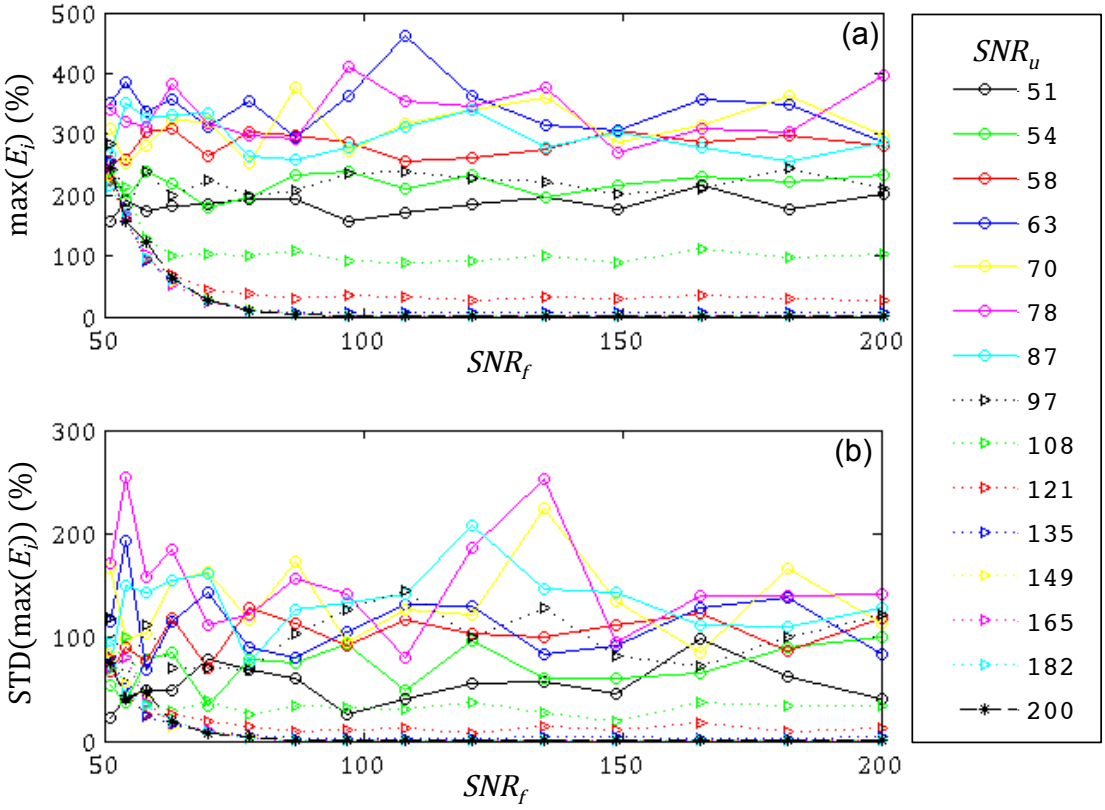

Figure 3.7: **a** Average and **b** standard deviation of maximum element error norm E_i of the elements used to discretize the specimen of example 4 versus signal-to-noise ratio SNR_u and SNR_f for 15 repetitions of 225 displacement and force full-fields

Poisson's ratios of $\nu_{xy} = 0.3$, $\nu_{yz} = 0.225$, and $\nu_{xz} = 0.15$ (Fig. 3.2). Figures 3.13, 3.14, and 3.15 show E_i , E_{ac}, E_{ub}, and corresponding STD values calculated 15 times for each SNR_f and SNR_u pair.

Elastic Modulus (MPa)	Element			
	2	3	4	5
E_{xx}	140,000	180,000	100,000	60,000
E_{yy}	105,000	135,000	75,000	45,000
E_{zz}	70,000	90,000	50,000	30,000

Table 3.2: Directional elastic modulus of finite elements 2–5 in example 6

Figures 3.7, 3.10, and 3.13 show that the actual error in the material elasticity tensors is very large for those measured displacement and force fields with low SNR_u and SNR_f levels. However,

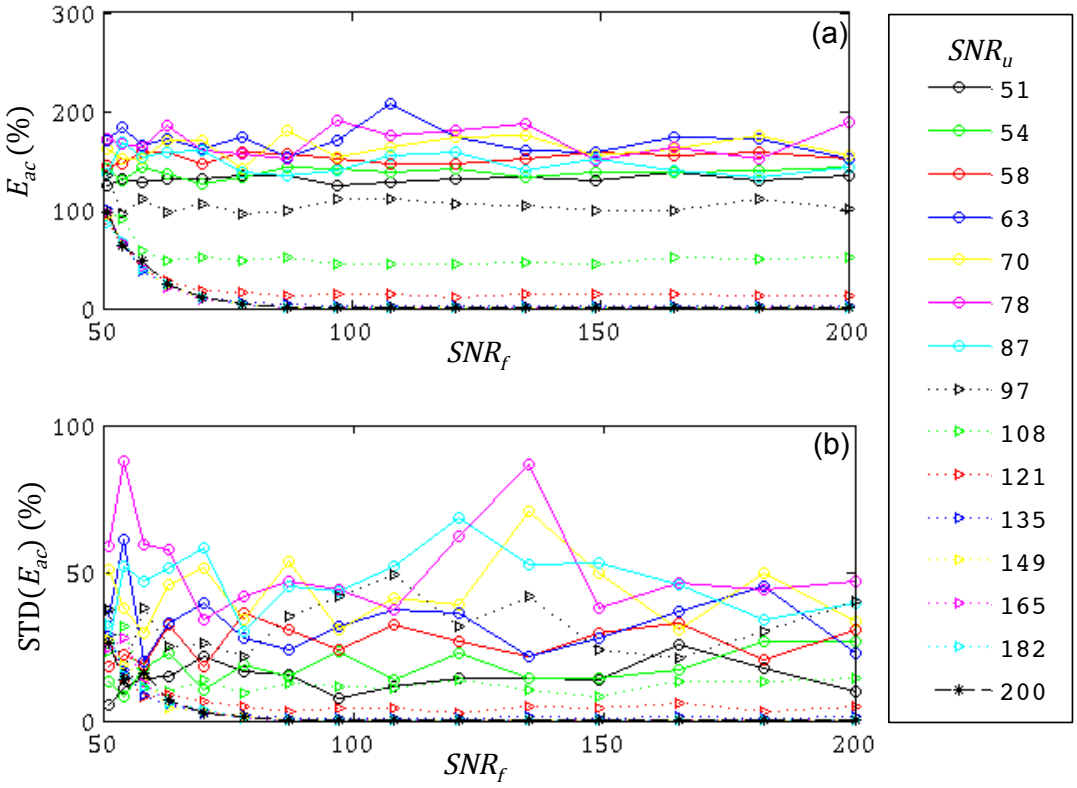

Figure 3.8: **a** Average and **b** standard deviation of maximum element error norm E_{ac} of the elements used to discretize the specimen of example 4 versus signal-to-noise ratio SNR_u and SNR_f for 15 repetitions of 225 displacement and force full-fields

all three examples show reasonable levels of E_i for $SNR_u > 135$ and $SNR_f > 85$. Table 3.3 gives the maximum E_i and corresponding E_{ub} and E_{ac} for each example case.

To assess the accuracy of the RULFEM predictions by the component-wise condition number of the system [Eq. (3.15)], in example 6, β_I is calculated for all 405 elements of $\mathbb{C}$ for one pair of noisy inputs of $SNR_f = 85$ and $SNR_u = 137$. Figure 3.16 shows β_i , normalized by the condition number of $\mathbf{A}$, i.e., $cond(A) = 9.2 \times 10^4$, versus the i th component number of $\mathbb{C}$. The local error E^i_{loc} of the ith nonzero component of $\mathbb{C}$, defined as

$$E^i_{loc} = \frac{|\mathbb{C}^i_{RULFEM} - \mathbb{C}^i_{actual}|}{|\mathbb{C}^i_{actual}|} \tag{3.24}$$

where $\mathbb{C}^i_{actual}$ is the ith nonzero component of $\mathbb{C}_{actual}$ and $\mathbb{C}^i_{RULFEM}$ is the ith component obtained with RULFEM is shown in Fig. 3.17 together with the corresponding $\beta_i/cond(A)$ versus the ith component number of $\mathbb{C}$. $\mathbb{C}_{actual}$ has 405 components (5 elements and 81 components per elasticity tensor) of which only 105 are nonzero. Only a few nonzero components with local errors

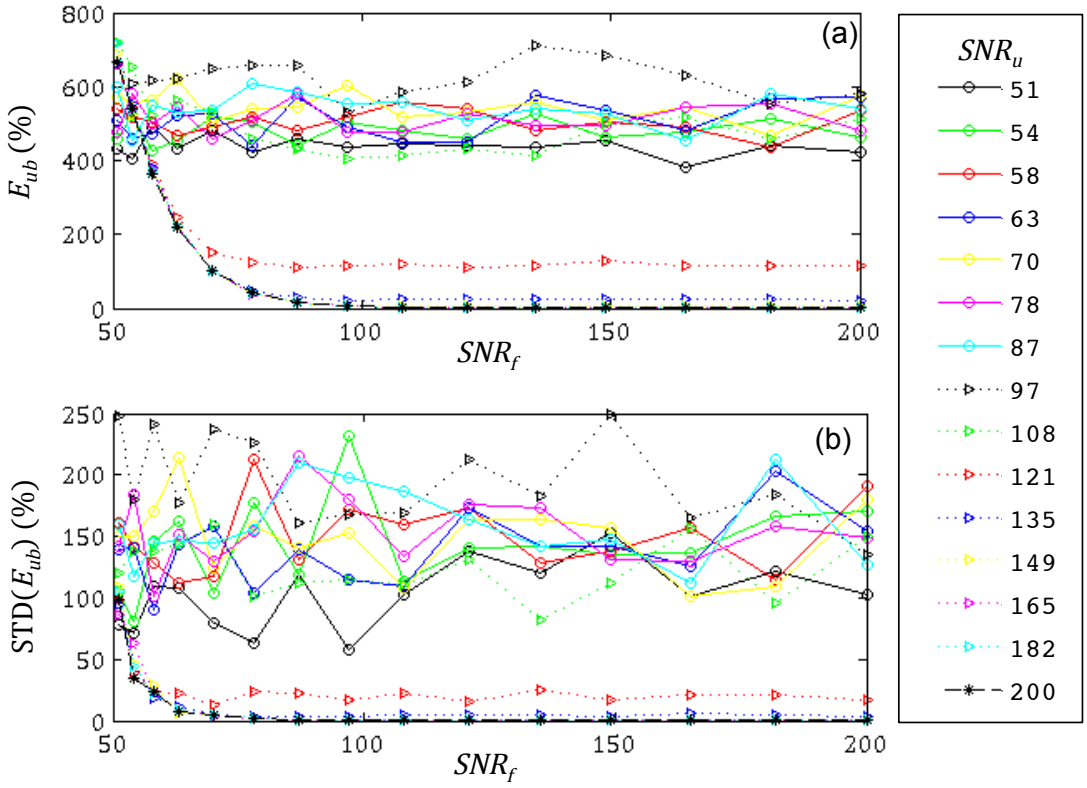

Figure 3.9: **a** Average and **b** standard deviation of maximum element error norm E_{ub} of the elements used to discretize the specimen of example 4 versus signal-to-noise ratio SNR_u and SNR_f for 15 repetitions of 225 displacement and force full-fields

$>$ 10% exist (Fig. 3.17). Although the calculated β_i values can be used to identify the erroneous components of β_i, they do not correspond to actual local errors.

3.6 Discussion

Previous material identification methods (i.e., FEMU, CEGM, VFM, EGM, and RGM) and the present method (RULFEM) all employ balance laws of mechanics, require as input measured full-field or partial-field quantities (i.e., displacement and force fields), and rely on numerical techniques, such as finite differences and FEM. However, the major difference between RULFEM and previous methods is that RULFEM does not require any assumption about the constitutive response of the material beyond incremental linearity. The implementation of FEM with RULFEM yields the material elasticity tensor of each element used to define the body, whereas all of the aforementioned methods (except VFM) solve for the material constants within the framework of an a

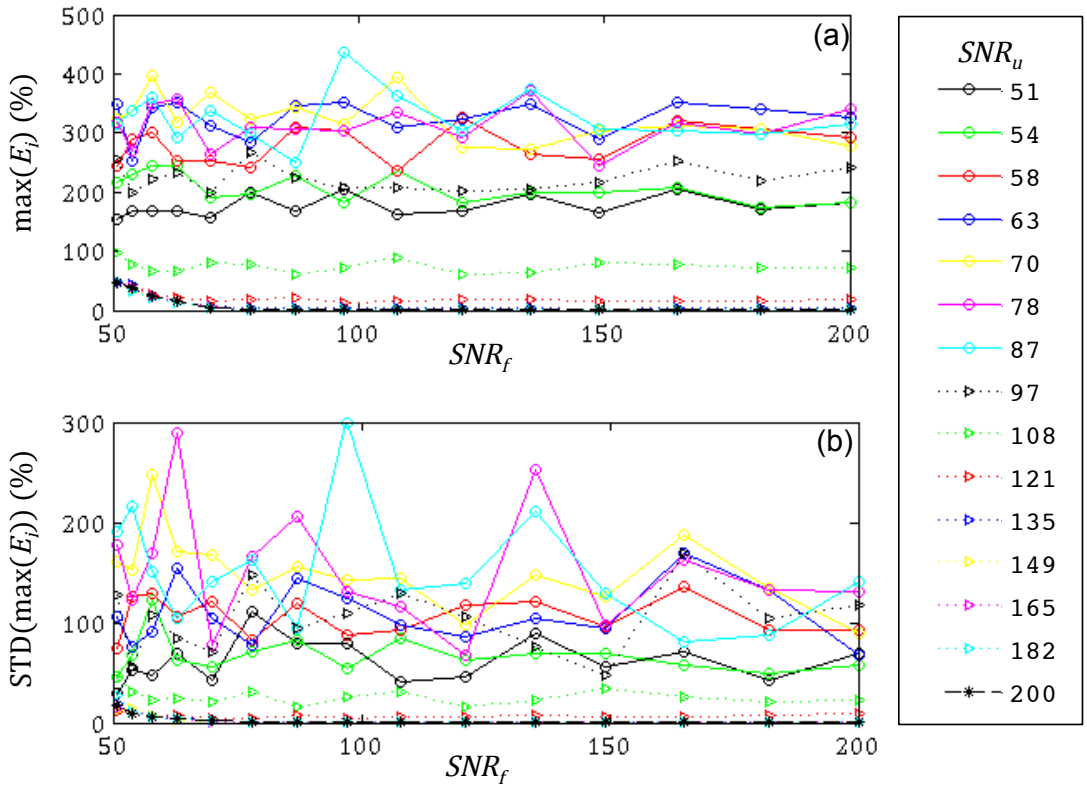

Figure 3.10: **a** Average and **b** standard deviation of maximum element error norm E_i of the elements used to discretize the specimen of example 5 versus signal-to-noise ratio SNR_u and SNR_f for 15 repetitions of 225 displacement and force full-fields

priori assumed constitutive model. However, VFM requires the determination of a particular (virtual) displacement field, which must be optimized to obtain fairly accurate results. Although VFM has been successfully applied to several types of materials, its application to finely discretized or irregularly shaped bodies presents particular challenges [1].

In addition to a priori assumptions, most of the existing methods use nonlinear cost functions, which are subjected to a set of constraint equations, and optimization techniques to obtain a solution. For a given set of constraint equations and in the presence of more than one local minimum, an accurate solution is not feasible. Therefore, a priori constitutive models and solution of the constraint equations based on a specific boundary value problem do not necessarily yield the actual constitutive model applicable to any other boundary- value problems.

RULFEM does not solve a nonlinear cost function but rather a linear system of equations [Eq. (3.12)]. More importantly, in contrast to other material identification methods, RULFEM does not require a priori assumptions about the constitutive material model. In fact, the elasticity tensors cal- culated in each step provide a basis for determining material constitutive models.

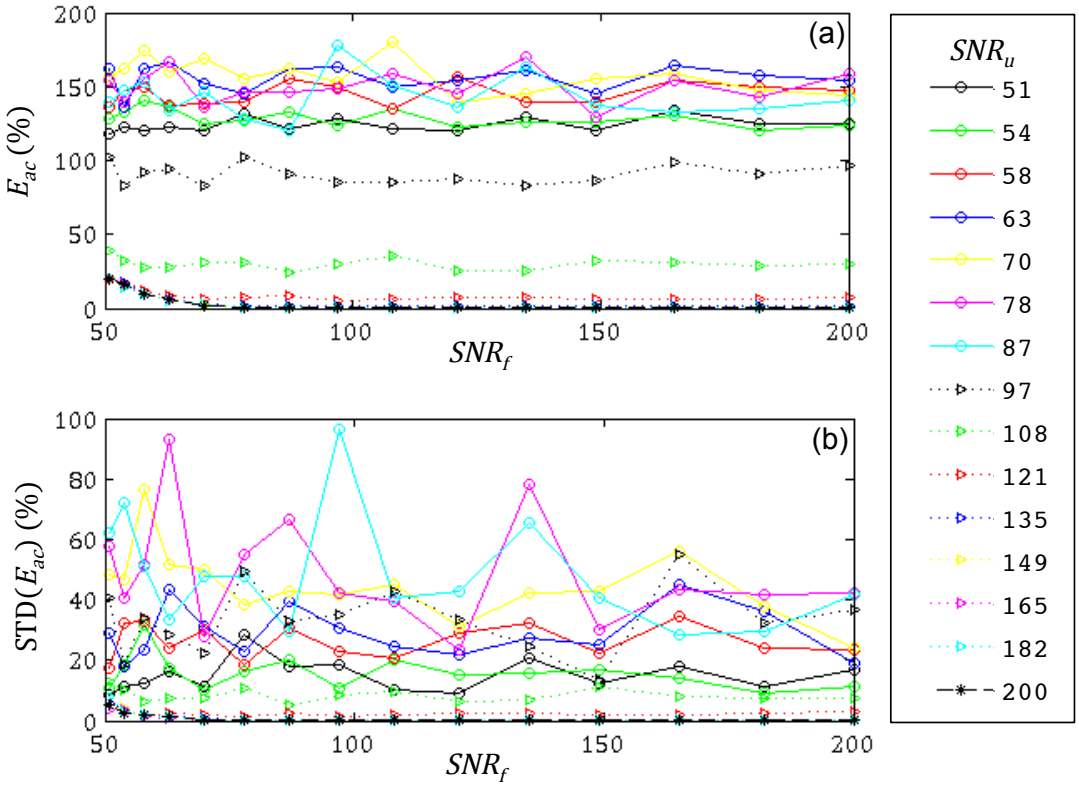

Figure 3.11: **a** Average and **b** standard deviation of maximum element error norm E_{ac} of the elements used to discretize the specimen of example 5 versus signal-to-noise ratio SNR_u and SNR_f for 15 repetitions of 225 displacement and force full-fields

Instabilities are not uncommon to the systems of equa- tions that characterize inverse problems. Material identifica- tion methods, including RULFEM, are not immune to this problem. In particular, the assembled **A** matrix [Eq. (3.12)] may have a high condition number. Each column of **A** pertains to a member of the elemental elasticity tensor $[\mathbb{C}^e]_n$, determined from the derivative of master elemental shape functions and the measured displacements [Eqs. (3.7) and (3.9)]. Thus, geometric symmetries in conjunction with the symmetry of the measured displacement field may yield an A matrix with similar columns, leading to a high condition num- ber. This problem is offset in the present analysis by using 64-node elements resulting in extra equations, i.e., the number of equations exceeds the number of unknowns. Hence, there is no guarantee that matrix A is invertible. In fact, it will not be invertible if the material exhibits some incipient instability condition. Though such unstable cases are relevant, such conditions are not encountered in a wide range of problems. Hence, if **A** is not invertible, it may be inferred that the body demonstrates an instability or a bifurcation point.

Even the use of 64-node elements does not guarantee a well-behaved **A** matrix [Eq. (3.12)], be-

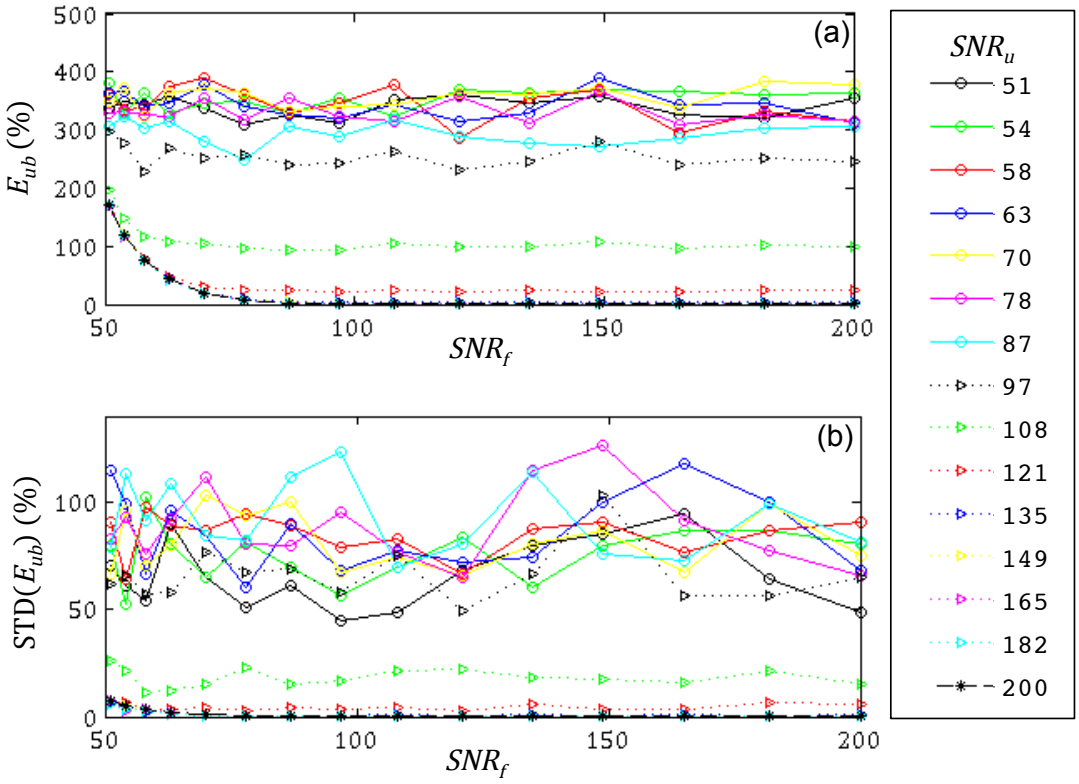

Figure 3.12: **a** Average and **b** standard deviation of maximum element error norm E_{ub} of the elements used to discretize the specimen of example 5 versus signal-to-noise ratio SNR_u and SNR_f for 15 repetitions of 225 displacement and force full-fields

cause noise in the measured displacement field could potentially increase the condition number of A. In addition, noise in the measured force field may yield erroneous results for the system of equations [Eq. (3.12)] when **A** is ill-conditioned. Therefore, it is important to examine the predicted solutions of such system. The upper-bound error norm Eub [Eq. (3.14) provides a computationally inexpensive means of evaluating the overall error level in the predicted components of the elemental material elasticity tensors, and the applicability of E_{ub} to the RULFEM is demonstrated by three examples (Sect. Validation of RULFEM for noisy input data). In addition, Table 3.3 and comparison of Figs. 3.9, 3.12, and 3.15 with Figs. 3.8, 3.11, and 3.14, respectively, confirm that $E_{ac} < E_{ub}$ for all data. This provides further validation of the error assessment criterion given by Eq. (3.14). Hence, Eq. (3.14) not only predicts an upper-bound error, but also an acceptable pair of SNR_u and SNR_f measurements.

The component-wise condition number β_i [Eq. (3.15)] provides another useful error assessment tool for RULFEM. Chandrasekaran and Ipsen [6] used β_i to distinguish the columns of **A** that are similar to each other, in a quantifiable manner similar to that of the condition number of $cond(A)$.

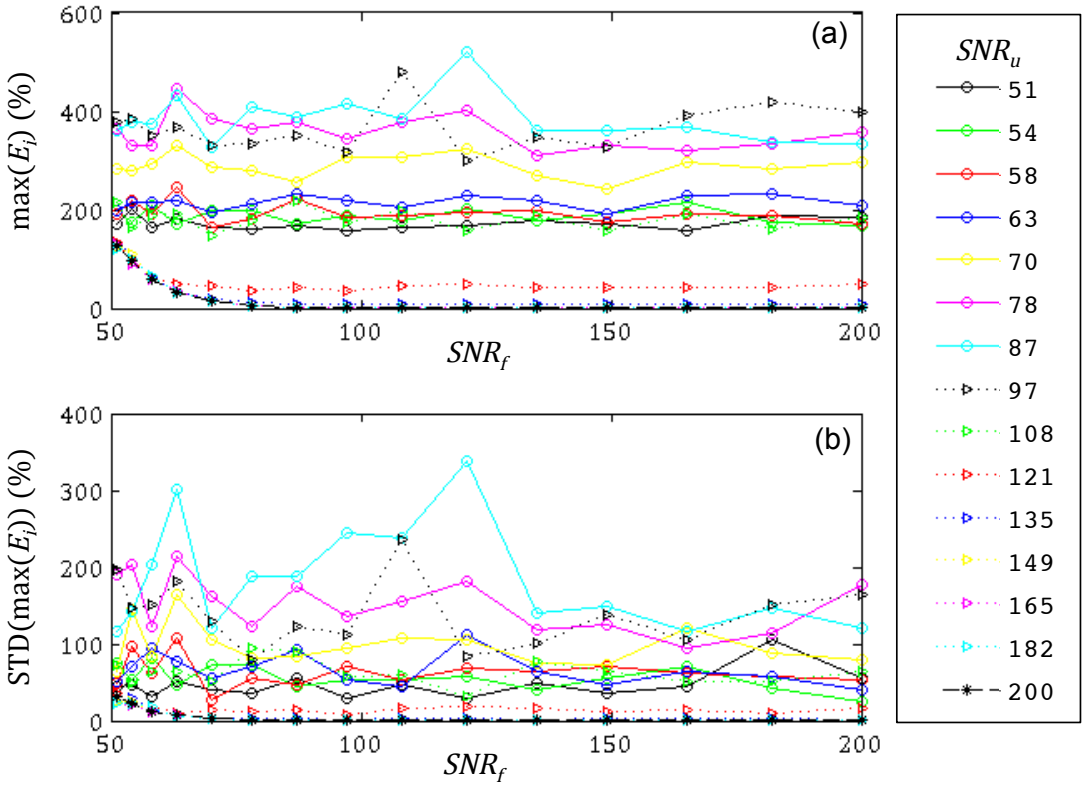

Figure 3.13: **a** Average and **b** standard deviation of maximum element error norm E_i of the elements used to discretize the specimen of example 6 versus signal-to-noise ratio SNR_u and SNR_f for 15 repetitions of 225 displacement and force full-fields

The β_i values of example 6 (previous section) are less than the overall condition number of $\mathbf{A}$ (Figs. 3.16, 3.17), although they do not necessarily correspond to the actual local errors in the elements of $\mathbf{C}$. Thus, β_i can be used in RULFEM to determine which components of $\mathbb{C}$ are less accurate than other components. This is useful information because it facilitates the selection of body perturbations above the noise level and, importantly, these perturbations can be measured in a particular direction at the node that most strongly influences the erroneous component of $\mathbb{C}$.

Many engineering problems can be modeled using 1D or 2D FEM models. RULFEM can also be used to solve such problems. However, the significant reduction in the number of DOF with 1D and 2D elements requires certain modifications in the RULFEM formulation. This is because the present method requires at least 81 independent DOF for solution.

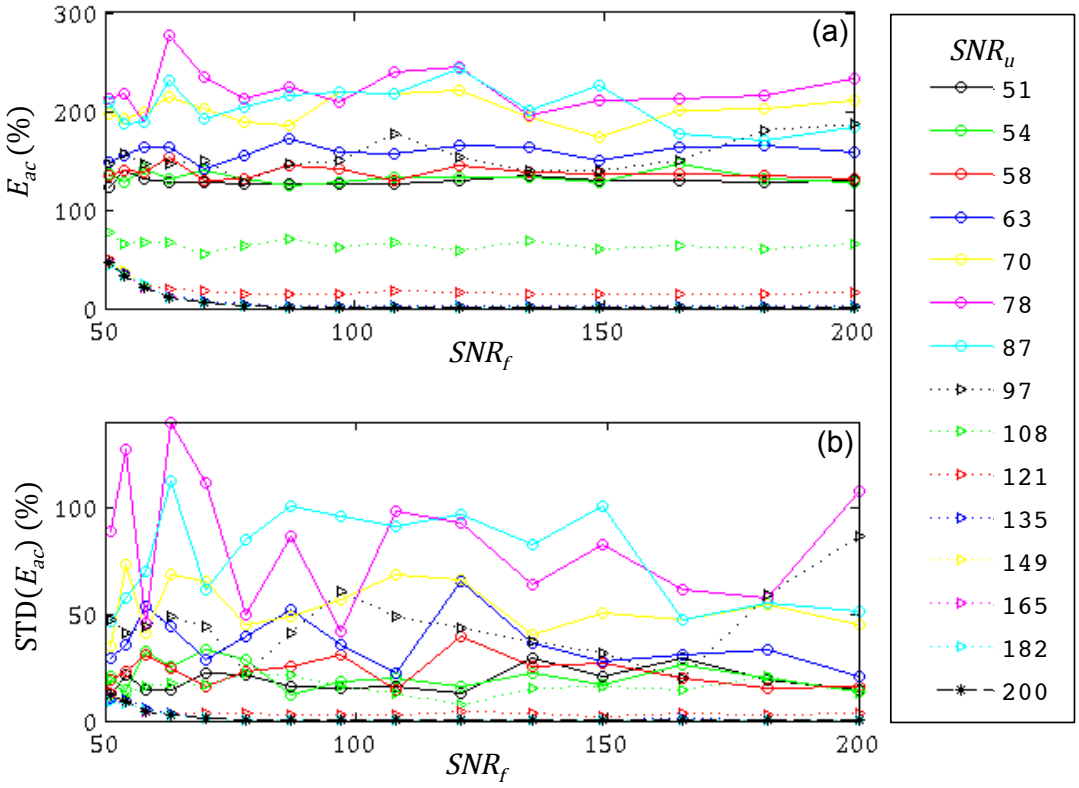

Figure 3.14: **a** Average and **b** standard deviation of maximum element error norm E_{ac} of the elements used to discretize the specimen of example 6 versus signal-to-noise ratio SNR_u and SNR_f for 15 repetitions of 225 displacement and force full-fields

3.7 Conclusion

A reverse updated Lagrangian finite element method (RULFEM) that provides nonlinear element-wise mechanical properties of 3D solid bodies (with deformed configurations tracked by incremental linear steps) was developed in this study. The RULFEM formulation relies on the solution of a linear system of equations and yields element- wise, fourth-order elasticity tensors for small displacement (or force) perturbations. The novelty of RULFEM is that an a priori assumed material constitutive law is not required; only incremental linearity of the deforming material and material uniformity within each element used to discretize the body are presumed. The validity of the method was demonstrated by numerical examples with both noise-free and noisy inputs.

The accuracy and efficiency of RULFEM depend not only on its numerical implementation but also on the accuracy and precision of the input displacement and force measurements. Because the mesh of the deformable body is distorted in each displacement perturbation (increment), remeshing may be necessary after a small number of displacement (or load) increments. Further, the

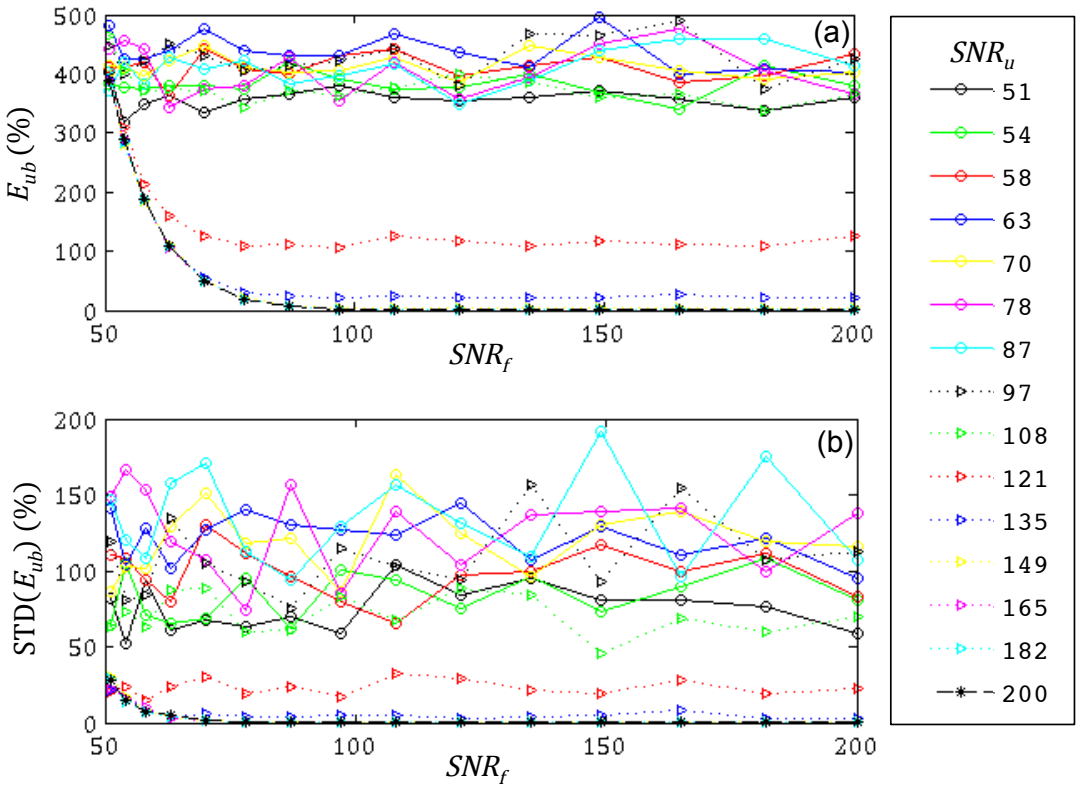

Figure 3.15: **a** Average and **b** standard deviation of maximum element error norm E_{ub} of the elements used to discretize the specimen of example 6 versus signal-to-noise ratio SNR_u and SNR_f for 15 repetitions of 225 displacement and force full-fields

accuracy of RULFEM strongly depends on the efficacy of the measuring system to closely track the nodal displacements while the body is incrementally deformed. The sensitivity of RULFEM is rooted in the high condition number of the coefficient matrix **A**. Thus, an upper bound error of the error arising from noisy measurements and, perhaps, the perturbation step size, both related to the condition number of **A**, was introduced and its utility was demonstrated by numerical examples. It was also shown that a component-wise condition number, which is comparable to the condition number of **A**, can be used to identify the components of the calculated $\mathbb{C}$ matrix that have a relatively high error and to facilitate the selection of body perturbations above the noise level, especially for a particular direction at the node that is most strongly affecting the erroneous component of $\mathbb{C}$.

Example	SNR_f	SNR_u	$maxE_i$ (%)	E_{ac} (%)	E_{ub} (%)
4	78	121	29	17	124
4	78	135	11	4	48
4	97	121	35	15	115
4	97	135	7	3	23
5	78	121	18	7	24
5	78	135	4	1	8
5	97	121	14	6	21
5	97	135	3	1	5
6	78	121	37	14	110
6	78	135	11	4	31
6	97	121	37	14	105
6	97	135	8	3	21

Table 3.3: Comparison of $maxE_i$ and corresponding E_{ac} and E_{ub} for two SNR_f and SNR_u values of examples 4-6 with noisy input vectors

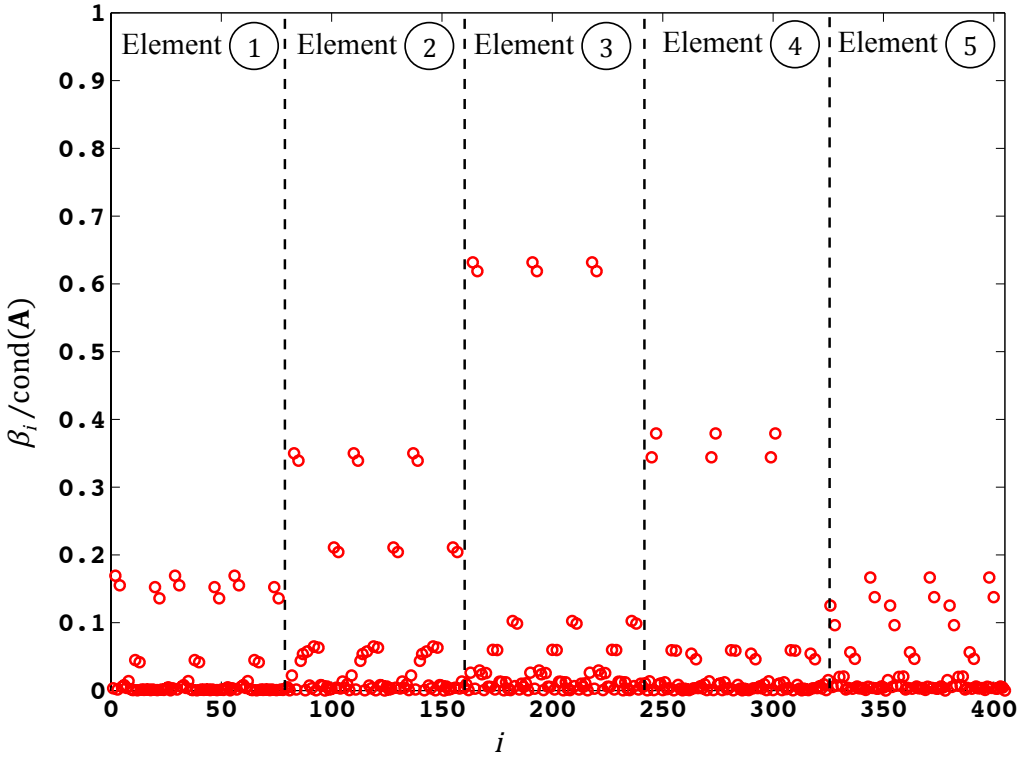

Figure 3.16: Component-wise condition number β_i normalized by $cond(A)$ of the elements used to discretize the specimen of example 6 versus ith component number of $\mathbb{C}$ vector matrix for signal-to-noise ratio $SNR_f = 85$ and $SNR_u = 137$

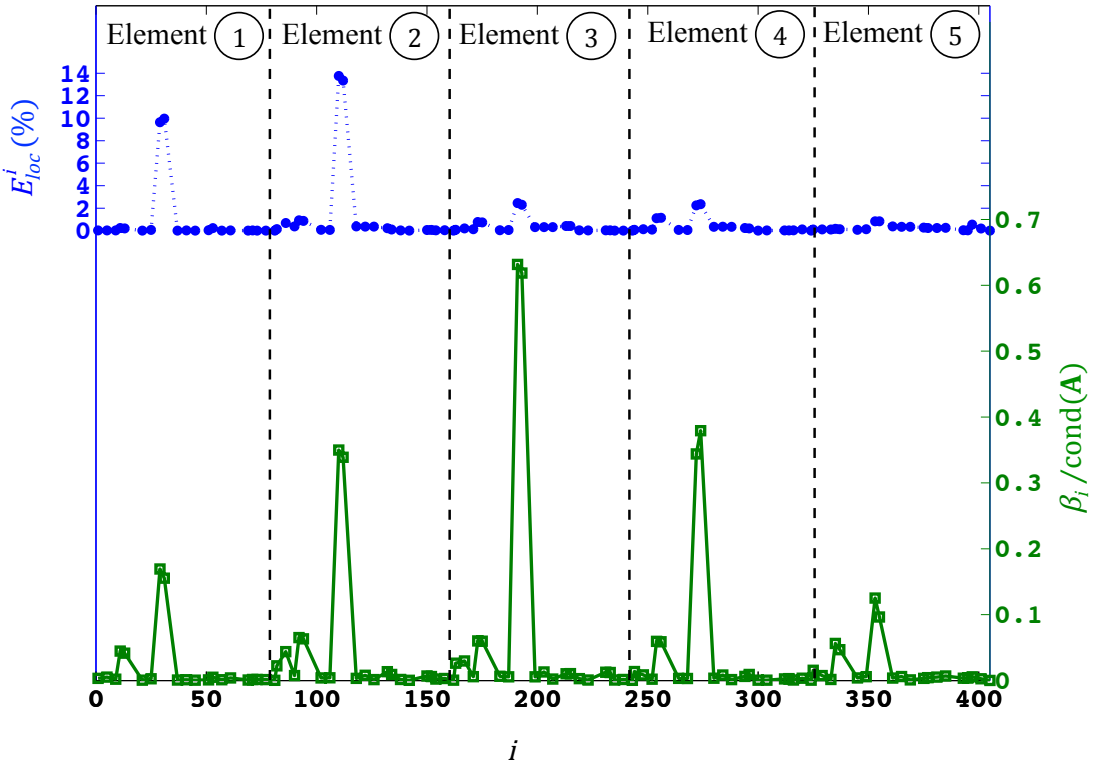

Figure 3.17: Actual local error E^i_{loc} and component-wise condition number β_i normalized by $cond(A)$ versus nonzero ith component of $\mathbb{C}_{actual}$ of the elements used to discretize the specimen of example 6 for signal-to-noise ratio $SNR_f = 85$ and $SNR_u = 137$

Chapter 4

Estimating Current State of Stress, ECSS

4.1 Introduction

The objective of the present chapter is to introduce a nondestructive inverse FEA method, termed Estimating Current State of Stress (ECSS), that is capable of predicting the current state of stress at nodal positions of the discretized body together with elemental incremental elasticity tensors. As in most exiting material identification techniques and destructive stress measurement techniques, ECSS requires three or more sets of full-field displacement and force data of the body resulting from three or more small displacement of the body relative to the current configuration. However, ECSS does not require any *a priori* constitutive assumptions beyond incremental linearity in the stress-deformation relation. Instead, it directly furnishes incremental elasticity tensors and stress fields at the finite-element level. Like the companion technique RULFEM (developed in Chapter 3) [28] on which it is based, ECSS generates a coefficient matrix defining a typically overdetermined least-square set of equations without nonlinear constraints. This coefficient matrix may have a high condition number or be rank deficient. Thus a small random error in the nodal displacement or nodal force vectors may yield erroneous results. Displacement measurements are acquired with imagining techniques, and so small measurement errors are inevitable. Global and local error assessments for these data have been introduced and validated in the course of the development of RULFEM (developed in Chapter 3) [28]; thus this issue is not discussed in this chapter. The ECSS method is developed for two types of perturbation in the following theory section. Using forward FEA, a straight steel beam is deformed in to the plastic range to generate residual stress under two different loading conditions, thus generating two different residual stress fields. The ECSS method is then validated by using surrogate full-field displacement and force measurements obtained from an FEA analysis of the residually stressed beam

4.2 Theory of Estimating Current State of Stress Method, ECSS

As in RULFEM [28] (see Chapter 3), ECSS is based on the updated Lagrangian finite element method (ULFEM), presented in Chapter 2.3. The goal of ULFEM is to compute finite element nodal displacements, $\{\mathbf{u}_h\}_1^0$, and nodal forces, $\{\mathbf{f}_h\}_1^0$ of the body Ω at configuration R_1 with respect to reference configuration R_0 (discretized by N_n nodes and N_e elements) when it is undergone a known perturbations at its boundaries, namely a known displacement at Γ_{u1} and a known traction at Γ_{q1}, Fig. 2.1; while the material incremental tensors, $\mathbb{L}_0^e$, for element e and initial nodal state of stress tensors, $\mathring{\mathbf{T}}_n$, are known throughout the body. Hence, solving Eq. (2.45) implicitly is possible, if and only if the displacement vector $\{\mathbf{u}_h\}_1^0$ can be decoupled and a set of linear equation is obtained with proper rank and condition number of the coefficient matrix, which is known as the stiffness matrix. The decoupling process is possible when the linear first Piola-Kirchhoff stress and displacement gradient relationship is applicable, i.e. Eq. (2.8) with either $\mathring{\mathbf{T}} = \mathbf{0}$ or known $\mathring{\mathbf{T}}$ at each node defining the finite element mesh. The number of equations or size of the decoupled stiffness matrix becomes equal to number of unknowns, i.e. total number of degrees of freedom, $3N_n$, excluding the boundary nodes where displacements are known.

The goal of the inverse problem, however, is to find the components of the initial state of stress, i.e. the nodal Cauchy stress tensors, $\mathring{\mathbf{T}}_n$, and the incremental elasticity tensors, $\mathbb{L}_0^e$ of each element e, where the nodal displacement field $\{\mathbf{u}_h\}_1^0$ and nodal forces $\{\mathbf{f}_h\}_1^0$ are known through measurements at configuration R_0 of the body. Because the unknown nodal Cauchy stress is a symmetric matrix, there are six unknowns per each nodal stress tensors, $\mathring{\mathbf{T}}_n$. The size of the vector form of all the nodal Cauchy stress tensors $\left\{\mathring{\mathbf{T}}\right\}$ is $(6N_n \times 1)$. The other unknown is the elemental incremental elasticity tensor, $\mathbb{L}_0^e$, which exhibits minor symmetries [19]; and, therefore, has a total of 36 unknowns per element. The size of the vector form of all the elemental incremental elasticity tensors $\{\mathbb{L}_0\}$ is $(36N_e \times 1)$. The total number of unknowns in the inverse problems becomes $(6N_n + 36N_e)$, which is more than two times larger than the total number of equations provided by the weak form of the momentum balance Eq. (2.45). Thus, the minimum number of independent perturbations are required to obtain minimum number of independent equations is three; provided the body Ω at configuration R_0 is discretized with 64-node hexagonal elements. Each known perturbation provides a pair of displacement $\{\mathbf{u}_h\}_{n+1}^n$ and force $\{\mathbf{f}_h\}_{n+1}^n$ full field data. Ultimately, the total unknown vectors are $\left\{\mathring{\mathbf{T}}, \mathbb{L}_0\right\}^T$.

The general form of the first incremental first Piola–Kirchhoff stress [Eq. (2.13)] can be introduced into Eq. (2.45), provided the incremental steps are sufficiently small for Eq. (2.45) to furnish a meaningful approximation. The elemental shape function, $[\boldsymbol{\phi}^e]$, and differential operator, $[\mathbf{B}^e]$ can be used to relate the Cauchy stress tensor, $\mathring{\mathbf{T}}$ and the deformation gradient, $\mathbf{H}_1^0$, at any point within an element e with the nodal Cauchy stresses $\left\{\mathring{\mathbf{T}}_n^e\right\}$ and the deformation gradient $\mathbf{H}_1^0 = [\mathbf{B}^e]\left\{\mathbf{u}_h^e\right\}_1^0$, respectively. Hence, the left-hand side of Eq. (2.45) becomes

$$\{\Pi(\mathbf{u})\}_1^0 = \underbrace{\mathcal{A}_{e=1}^{N_e}\left\{\int_{R_0}\left([\mathbf{B}^e]^T\left(\mathbf{I}+[\mathbf{B}^e]\{\mathbf{u}_h^e\}_1^0\right)[\boldsymbol{\phi}^e]\right)d\mathrm{V}_0^e\right\}}_{\mathbf{Z}\left(\{\mathbf{u}_h^e\}_1^0\right)=\mathbf{Z}_1^0}\left\{\mathring{\mathbf{T}}\right\}+ \underbrace{\mathcal{A}_{e=1}^{N_e}\left\{\int_{R_0}\left(\left[\mathbf{B}_{sym}^e\right]^T[\mathbb{L}_0^e]\left[\mathbf{B}_{sym}^e\right]\right)d\mathrm{V}_0^e\right\}}_{\mathbf{K}_0}\{\mathbf{u}_h\}_1^0 \tag{4.1}$$

where $\left\{\mathring{\mathbf{T}}\right\}$ is the vector formed from all nodal Cauchy stress components with size $(6N_n \times 1)$, and $\{\mathbf{u}_h\}_1^0$ is the vector of the nodal displacement components with size of $(3N_n) \times 1$. $\left[\mathbf{B}_{sym}^e\right]$ is the symmetric format of the differential operator $[\mathbf{B}^e]$, with size of $6\,(\times 3N_n)$, used directly to compute $\left[\mathbf{E}_1^0\right]$ instead of computing $\mathbf{H}_1^0$ and its transpose. $\left[\mathbb{L}_0^e\right]$ is a 6×6 representing the incremental elasticity tensor of element e e. The unknowns of the present inverse problem (ECSS), i.e., the nodal Cauchy stress elements, $\left\{\mathring{\mathbf{T}}\right\}$ and the elemental incremental elasticity tensor, $\left[\mathbb{L}_0^e\right]$, can be coupled (utilizing the authors' earlier work [28] (Chapter 3 equations (3.9)), as $\mathbf{K}_0\left\{\mathbf{u}_h^e\right\}_1^0 = \mathbf{A}_1^0\left(\left\{\mathbf{u}_h^e\right\}_1^0\right)\{\mathbb{L}_0\}$) and moved outside the second assembly integral in Eq. (4.1), as a vector of $\{\mathbb{L}_0\}$. Hence, Eq. (4.1) assumes the following short form:

$$\{\Pi(\mathbf{u})\}_1^0 = \mathbf{Z}_1^0\left\{\mathring{\mathbf{T}}\right\} + \mathbf{A}_1^0\{\mathbb{L}_0\} \tag{4.2}$$

Similar to the left-hand side of (2.45), application of the general form of the first incremental first Piola–Kirchhoff stress [Eq. (2.13)] to the second term of the right-hand side of (2.45) and uncoupling the Cauchy stress as a vector of $\left\{\mathring{\mathbf{T}}\right\}$ yields:

$$\mathcal{A}_{e=1}^{N_e}\left\{\int_{\Gamma_{q0}^e}\left([\boldsymbol{\phi}^e]^T\left\{\widehat{\mathbf{P}}^e\left(\mathbf{H}^e|_1^0\right)\mathbf{N}_0^0\right\}\right)d\mathrm{A}_0^e\right\} = \underbrace{\mathcal{A}_{e=1}^{N_e}\left\{\int_{\Gamma_{q0}^e}\left([\boldsymbol{\phi}^e]^T\left(\mathbf{I}+[\mathbf{B}^e]\{\mathbf{u}_h^e\}_1^0\right)\Psi_0\left(\mathbf{N}_0^0\right)\right)d\mathrm{A}_0^e\right\}}_{\mathbf{Y}\left(\{\mathbf{u}_h^e\}_1^0,\mathbf{N}_0^0\right)=\mathbf{Y}_1^0}\left\{\mathring{\mathbf{T}}\right\} + \underbrace{\mathcal{A}_{e=1}^{N_e}\left\{\int_{\Gamma_{q0}^e}\left([\boldsymbol{\phi}^e]^T\,\bar{\mathbf{s}}\right)d\mathrm{A}_0^e\right\}}_{\{\mathbf{f}_h^{ext}\}_1^0} \tag{4.3}$$

where $\Psi_0\left(\mathbf{N}_0^0\right)$ is a function that reorders $[\boldsymbol{\phi}_T^e]\left\{\mathring{\mathbf{T}}^{\mathbf{e}}\right\}\mathbf{N}_0^0$, such that $\Psi_0\left(\mathbf{N}_0^0\right)\left\{\mathring{\mathbf{T}}^{\mathbf{e}}\right\} = [\boldsymbol{\phi}^e]_T\left\{\mathring{\mathbf{T}}^{\mathbf{e}}\right\}\mathbf{N}_0^0$, and $\bar{\mathbf{s}}$ is a second Piola-Kirchhoff traction born from $\mathbb{L}_0\left[\mathbf{E}_1^0\right]$. As a result, Eq. (2.46) can be rewritten based on Eqs. (4.2) and (4.3) as

$$\left[\mathbf{Z}_1^0 - \mathbf{Y}_1^0\right]\left\{\mathring{\mathbf{T}}\right\} + \mathbf{A}_1^0\{\mathbb{L}_0\} = \{\mathbf{f}_h^{ext}\}_1^0 + \left\{\mathbf{f}_h^b\right\}_1^0 \tag{4.4}$$

or in matrix form

$$\underbrace{\left[\mathbf{Z}_1^0 - \mathbf{Y}_1^0 \quad \mathbf{A}_1^0\right]}_{3N_n\times(6N_n+36N_e)} \underbrace{\left\{\begin{matrix}\overset{\circ}{\mathbf{T}} \\ \mathbb{L}_0\end{matrix}\right\}}_{(6N_n+36N_e)\times 1} = \underbrace{\{\mathbf{f}_h^{ext}\}_1^0 + \left\{\mathbf{f}_h^b\right\}_1^0}_{3N_n\times 1} \tag{4.5}$$

Depending on the number of elements, N_e, three or four sets of perturbations are necessary to generate a set of equations equal to or greater than the number of unknowns. The required sets of displacement and force full-field data can be obtained by the consecutive perturbation method (CPM) and the reference configuration perturbation method (RCPM). The CPM defines each small perturbation with respect to the current configuration, i.e., it entails a perturbation of the body Ω first from configuration R_0 to R_1, then from configuration R_1 to configuration R_2, and so on, (see Fig. 4.1) . The RCPM perturbs the body Ω with respect to the original configuration R_0 as many times as required to configurations R_1, R_2, etc., while every perturbation step is independent of the the others and enough time is given to the body to obtain original configuration R_0 after each perturbations (see Fig. 4.2). Each method has its advantage and disadvantageous. In the CPM, full field displacement and force data require one time instrumentation setup (to measure the full field data); whereas in the RCPM different instrumentation setups may be needed for each perturbation step. Although the instrumentation setup may be less involved in the CPM compared to the RCPM, the associated measured field data are probably less reliable. Since the perturbation direction is biased on the CPM, the response should be on the order of measurement noise level. Consequently, each method requires slightly different numerical treatment, as explained in the following two subsections.

4.3 The ECSS Method Based on the Consecutive Perturbation Method, ECSS-CPI

The first linear perturbation yields the first set of equations Eqs. (4.4) and (4.5). The second set of equations are then produced by perturbing Ω from configuration R_1 to configuration R_2 with measured full field displacement and force fields $\{\mathbf{u}_h\}_2^1$ and $\left\{\mathbf{f}_h^{ext}\right\}_2^1$, respectively. Similar to the derivation of the first set of equations (Eqs. (4.4) or (4.5)), the second step is obtained by making use of Eq. (2.21) in Eq. (2.48).

Substituting the first Piola-Kirchhoff stress on the left-hand side of Eq. (2.48) with Eq. (2.21) and $dV_{n+1} = J_{n+1}^n dV_n$ gives

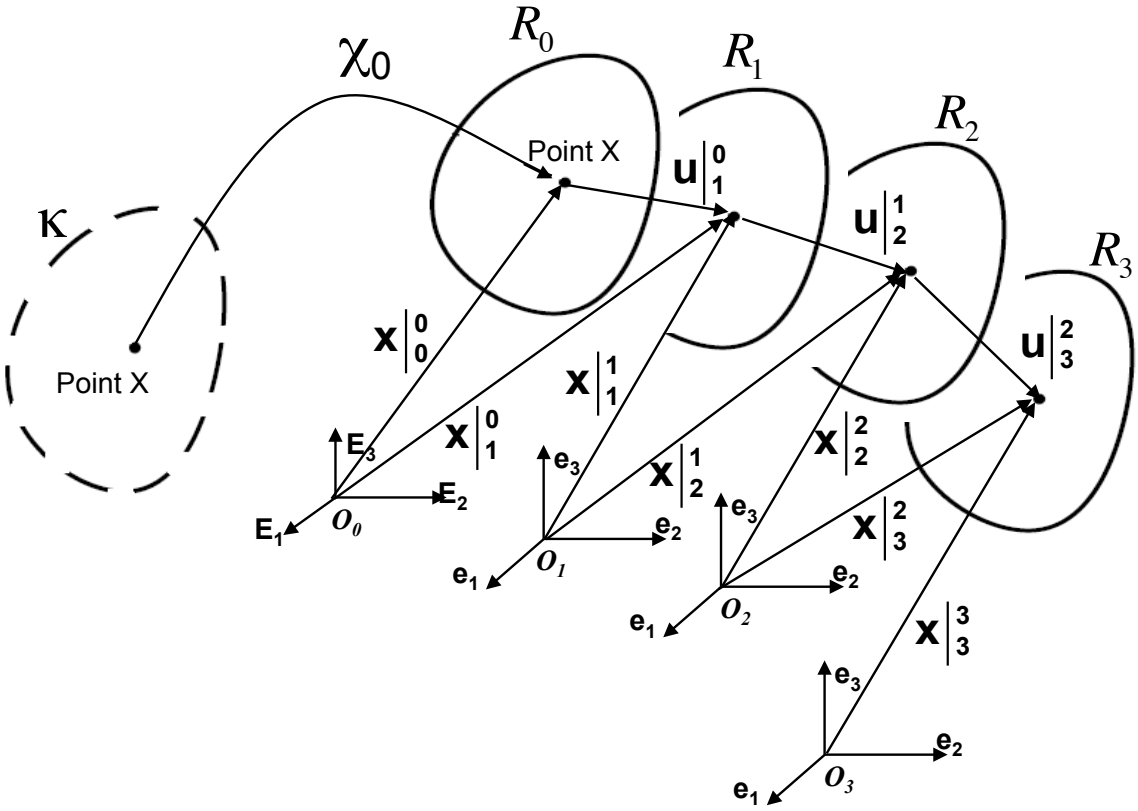

Figure 4.1: Consecutive Perturbation Inputs, ECSS-CPI, concept

$$\{\Pi(\mathbf{u})\}_2^1 = \underbrace{\mathcal{A}_{e=1}^{N_e}\left\{\int_{R_0}\left([\mathbf{B}^e]^T\left(\mathbf{I}+[\mathbf{B}^e]\{\mathbf{u}_h^e\}_2^0\right)\left([\boldsymbol{\phi}^e]\left\{\mathring{\mathbf{T}}^e\right\}\right)\left(\mathbf{I}+[\mathbf{B}^e]\{\mathbf{u}_h^e\}_1^0\right)\right)d\mathrm{V}_0^e\right\}}_{\mathbf{K}_1} +$$
$$\underbrace{\mathcal{A}_{e=1}^{N_e}\left\{\int_{R_0}\left([\mathbf{B}^e]^T\left(\mathbf{I}+[\mathbf{B}^e]\{\mathbf{u}_h^e\}_2^1\right)\left([\mathbb{L}_0^e]\left[\mathbf{B}_{sym}^e\right]^T\{\mathbf{u}_h^e\}_1^0\right)\left(\mathbf{I}+[\mathbf{B}^e]\{\mathbf{u}_h^e\}_1^0\right)^T\right)d\mathrm{V}_0^e\right\}}_{\mathbf{K}_2} + \tag{4.6}$$
$$\underbrace{\mathcal{A}_{e=1}^{N_e}\left\{\int_{R_1}\left([\mathbf{B}^e]^T\left([\mathbb{L}_1^e]\left[\mathbf{B}_{sym}^e\right]^T\{\mathbf{u}_h^e\}_2^1\right)\right)d\mathrm{V}_1^e\right\}}_{\mathbf{K}_3}$$

where $[\mathbf{B}^e]$ is the differential operator of the element shape function with respect to R_i configuration, and the terms including the incremental elasticity tensors, such as $\left(\left[\mathbb{L}_0^e\right]\left[\mathbf{B}_{sym}^e\right]^T\left\{\mathbf{u}_h^e\right\}_1^0\right)$, have technically 6 rows and as many as 3 times number of nodes per element. However, the full version with 9 rows is required to match the size of terms to the surrounding terms. The conversion of the 6-element symmetric tensor to a general 9-element tensor is not discussed here for brevity.

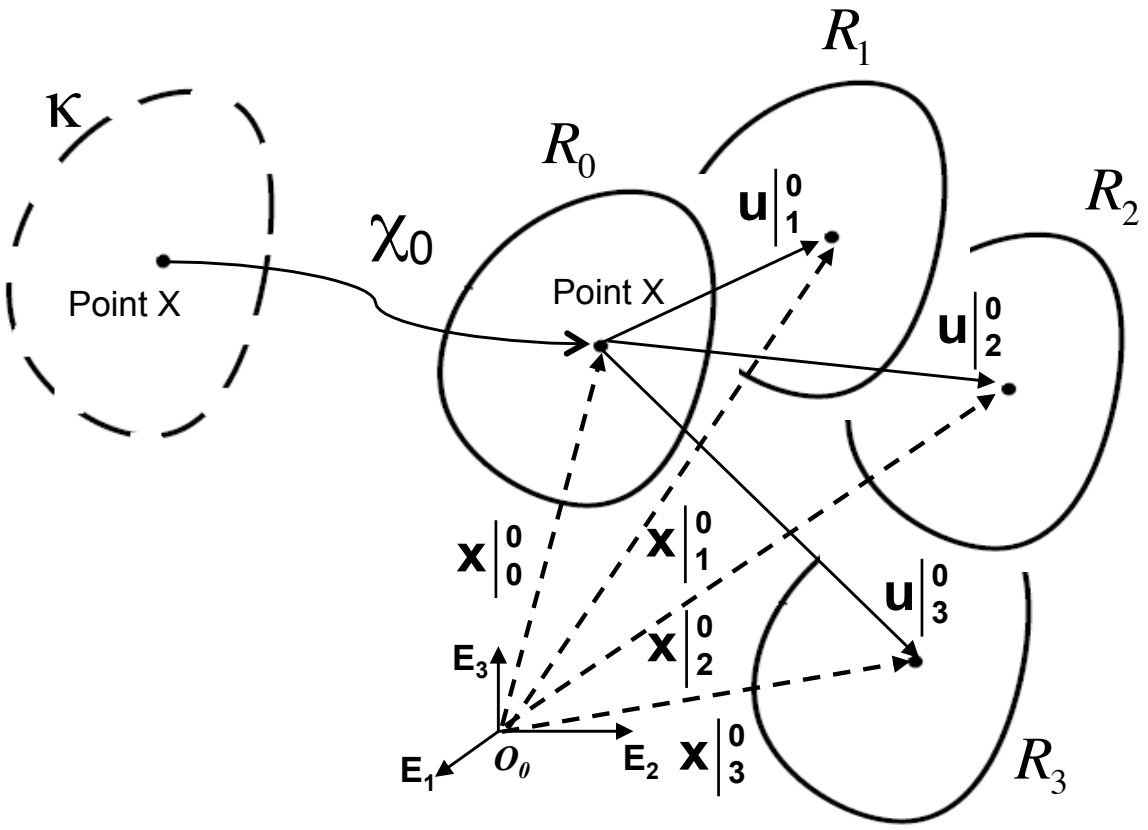

Figure 4.2: Reference Configuration Perturbations, ECSS-RCP, Concept.

In the inverse problem, the unknowns are the initial state of stress tensors for all element e nodes, $[\boldsymbol{\phi}^e]\left\{\mathring{\mathbf{T}}^e\right\}$, the incremental elasticity tensors of all elements in the first perturbation, $\left[\mathbb{L}_0^e\right]$, and the incremental elasticity tensors of all elements at the second perturbation, $\left[\mathbb{L}_1^e\right]$, where they are referred to in vector format, for the entire mesh with, $\left\{\mathring{\mathbf{T}}\right\}$, $\{\mathbb{L}_0\}$ and $\{\mathbb{L}_1\}$, respectively. To decouple these three unknown vectors in (4.6) the terms of K_1, K_2, and K_3, the following treatment is used:

$$\sum_{i=1}^{6Nn} \frac{\partial \mathbf{K}_1}{\partial \left\{\mathring{\mathbf{T}}^e\right\}_i} = \left[\mathbf{Z}_2^1\right]\left\{\mathring{\mathbf{T}}\right\} \tag{4.7}$$

where i is the i-th term of the initial stress tensor of element e in the form of vector $\left\{\mathring{\mathbf{T}}^e\right\}$; each differential $\dfrac{\partial \mathbf{K}_1}{\partial \left\{\mathring{\mathbf{T}}^e\right\}_i}$ creates a column of matrix $\left[\mathbf{Z}_2^1\right]$. Similarly, the second and third terms are defined as

$$\sum_{i=1}^{36Ne} \frac{\partial \mathbf{K}_2}{\partial \left[\mathbb{L}_0^e\right]_i} = \left[\mathbf{A}_2^0\right]\{\mathbb{L}_0\} \tag{4.8}$$

where i is the i-th term of element e in form of $\left[\mathbb{L}_0^e\right]$, and each differential $\dfrac{\partial \mathbf{K}_2}{\partial \left[\mathbb{L}_0^e\right]_i}$ creates a column of matrix $\left[\mathbf{A}_2^0\right]$.

$$\sum_{i=1}^{36Ne} \frac{\partial \mathbf{K}_3}{\partial \left[\mathbb{L}_1^e\right]_i} = \left[\mathbf{A}_2^1\right]\{\mathbb{L}_1\} \tag{4.9}$$

where i is the i-th term of element e in form of $\left[\mathbb{L}_1^e\right]$, and each differential $\dfrac{\partial \mathbf{K}_3}{\partial \left[\mathbb{L}_1^e\right]_i}$ yields a column of matrix $\left[\mathbf{A}_2^1\right]$.

Eq. (4.6) can be rewritten based on the defined decoupled matrices and vectors of unknowns as defined in Eqs. (4.7), (4.8), and (4.9). Thus,

$$\{\Pi(\mathbf{u})\}_2^1 = \left[\mathbf{Z}_2^1\right]\left\{\mathring{\mathbf{T}}\right\} + \left[\mathbf{A}_2^0\right]\{\mathbb{L}_0\} + \left[\mathbf{A}_2^1\right]\{\mathbb{L}_1\} \tag{4.10}$$

where $\{\mathbb{L}_1\}$ is a vector of the components of all the elements incremental elasticity tensors, which becomes another unknown vector to be computed.

Using Nanson's formula, the successive area elements and unit normal vectors in the Lagrangian formulations are related as

$$\frac{1}{J_{n+1}^n}\left(\mathbf{F}_{n+1}^n\right)^T \mathbf{N}_{n+1}^{n+1} dA_{n+1} = \mathbf{N}_n^n dA_n \tag{4.11}$$

In the second perturbation with respect to the first configuration R1, the second term of the right-hand side of Eq. (2.48) after incorporating Eq. (4.11) and the variable defined for Eq. (4.3) becomes:

$$\begin{aligned}
&\mathcal{A}_{e=1}^{N_e}\left\{\int_{\Gamma_{q_1}^e}\left([\boldsymbol{\phi}^e]^T\left\{\widehat{\mathbf{P}}^e\left(\mathbf{H}^e|_2^1\right)\mathbf{N}_1^1\right\}\right)d\mathrm{A}_1^e\right\} = \\
&\underbrace{\mathcal{A}_{e=1}^{N_e}\left\{\int_{\Gamma_{q0}^e}\left([\boldsymbol{\phi}^e]^T\left(\mathbf{I}+[\mathbf{B}^e]\{\mathbf{u}_h^e\}_2^0\right)\Psi_1\left(\mathbf{N}_0^0\right)\right)d\mathrm{A}_0^e\right\}}_{\mathbf{Y}\left(\{\mathbf{u}_h^e\}_2^0,\mathbf{N}_0^0\right)=\mathbf{Y}_2^0}\left\{\mathring{\mathbf{T}}\right\} \\
&+\underbrace{\mathcal{A}_{e=1}^{N_e}\left\{\int_{\Gamma_{q0}^e}\left([\boldsymbol{\phi}^e]^T\left(\mathbf{I}+[\mathbf{B}^e]\{\mathbf{u}_h^e\}_2^1\right)\bar{\mathbf{s}}_0\right)d\mathrm{A}_0^e\right\}}_{\{\mathbf{f}_h^{ext}\}_2^0}+\underbrace{\mathcal{A}_{e=1}^{N_e}\left\{\int_{\Gamma_{q_1}^e}\left([\boldsymbol{\phi}^e]^T\bar{\mathbf{s}}_1\right)d\mathrm{A}_1^e\right\}}_{\{\mathbf{f}_h^{ext}\}_2^1}
\end{aligned} \tag{4.12}$$

Thus, the concise matrix form of the second step Lagrangian formulation based on Eqs. (4.10) and (4.12) yields

$$\underbrace{\left[\mathbf{Z}_2^1 - \mathbf{Y}_2^0 \quad \mathbf{A}_2^0 \quad \mathbf{A}_2^1\right]}_{3N_n\times(6N_n+72N_e)} \underbrace{\begin{Bmatrix} \mathring{\mathbf{T}} \\ \mathbb{L}_0 \\ \mathbb{L}_1 \end{Bmatrix}}_{(6N_n+72N_e)\times 1} = \underbrace{\left\{\mathbf{f}_h^b\right\}_2^0 + \left\{\mathbf{f}_h^{ext}\right\}_2^0 + \left\{\mathbf{f}_h^{ext}\right\}_2^1}_{3N_n\times 1} \tag{4.13}$$

In the third step, the weak-form uses the first Piola-Kirchhoff stress, defined in Eq. (2.22), and the left-hand side of Eq. (2.48) becomes

$$\begin{aligned}
\{\Pi(\mathbf{u})\}_3^2 = & \underbrace{\mathcal{A}_{e=1}^{N_e}\left\{\int_{R_0}\left([\mathbf{B}^e]^T\left(\mathbf{I}+[\mathbf{B}^e]\{\mathbf{u}_h^e\}_3^0\right)\left([\boldsymbol{\phi}^e]\left\{\mathring{\mathbf{T}}^e\right\}\right)\left(\mathbf{I}+[\mathbf{B}^e]\{\mathbf{u}_h^e\}_2^0\right)^T\right)d\mathrm{V}_0^e\right\}}_{\mathbf{K}_4} + \\
& \underbrace{\mathcal{A}_{e=1}^{N_e}\left\{\int_{R_0}\left([\mathbf{B}^e]^T\left(\mathbf{I}+[\mathbf{B}^e]\{\mathbf{u}_h^e\}_3^1\right)\left([\mathbb{L}_0^e]\left[\mathbf{B}_{sym}^e\right]^T\{\mathbf{u}_h^e\}_1^0\right)\left(\mathbf{I}+[\mathbf{B}^e]\{\mathbf{u}_h^e\}_2^0\right)^T\right)d\mathrm{V}_0^e\right\}}_{\mathbf{K}_5} + \\
& \underbrace{\mathcal{A}_{e=1}^{N_e}\left\{\int_{R_1}\left([\mathbf{B}^e]^T\left(\mathbf{I}+[\mathbf{B}^e]\{\mathbf{u}_h^e\}_3^2\right)\left([\mathbb{L}_1^e]\left[\mathbf{B}_{sym}^e\right]^T\{\mathbf{u}_h^e\}_2^1\right)\left(\mathbf{I}+[\mathbf{B}^e]\{\mathbf{u}_h^e\}_2^0\ 1\right)^T\right)d\mathrm{V}_1^e\right\}}_{\mathbf{K}_6} + \\
& \underbrace{\mathcal{A}_{e=1}^{N_e}\left\{\int_{R_2}\left([\mathbf{B}^e]^T\left([\mathbb{L}_2^e]\left[\mathbf{B}_{sym}^e\right]^T\{\mathbf{u}_h^e\}_3^2\right)\right)d\mathrm{V}_2^e\right\}}_{\mathbf{K}_7}
\end{aligned} \tag{4.14}$$

Exploiting the decoupling technique applied to Eqs. (4.7) through (4.9), the four derived terms of $\mathbf{K}_4$ to $\mathbf{K}_7$ shown on the right-hand side of Eq. (4.14) combine as

$$\{\Pi(\mathbf{u})\}_3^2 = \left[\mathbf{Z}_3^2\right]\left\{\mathring{\mathbf{T}}\right\} + \left[\mathbf{A}_3^0\right]\{\mathbb{L}_0\} + \left[\mathbf{A}_3^1\right]\{\mathbb{L}_1\} + \left[\mathbf{A}_3^2\right]\{\mathbb{L}_2\} \tag{4.15}$$

where the left-hand side of Eq. (2.48) for the third step is expanded as following:

$$\begin{aligned}
& \mathcal{A}_{e=1}^{N_e}\left\{\int_{\Gamma_{q2}^e}\left([\boldsymbol{\phi}^e]^T\left\{\widehat{\mathbf{P}}^e\left(\mathbf{H}^e|_3^2\right)\mathbf{N}_2^2\right\}\right)d\mathrm{A}_2^e\right\} = \\
& \underbrace{\mathcal{A}_{e=1}^{N_e}\left\{\int_{\Gamma_{q0}^e}\left([\boldsymbol{\phi}^e]^T\left(\mathbf{I}+[\mathbf{B}^e]\{\mathbf{u}_h^e\}_3^0\right)\Psi_2\left(\mathbf{N}_0^0\right)\right)d\mathrm{A}_0^e\right\}}_{\mathbf{Y}\left(\{\mathbf{u}_h^e\}_3^0,\mathbf{N}_0^0\right)=\mathbf{Y}_3^0}\left\{\mathring{\mathbf{T}}\right\} + \underbrace{\mathcal{A}_{e=1}^{N_e}\left\{\int_{\Gamma_{q0}^e}\left([\boldsymbol{\phi}^e]^T\left(\mathbf{I}+[\mathbf{B}^e]\{\mathbf{u}_h^e\}_3^1\right)\bar{\mathbf{s}}_0\right)d\mathrm{A}_0^e\right\}}_{\{\mathbf{f}_h^{ext}\}_3^1} \\
& + \underbrace{\mathcal{A}_{e=1}^{N_e}\left\{\int_{\Gamma_{q1}^e}\left([\boldsymbol{\phi}^e]^T\left(\mathbf{I}+[\mathbf{B}^e]\{\mathbf{u}_h^e\}_3^2\right)\bar{\mathbf{s}}_1\right)d\mathrm{A}_1^e\right\}}_{\{\mathbf{f}_h^{ext}\}_3^2} + \underbrace{\mathcal{A}_{e=1}^{N_e}\left\{\int_{\Gamma_{q2}^e}\left([\boldsymbol{\phi}^e]^T\bar{\mathbf{s}}_2\right)d\mathrm{A}_2^e\right\}}_{\{\mathbf{f}_h^{ext}\}_3^2}
\end{aligned} \tag{4.16}$$

Thus, as in the previous step, the concise matrix form of the third step Lagrangian formulation based on Eqs. (4.15) and (4.16) becomes:

$$\underbrace{\begin{bmatrix}\mathbf{Z}_3^2-\mathbf{Y}_3^0 & \mathbf{A}_3^0 & \mathbf{A}_3^1 & \mathbf{A}_3^2\end{bmatrix}}_{3N_n\times(6N_n+108N_e)}\underbrace{\begin{Bmatrix}\mathring{\mathbf{T}}\\ \mathbb{L}_0\\ \mathbb{L}_1\\ \mathbb{L}_2\end{Bmatrix}}_{(6N_n+108N_e)\times 1}=\underbrace{\left\{\mathbf{f}_h^b\right\}_3^0+\{\mathbf{f}_h^{ext}\}_3^0+\{\mathbf{f}_h^{ext}\}_3^1+\{\mathbf{f}_h^{ext}\}_3^2}_{3N_n\times 1} \tag{4.17}$$

A full set of equations can be obtained from Eq. (4.5), Eq. (4.13), and Eq. (4.17) . This form furnishes a least-squares problem, which can be solved for the nodal Cauchy stress and three steps of incremental elasticity tensors of all finite elements defining the body, i.e.,

$$\underbrace{\begin{bmatrix}\mathbf{Z}_1^0-\mathbf{Y}_1^0 & \mathbf{A}_1^0 & \mathbf{0} & \mathbf{0}\\ \mathbf{Z}_2^1-\mathbf{Y}_2^0 & \mathbf{A}_2^0 & \mathbf{A}_2^1 & \mathbf{0}\\ \mathbf{Z}_3^2-\mathbf{Y}_3^0 & \mathbf{A}_3^0 & \mathbf{A}_3^1 & \mathbf{A}_3^2\end{bmatrix}_{9N_n\times(6N_n+108N_e)}}_{\mathcal{G}_1}\underbrace{\begin{Bmatrix}\mathring{\mathbf{T}}\\ \mathbb{L}_0\\ \mathbb{L}_1\\ \mathbb{L}_2\end{Bmatrix}_{(6N_n+108N_e)\times 1}}_{\mathcal{X}_1}=\underbrace{\begin{Bmatrix}\left\{\mathbf{f}_h^b\right\}_1^0+\left\{\mathbf{f}_h^{ext}\right\}_1^0\\ \left\{\mathbf{f}_h^b\right\}_2^0+\left\{\mathbf{f}_h^{ext}\right\}_2^0+\left\{\mathbf{f}_h^{ext}\right\}_2^1\\ \left\{\mathbf{f}_h^b\right\}_3^0+\left\{\mathbf{f}_h^{ext}\right\}_3^0+\left\{\mathbf{f}_h^{ext}\right\}_3^1+\left\{\mathbf{f}_h^{ext}\right\}_3^2\end{Bmatrix}_{9N_n\times 1}}_{\mathcal{B}_1} \tag{4.18}$$

or in short form:

$$\mathcal{G}_1\mathcal{X}_1=\mathcal{B}_1 \tag{4.19}$$

4.4 The ECSS Method Based on the Reference Configuration Perturbation Method, ECSS-RCP

In this approach, the body Ω at configuration R_0 is perturbed in an elastic fashion at least three times, and the required measurements are obtained after each perturbation. The perturbation is then removed and the body resumes its reference configuration R_0. For instance, the first configuration R_1 is obtained by applying a small perturbation to the body at configuration R_0. The associated full-field displacement vector $\{\mathbf{u}_h\}_1^0$ and full-field force vector $\{\mathbf{f}_h\}_1^0$ are then measured, and the second configuration R_2 is similarly obtained with applying another small perturbation to configuration R_0. Subsequently the associated full-field displacement vector $\{\mathbf{u}_h\}_2^0$ and full-field force vector $\{\mathbf{f}_h\}_2^0$ are measured. In the same way, the third perturbation deforms the body from the reference configuration R_0 to configuration R_3, and the full-field pair of displacement and force vectors $\{\mathbf{u}_h\}_3^0$ and $\{\mathbf{f}_h\}_3^0$,respectively, are measured.

Since the reference configuration for each perturbation is configuration R_0, the unknowns are only the nodal components of Cauchy stress and the elements of incremental elasticity tensors in vector form $\left\{\mathring{T},\mathbb{L}_0\right\}^T$. Accordingly, each perturbation step yields a set of equations, such as Eq. (4.5) that are combined to yield the following least-squares problem, which is similar to

Eq.(4.20), similar to Eq. (4.18), and can be solved to obtain the nodal Cauchy stresses and three-step incremental elasticity tensors of all finite elements comprising the body, i.e.,

$$\underbrace{\begin{bmatrix} \mathbf{Z}_1^0 - \mathbf{Y}_1^0 & \mathbf{A}_1^0 \\ \mathbf{Z}_2^1 - \mathbf{Y}_2^0 & \mathbf{A}_2^0 \\ \mathbf{Z}_3^2 - \mathbf{Y}_3^0 & \mathbf{A}_3^0 \end{bmatrix}_{9N_n \times (6N_n + 36N_e)}}_{\mathcal{G}_2} \underbrace{\begin{Bmatrix} \mathring{\mathbf{T}} \\ \mathbb{L}_0 \end{Bmatrix}_{(6N_n + 36N_e) \times 1}}_{\mathcal{X}_2} = \underbrace{\begin{Bmatrix} \left\{\mathbf{f}_h^b\right\}_1^0 + \left\{\mathbf{f}_h^{ext}\right\}_1^0 \\ \left\{\mathbf{f}_h^b\right\}_2^0 + \left\{\mathbf{f}_h^{ext}\right\}_2^0 \\ \left\{\mathbf{f}_h^b\right\}_3^0 + \left\{\mathbf{f}_h^{ext}\right\}_3^0 \end{Bmatrix}_{9N_n \times 1}}_{\mathcal{B}_2} \tag{4.20}$$

or in short form:

$$\mathcal{G}_2 \mathcal{X}_2 = \mathcal{B}_2 \tag{4.21}$$

4.5 Validation of the ECSS method

The input to ECSS method is the full-field data (i.e., displacement and traction fields) may contain noise and measurement errors. As with other inverse methods, ECSS relies on the solution of a system of equations containing a coefficient matrix $\mathcal{G}_1$ or $\mathcal{G}_2$ characterized by moderate to relatively high condition number and respective forcing vectors $\mathcal{B}_1$ or $\mathcal{B}_2$. Consequently, validation criteria and error assessment in the presence of noisy input data are necessary. Numerical techniques and criteria for this purpose were presented and validated in our previous work [28]. These techniques are capable not only to compute overall upper-bound error, but can also be used to estimate the local error of each component of the unknown vector, $\mathcal{X}_1$. Therefore no examples are presented for noisy input data in this paper.

ECSS-RCP method is validated with examples presented in the present section. The numerical tool used to solve Eq. (4.20) is the MatLab back-slash operator (version 2013b). MatLab yields a least-squares solution for the rectangular matrix $\mathcal{G}_2$ and solves so-called "over-determined systems" using QR factorization.

The solution to Eq. (4.20) yields (1) as many symmetric second-order Cauchy stress tensors, with 6 components, as the number of nodes used to discretize the body, and (2) as many fourth-order incremental elasticity tensors, with 36 components, as the number of (64-node) elements used to discretize the deformed body. Mechanical property of each element e is defined by its fourth-order incremental elasticity tensor, which is represented by a (6×6) matrix $[\mathbb{L}^e]_i$, where $i \in \{0, 1, 2, 3\}$. The mechanical properties of an element e are defined by its fourth-order incremental elasticity tensor, which is represented by a (6×6) matrix $[\mathbb{L}^e]_i$, where $i \in \{0, 1, 2, 3\}$. Since ECSS predicts local (element-wise and node-wise) properties from the solution of the global equation system [Eq. (4.20)], two levels of assessment must be used to validate the method.

The objective of local validation is to compare the predicted components of $[\mathbb{L}^e]_i$ and $\mathring{\mathbf{T}}_n$ with actual components. Although a component-wise comparison of matrices might be feasible when dealing with a few finite elements, the comparison is cumbersome when there are many elements. Therefore, it is preferred to assess the accuracy of ECSS using a single error number. Here, the

element error norm $E_{L_i}(e)$ at reference configuration i of incremental elasticity tensor $\mathbb{L}_i$ is used, which is defined as

$$E_{L_i}(e) = \frac{\left\| \left[\mathbb{L}^e_{ECSS}\right]_i - \left[\mathbb{L}^e_{FEA}\right]_i \right\|}{\left\| \left[\mathbb{L}^e_{FEA}\right]_i \right\|} \tag{4.22}$$

where $\left[\mathbb{L}^e_{ECSS}\right]_i$ and $\left[\mathbb{L}^e_{FEA}\right]_i$ are the incremental elasticity tensor of element e at reference configuration i predicted by ECSS and that of the actual, respectively, and $\|\bullet\|$ is the matrix norm. However, there may be nodes with vanishing stress components, and so a similar definition is not appropriate for stress error predictions. The norm of the differences of the actual and predicted stresses can be compared against the norm of the actual stress.

$$E_{\overset{\circ}{\mathbf{T}}}(n) = \left\| \left[\overset{\circ}{\mathbf{T}}_{ECSS}\right]_n - \left[\overset{\circ}{\mathbf{T}}_{FEA}\right]_n \right\| \; versus \; \left\| \left[\overset{\circ}{\mathbf{T}}_{FEA}\right]_n \right\| \tag{4.23}$$

where $\left[\overset{\circ}{\mathbf{T}}_{ECSS}\right]_n$ and $\left[\overset{\circ}{\mathbf{T}}_{FEA}\right]_n$, are the Cauchy stresses tensors of node n at configuration R_0 predicted by ECSS and that of the actual.

The main goal of this presentation is to develop and demonstrate ECSS for noise-free and error-free input data pairs (full field displacement and force). Accordingly, global error assessments are ignored for the presented examples. The machinery for accessing the global error of the system of equations [Eq. (4.18) or Eq. (4.20)] has been developed and demonstrated in earlier work of the authors [28]. The very same machinery are applicable to the system of equations developed here.

The capability of the present method is demonstrated in this section by two examples in which the input measurement (force and displacement) field data are not obtained from actual measurements; instead they are generated from a forward static finite element analysis of a body with known incremental elasticity tensors and prescribed traction and displacement perturbations. These fields are regarded as effectively noise-free and are used to validate the ECSS-RCP formulation. The computed unknown vector $\left\{\overset{\circ}{\mathbf{T}}, \mathbb{L}_0\right\}^T$ is then compared to the actual quantities utilizing the error equations Eq. (4.22) and Eq. (4.23). Further, some stress contour plots and figure plots of Cauchy stress components are presented.

Inspired by standardized material testing protocols, the following two examples model four-point and three-point bending experiments of a beam with a trapezoidal cross-section (see Fig. 4.3). The beams are made of a hypothetical elasto-perfectly plastic steel with Young elastic modulus of 200 GPa, Poisson ration of 0.3, yield strength of 250 MPa. Residual stress fields in the beams were produced in two steps. In Step-1 the beams were first loaded such that the beam mid-sections were plasticized, and in Step-2 the beams were unloaded completely. The stressed beams under no loading, e.g $\left(\overset{\circ}{\mathbf{b}}, \overset{\circ}{\mathbf{t}}\right) = (\mathbf{0}, \mathbf{0})$, but with non-zero residual stress field, $\overset{\circ}{\mathbf{T}} \neq \mathbf{0}$, reach the configuration R_0 in the ECSS-RCP formulation. To numerically produce configuration R_0, the two steps were modeled using the nonlinear capabilities of the commercial finite element software code ABAQUS 6.9EF (Dassault Systèmes 10 rue Marcel Dassault, 78140 Vélizy-Villacoublay – France, telephone: +33 1 61 62 61 62 – VAT: FR 52 322 306 440) . The beams were meshed using 3454 eight-node hexagonal elements (namely C3D8 in ABAQUS) and a total of 4900 nodes.

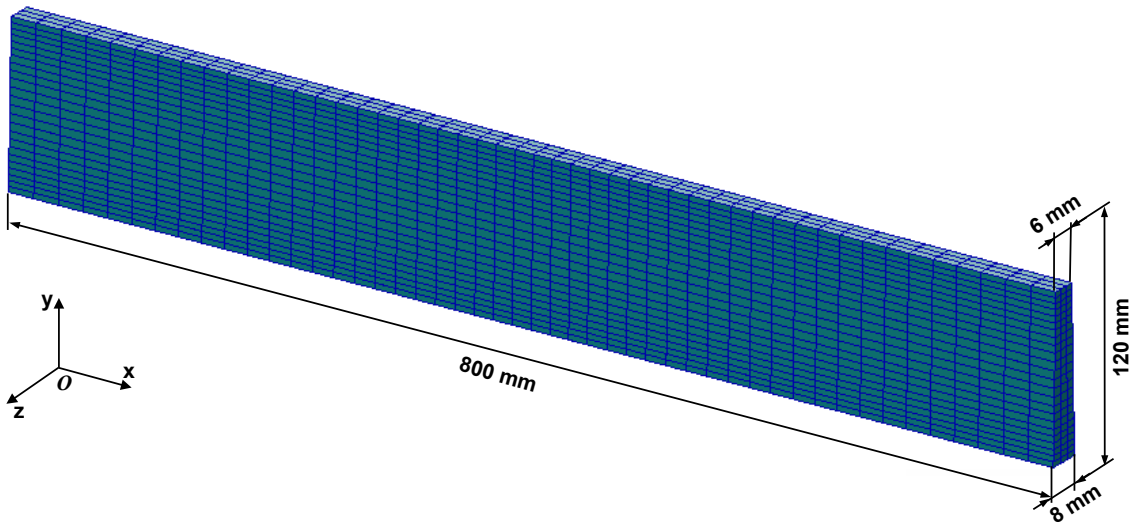

Figure 4.3: Beam example geometry and finite element mesh

For the given number of nodes and number of elements, the total number of unknowns become $3454 \times 36 + 4900 \times 6 = 153,744$; hence, at least eleven different perturbations are required to compute as many unknowns. To reduce the number of perturbations to a minimum and manageable figure, the number of elements must be reduced. However, the number of nodes must remain the same. Higher order Lagrangian elements for these examples utilizes all the nodes defined in the original mesh, but the number of elements reduces. For examples, 7, 4, and 3 perturbations are necessary for 16-node, 32-node and 64-node hexagonal iso-parametric elements, respectively. For the discussed beam examples, each 27 adjacent eight-node hexagonal elements form a 64 node element. Thus, total number of 64-node elements used in ECSS computation became $N_e = 128$ with the same total node of 8-node hexagonal mesh of $N_e = 4900$.

Example 1: The residual stress field produced by a four-point bending experiment is shown in Fig. 4.4 fThis the two step analysis explained above with ABAQUS/Standard Solver to construct the configuration R_0 of the beam with residual stress fields shown in Fig. 4.5. The beam were then perturbed, in the absence of body forces, four times from reference configuration R_0. The boundary condition of each perturbations that yielded configurations R_1, R_2, R_3, and R_4 are shown in Fig. 4.6, Fig. 4.7, Fig. 4.8, and Fig. 4.9, respectively. Four full field displacements and traction forces were then extracted from linear static finite element analysis of the four perturbations, namely: $\left(\{\mathbf{u}_h\}_1^0, \{\mathbf{f}_h\}_1^0\right)$ from configuration R_1, $\left(\{\mathbf{u}_h\}_2^0, \{\mathbf{f}_h\}_2^0\right)$ from configuration R_2, $\left(\{\mathbf{u}_h\}_3^0, \{\mathbf{f}_h\}_3^0\right)$ from configuration R_3, and $\left(\{\mathbf{u}_h\}_4^0, \{\mathbf{f}_h\}_4^0\right)$ from configuration R_4. The total number of nodes defining the finite element mesh of the beam yielded the total number of degrees-of-freedom (DOF) to be $DOF = 3N_n = 14700$. The total number of unknowns is $6N_n + 36Ne = 34008$. Thus, the required ECSS-RCP system of equations, defined for three perturbations by Eq. (4.20), yields a coefficient matrix $\mathcal{G}_2$ of size 44100×34008 and a forcing vector of $\mathcal{B}_2$ of size 44100×1. Thus,

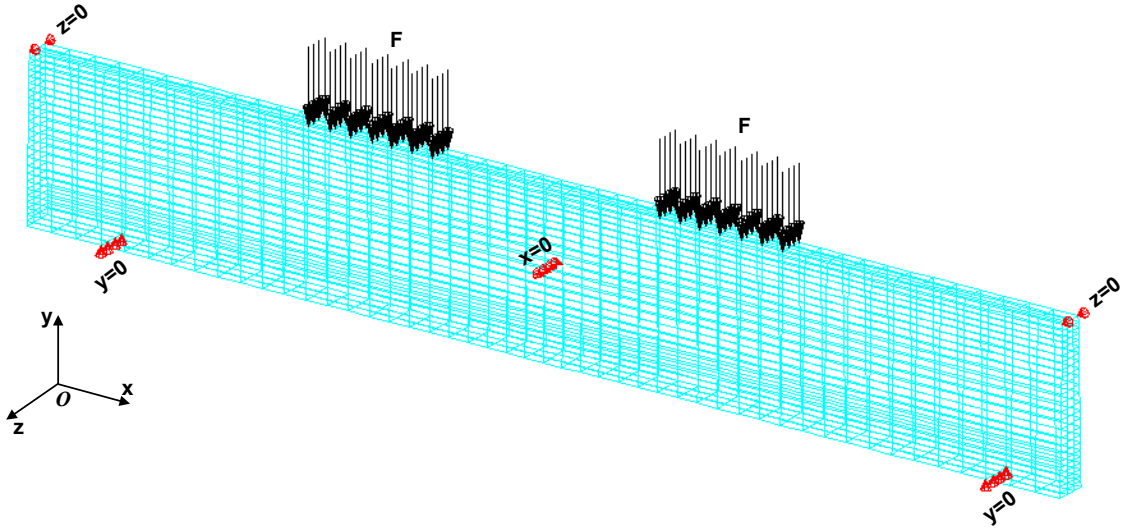

Figure 4.4: Example-1, Four-point bending boundary conditions and loading produces residual stress upon unloading, where $F = 67,200$ N

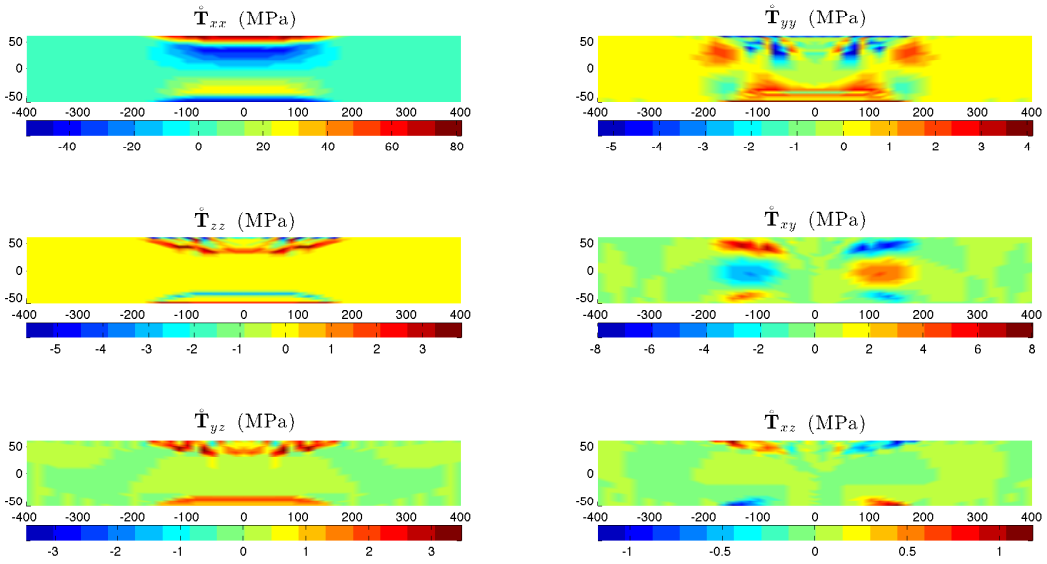

Figure 4.5: Example-1, Contour plots of the six components of the actual residual stress $\mathring{\mathbf{T}}_{FEA}$

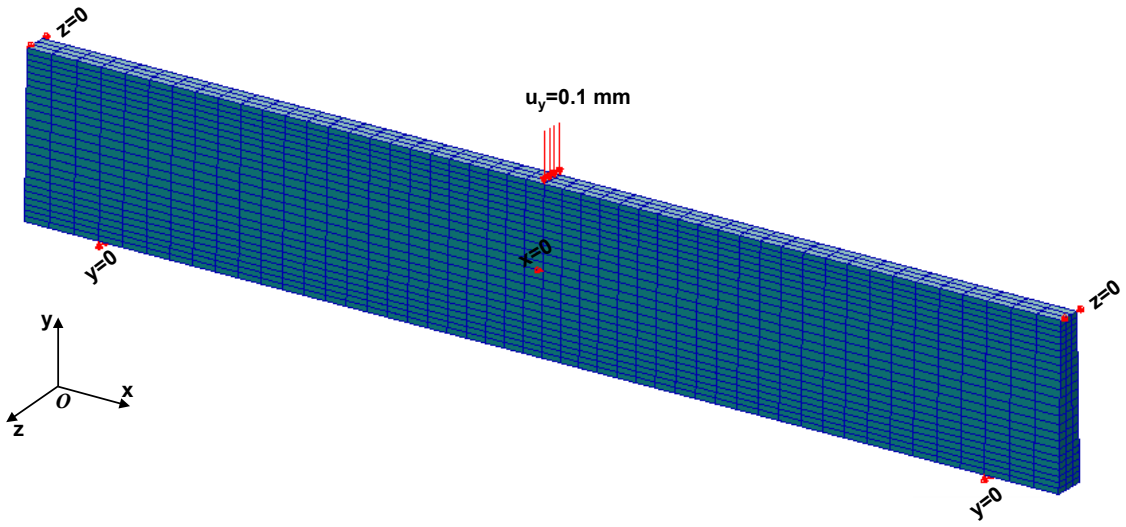

Figure 4.6: The first perturbation boundary conditions

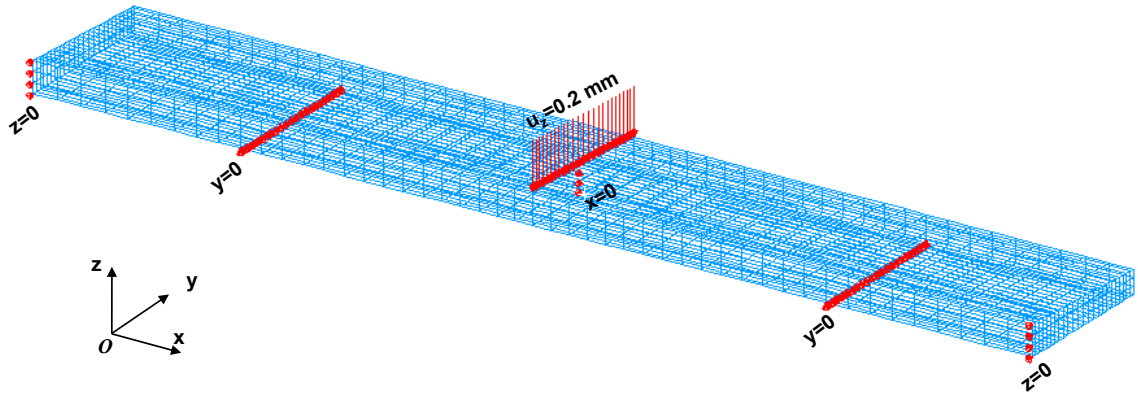

Figure 4.7: The second perturbation boundary conditions

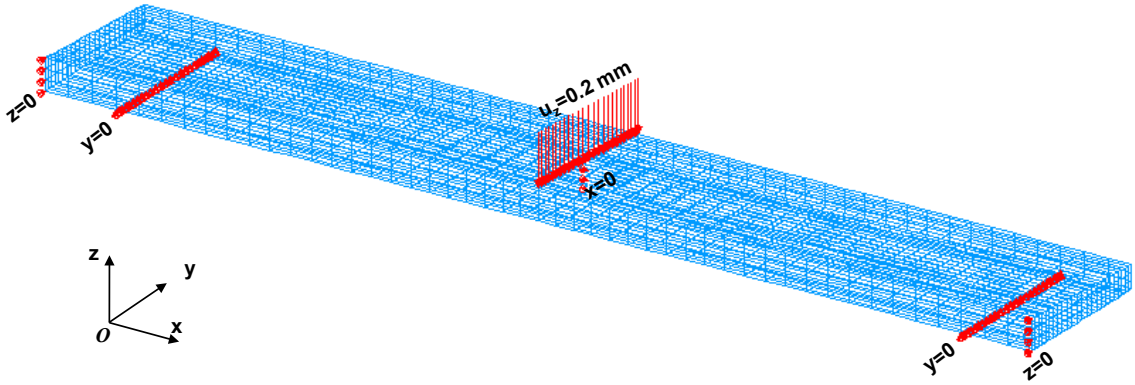

Figure 4.8: The third perturbation boundary conditions

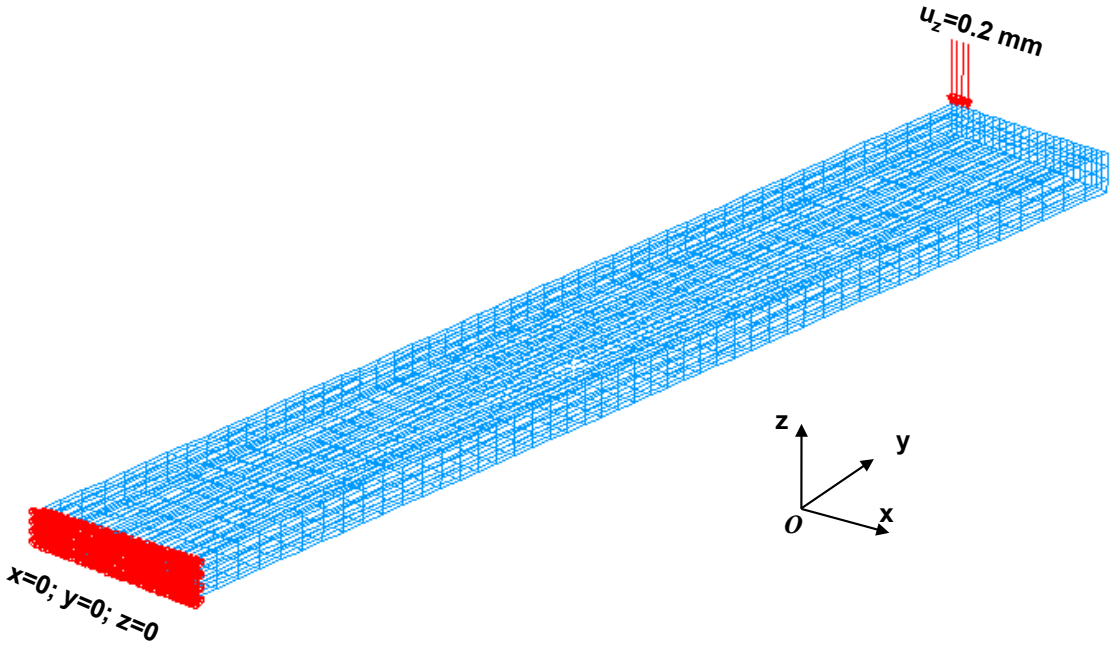

Figure 4.9: The forth perturbation boundary conditions

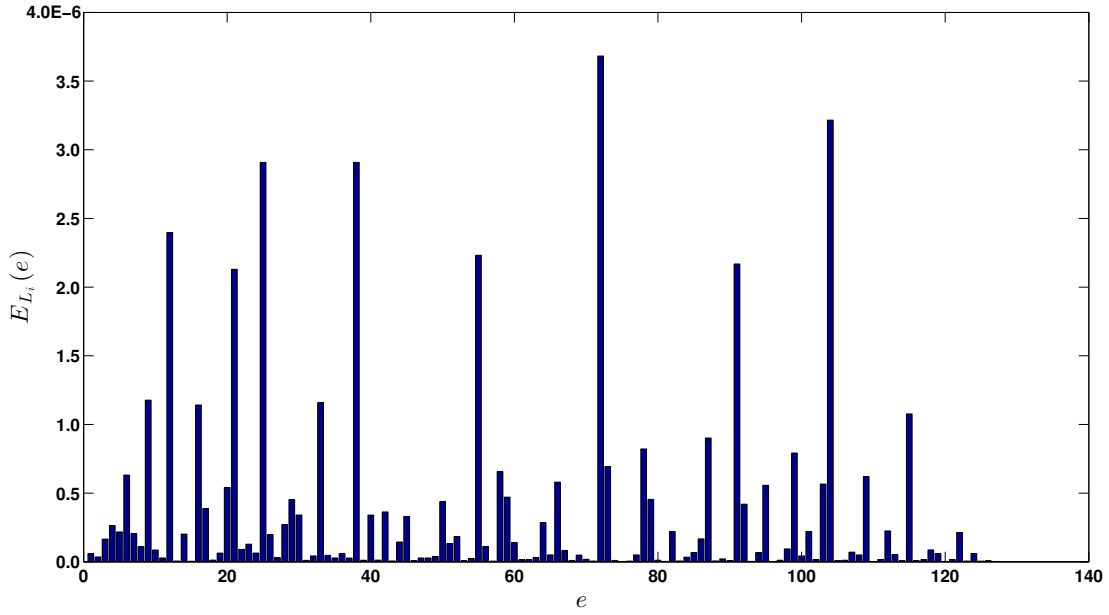

Figure 4.10: Example-1, element error norm $E_{Li}(e)$ versus element number e for example 1. All $E_{Li}(e)$ values are $< 4.0 \times 10^{-6}$, confirming the accuracy of all elemental incremental elasticity tensors obtained with ECSS-RCP method.

the resulting least-squares system of equations $\mathcal{G}_2\mathcal{X}_2 = \mathcal{B}_2$ can be solved for $\mathcal{X}_2$. However, the mesh geometry and the response of the beam to each perturbation do not guarantee 34008 independent equations. Indeed, the MatLab back-slash operator (version 2013b), used to solve this least-squares problem, reported the rank of the coefficient matrix $\mathcal{G}_2$ as 34006. Hence, a new perturbation was required to guarantee a sufficient number of independent equations for this example. Consequently, Eq. (4.20) for this example, with four perturbations, yields:

$$\underbrace{\begin{bmatrix} \mathbf{Z}_1^0 - \mathbf{Y}_1^0 & \mathbf{A}_1^0 \\ \mathbf{Z}_2^1 - \mathbf{Y}_2^0 & \mathbf{A}_2^0 \\ \mathbf{Z}_3^2 - \mathbf{Y}_3^0 & \mathbf{A}_3^0 \\ \mathbf{Z}_4^3 - \mathbf{Y}_4^0 & \mathbf{A}_4^0 \end{bmatrix}_{58800\times 34008}}_{\mathcal{G}_2} \underbrace{\begin{Bmatrix} \mathring{\mathbf{T}} \\ \mathbb{L}_0 \end{Bmatrix}_{34008\times 1}}_{\mathcal{X}_2} = \underbrace{\begin{Bmatrix} \left\{\mathbf{f}_h^{ext}\right\}_1^0 \\ \left\{\mathbf{f}_h^{ext}\right\}_2^0 \\ \left\{\mathbf{f}_h^{ext}\right\}_3^0 \\ \left\{\mathbf{f}_h^{ext}\right\}_4^0 \end{Bmatrix}_{58800\times 1}}_{\mathcal{B}_2} \tag{4.24}$$

Solution of this least-square problem [Eq. (4.24)] is then compared using the two error norm equations defined by Eqs. (4.22) and (4.23); and are shown in Fig. 4.10 and 4.11. Thus the errors in predicting the incremental elasticity tensors for all 128 elements are less than 4×10^{-8}. The error in computing nodal Cauchy stresses are very small for larger values $\left\| \left[\mathring{\mathbf{T}}_{FEA}\right]_n \right\|$, and in the contrary, it is larger for smaller values of $\left\| \left[\mathring{\mathbf{T}}_{FEA}\right]_n \right\|$. Nonetheless, the maximum defined error,

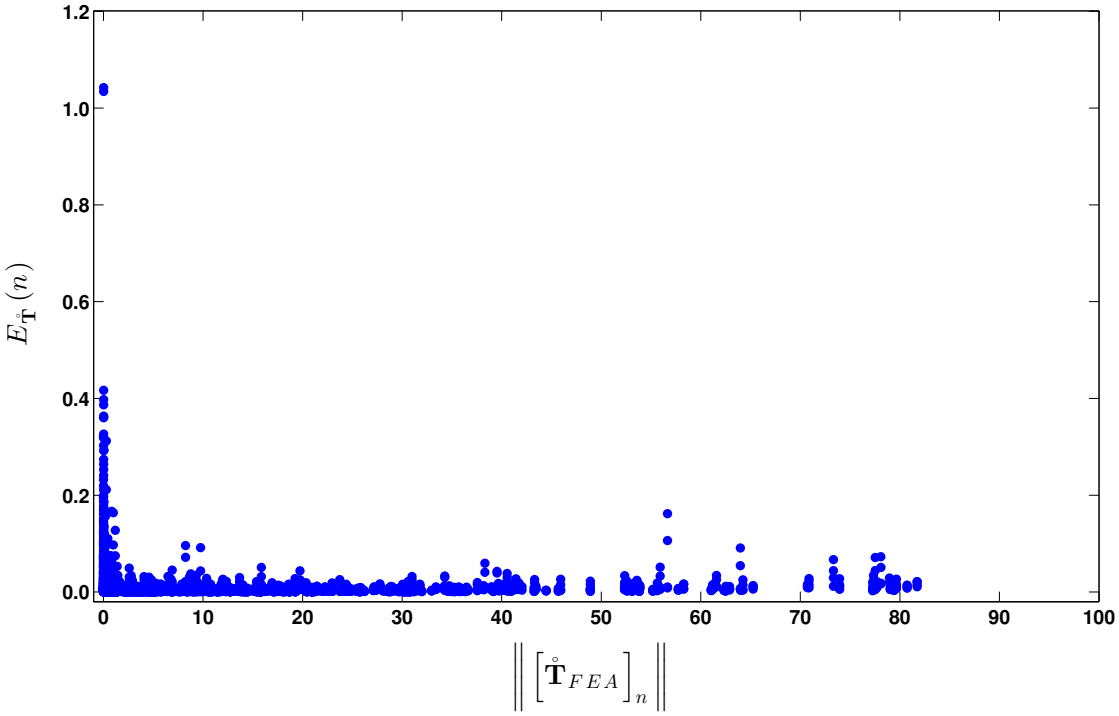

Figure 4.11: Example-1, $E_{\mathring{\mathbf{T}}}(e)$ versus $\left\| \left[\mathring{\mathbf{T}}_{FEA} \right]_n \right\|$. $E_{\mathring{\mathbf{T}}}(e)$ values are small for larger values of $\left\| \left[\mathring{\mathbf{T}}_{FEA} \right]_n \right\|$, and only in couple of nodes that $\left\| \left[\mathring{\mathbf{T}}_{FEA} \right]_n \right\|$ is almost zero, $E_{\mathring{\mathbf{T}}}(e)$ is as large as 1.

$E_{\mathring{\mathbf{T}}}(n)$, is less than 1.2.

Moreover, the actual contour plots of the six component of nodal Cauchy stress tensors, shown as a reference in Fig. 4.5, can be compared with the predicted nodal Cauchy stress components depicted in Fig. 4.12. Comparison of these two figures also furnishes a visual confirmation of the ECSS method for this example. However, visualization of a contour plot is limited to the outer surface of the beam. Consequently, another measure is to plot stresses on a path passing through the beam, as shown in Fig. 4.13. Both actual and predicted (ECSS) Cauchy stress components are shown in six subplots in Fig. 4.14. The predicted stress components are seen to be almost identical to the actual stress components.

Example 2: The residual stress field produced by a three-point bending experiment as shown in Fig. 4.15 from the two step analysis explained above with ABAQUS/Standard Solver to construct the configuration R_0 of the beam with residual stress fields shown in Fig. 4.16. The beam were then perturbed, in the absence of body forces, four times from reference configuration R_0. The boundary condition of each perturbations that yielded configurations R_1, R_2, and R_3 are shown in Fig. 4.6, Fig. 4.7, and Fig. 4.8, respectively. Three full-field displacements and traction forces were then

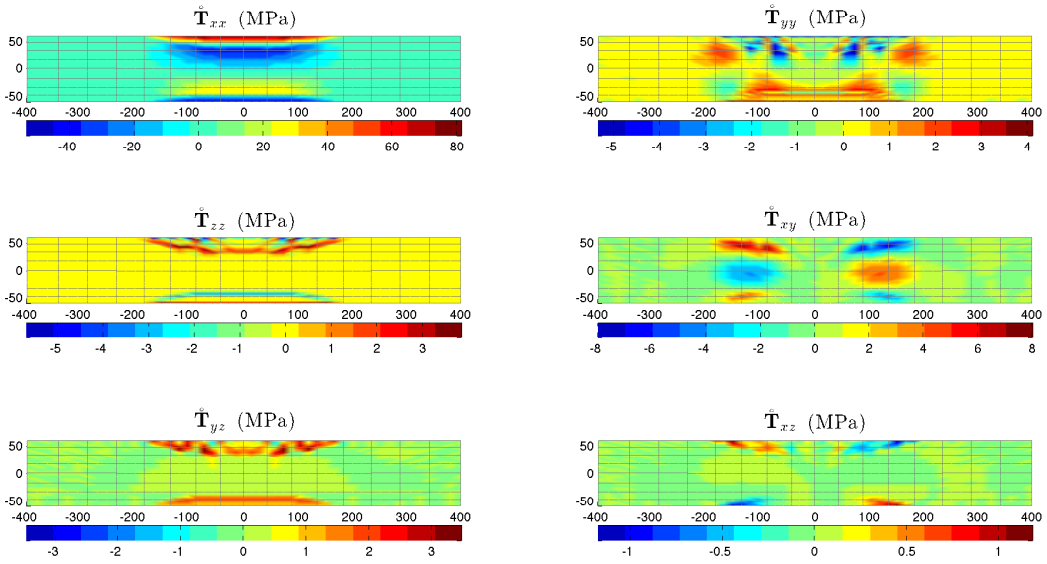

Figure 4.12: Example-1, Contour plots of the six components of the predicted residual stress $\mathring{\mathbf{T}}_{ECSS}$

extracted from linear static finite element analysis of the three perturbations, namely: $\left(\{\mathbf{u}_h\}_1^0\,,\,\{\mathbf{f}_h\}_1^0\right)$ from configuration R_1, $\left(\{\mathbf{u}_h\}_2^0\,,\,\{\mathbf{f}_h\}_2^0\right)$ from configuration R_2, and $\left(\{\mathbf{u}_h\}_3^0\,,\,\{\mathbf{f}_h\}_3^0\right)$ from configuration R_3. The total number of nodes defining the finite element mesh of the beam determined the total number of degrees-of-freedom (DOF) to be $DOF = 3N_n = 14700$. The total number of unknowns are $6N_n + 36Ne = 34008$. Thus, the required ECSS-RCP system of equations, defined for three perturbations by Eq. (4.20), yields a coefficient matrix $\mathcal{G}_2$ of size 44100×34008 and a forcing vector of $\mathcal{B}_2$ of size 44100×1. Hence, the formed least-squares system of equations of $\mathcal{G}_2\mathcal{X}_2 = \mathcal{B}_2$ can be solved for $\mathcal{X}_2$. However, contrary to the previous example, three perturbation produced sufficient independent equations; hence, the entire number of unknowns, 34008, were computed using MatLab. Similar to previous example, the solution is then compared using the two error norm equations defined by Eqs. (4.22) and (4.23); and are shown in Fig. 4.17 and 4.18. Hence, the errors in predicting the incremental elasticity tensors for all 128 elements are less than 3.5×10^{-9}. The error in computing nodal Cauchy stresses are very small for larger values $\left\| \left[\mathring{\mathbf{T}}_{FEA}\right]_n \right\|$, and in the contrary, it is larger for smaller values of $\left\| \left[\mathring{\mathbf{T}}_{FEA}\right]_n \right\|$. Nonetheless, the maximum defined error, $E_{\mathring{\mathbf{T}}}(n)$, is less than 3.0×10^{-3}.

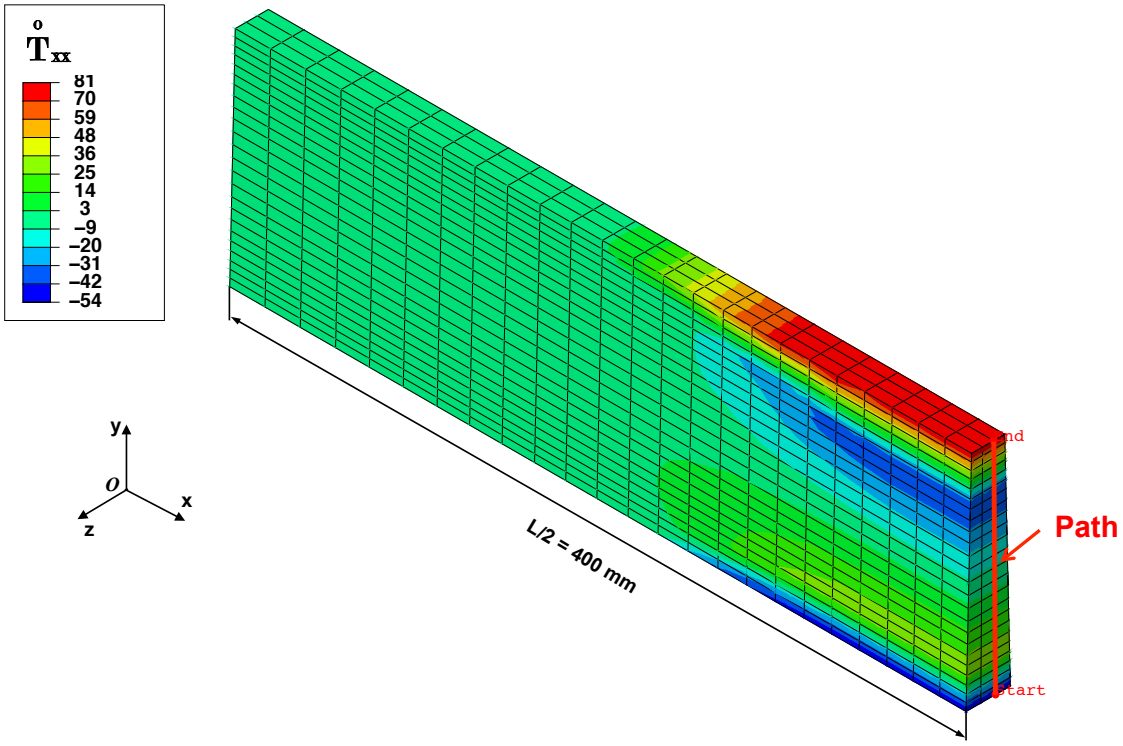

Figure 4.13: Example-1, A beam mid-section path on xx-component of the $\mathring{\mathbf{T}}_{FEA}$ contour plot

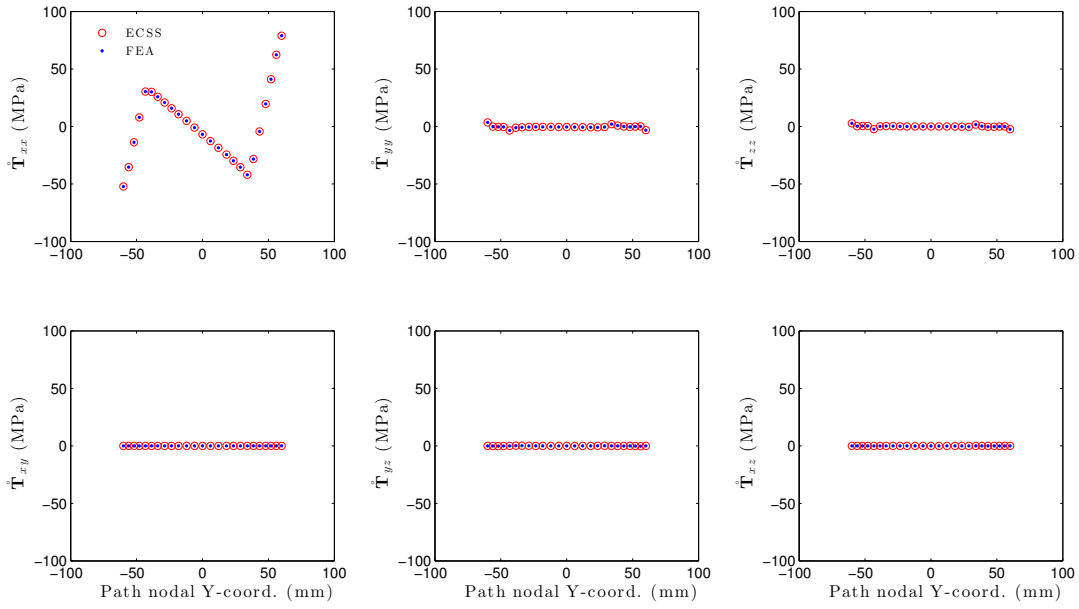

Figure 4.14: Example-1, $\mathring{\mathbf{T}}$ components of nodes on the path shown in Fig. 4.13

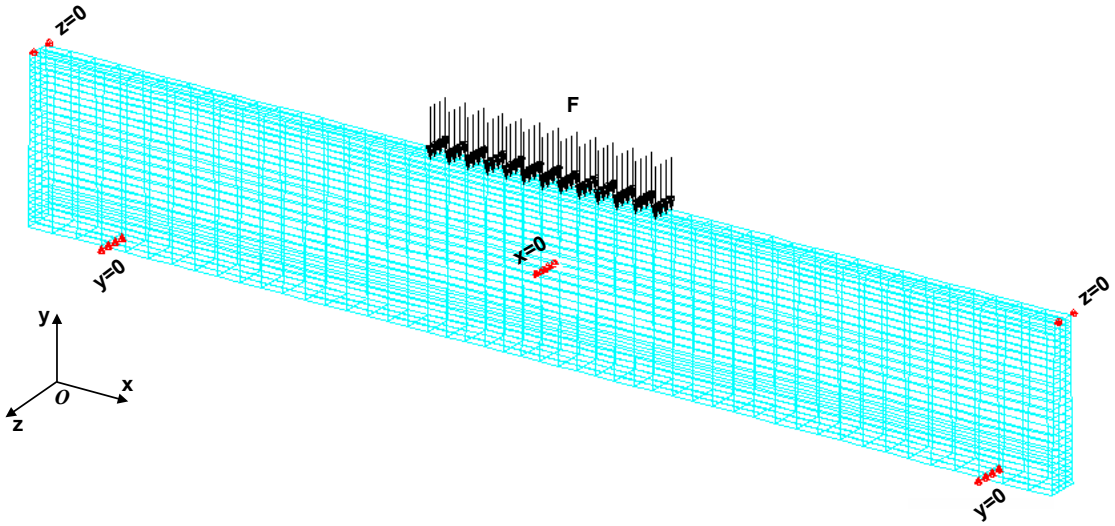

Figure 4.15: Example-2, three-point bending boundary conditions and loading produces residual stress upon unloading, where $F = 58,500$ N.

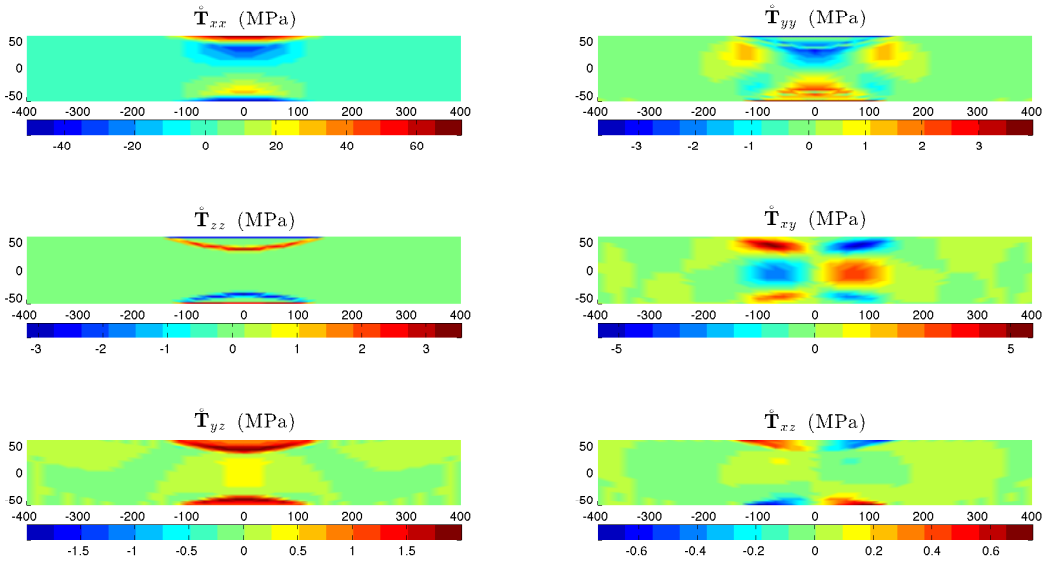

Figure 4.16: Example-2, Contour plots of the six components of the FEA residual stress $\mathring{\mathbf{T}}_{FEA}$

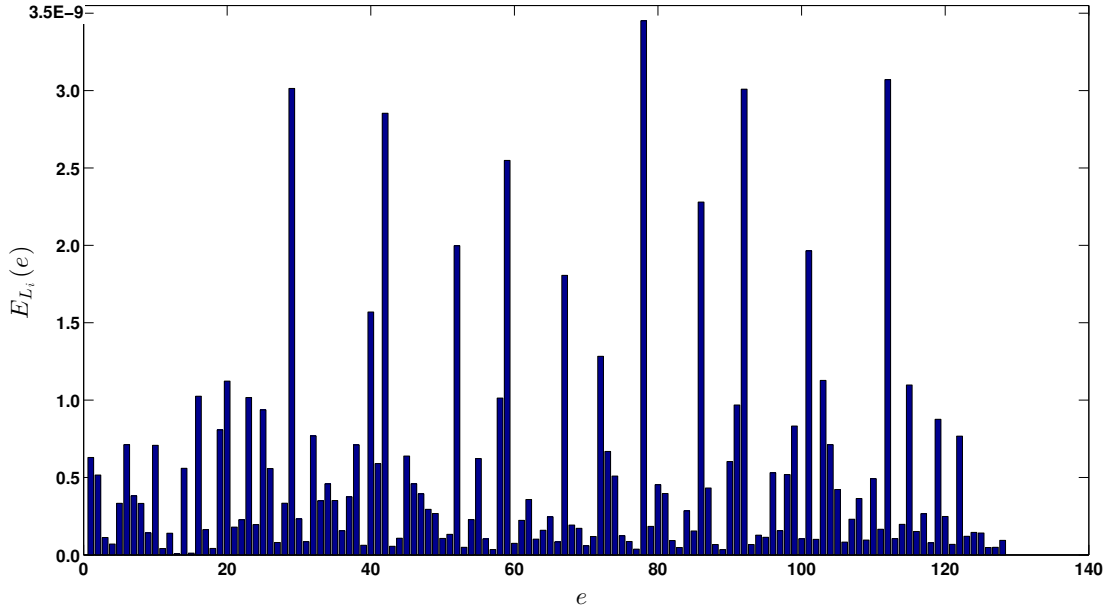

Figure 4.17: Example-2, element error norm $E_{Li}(e)$ versus element number e for example 2. All $E_{Li}(e)$ values are $< 3.5 \times 10^{-9}$, confirming the accuracy of all elemental incremental elasticity tensors obtained with ECSS-RCP method.

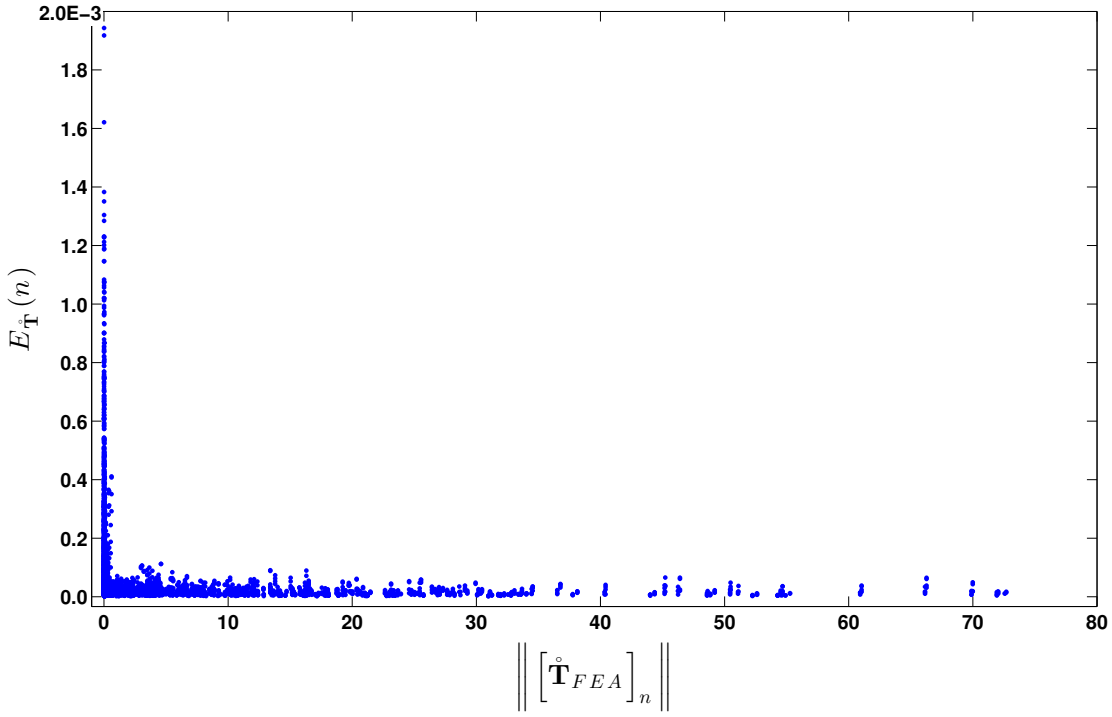

Figure 4.18: Example-2, $E_{\mathring{\mathbf{T}}}(e)$ versus $\left\| \left[\mathring{\mathbf{T}}_{FEA} \right]_n \right\|$. $E_{\mathring{\mathbf{T}}}(e)$ values are small for larger values of $\left\| \left[\mathring{\mathbf{T}}_{FEA} \right]_n \right\|$, and only in couple of nodes that $\left\| \left[\mathring{\mathbf{T}}_{FEA} \right]_n \right\|$ is almost zero, $E_{\mathring{\mathbf{T}}}(e)$ is as large as 2×10^{-3}.

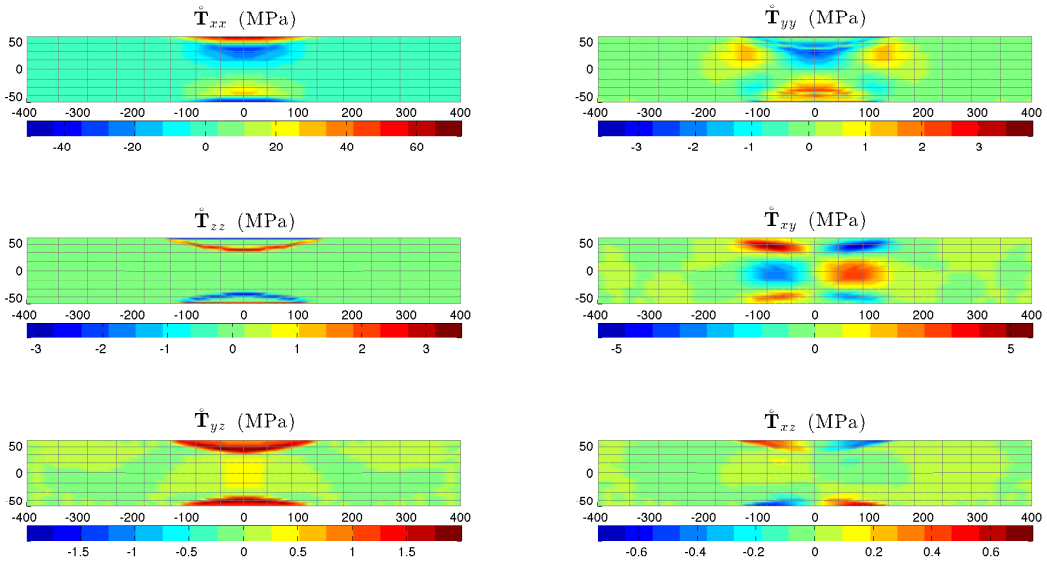

Figure 4.19: Example-2, Contour plots of the six components of the predicted residual stress $\mathring{\mathbf{T}}_{ECSS}$

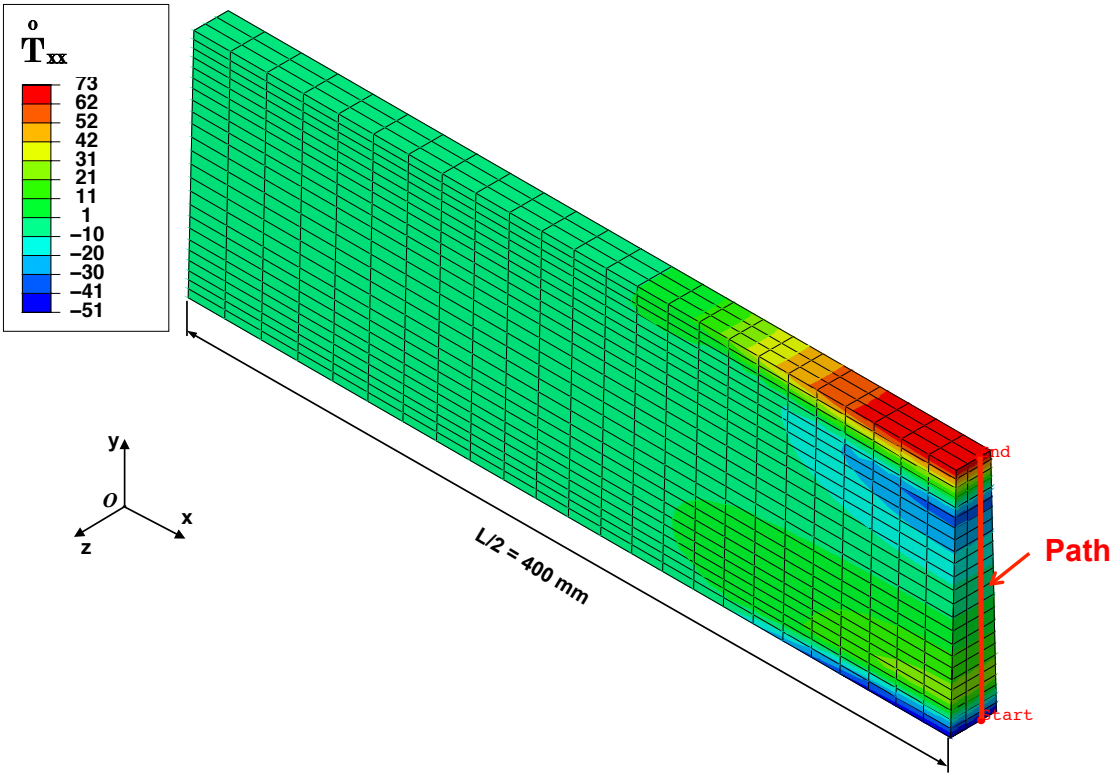

Figure 4.20: Example-2, A beam mid-section path on xx-component of the $\mathring{\mathbf{T}}_{FEA}$ contour plot

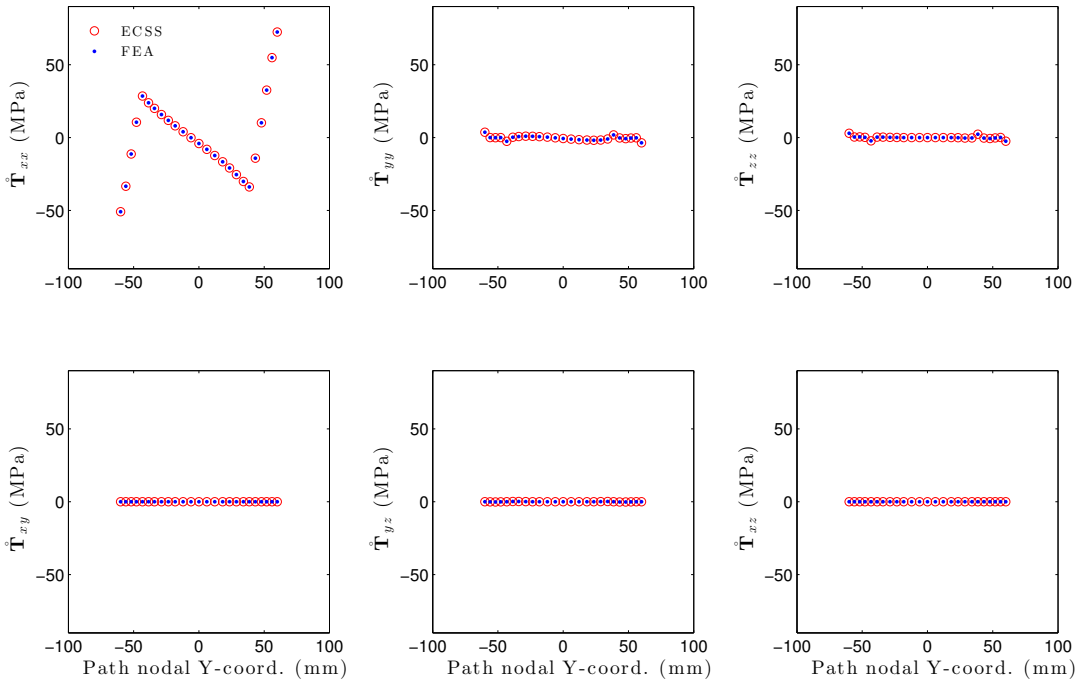

Figure 4.21: Example-2, $\mathring{\mathbf{T}}$ components of nodes on the path shown in Fig. 4.20

As in the previous example, the actual nodal Cauchy stress components (Fig. 4.16) can be compared with that of predicted ones, as shown in Fig. 4.19. Once again a comparison of these two figures provides a visual validation of the ECSS method. Moreover, the plot of stress components plot along a path passing through the mid-section of the beam - see Fig. 4.20. is shown in Fig. 4.21. The predicted stress components are almost identical to the actual stress components.

4.6 Discussion

The ECSS method addresses two problems of material identification. It not only furnishes the material incremental tensor for each element, but also supplies the current state-of-stress tensor at each node. Displacement and force full-field measurements are required for three or more linear perturbations as inputs to RULFEM and ECSS. As in other methods (e.g., FEMU, CEGM, VFM, EGM, and RGM), where balance laws of mechanics are solved using a numerical technique such as finite differences, boundary elements or FEM, to determine material property parameters, the RULFEM and ECSS methods deliver equilibrium states states by utilizing FEA . Except for VFM, RULFEM and ECSS, the other methods convert numerical forms of the balance laws into optimization problems with different cost functions. Unlike previous methods, however (including VFM), ECSS and RULFEM directly solves a least-squares set of equations and do not require any

assumptions whatsoever regarding constitutive response beyond incremental linearity. Both yield the material incremental elasticity tensor ($\mathbb{L}^e$) and elasticity tensor ($\mathbb{C}^e$), respectively, for each element of the mesh comprising the discretization of the domain. In marked contrast, all of other methods generate the material constants of an *a priori* assumed constitutive model. Further while VFM does not solve an optimization problem to determine the material constants, it does require an optimized particular (virtual) displacement field to achieve acceptable results.

ECSS yields the elemental incremental elasticity tensor, $\mathbb{L}^e$, which is a fourth-order tensor with minor symmetry that can be represented as a (6×6) matrix, whereas the basic RULFEM yields elemental $\mathbb{C}^e$, which is a fourth-order tensor having no symmetry; i.e., it cannot generally be represented as a symmetric (9×9) matrix. Hence, application of RULFEM to bodies with unknown stresses at the initial configuration generates erroneous elements of $\mathbb{C}^e$, since $\mathbb{C}_0[\mathbf{H}] = \mathbf{H}\overset{\circ}{\mathbf{T}} + \mathbb{L}_0[\mathbf{E}]$ [19, 28].

The ECSS CSS capability can be contrasted with existing residual stress measurement techniques. ECSS does not require - and in fact is incompatible with - any *a priori* assumptions about the constitutive model of any element; whereas, both destructive (HDM, RCM, DHM, ST, CM, etc.) and nondestructive (X-ray, neutron diffraction, eddy current, ultrasound) measurement techniques are based on *a priori* material constitutive models, and they do not allow for different material properties in different finite elements.

The ECSS method is a nondestructive method of determining the CSS (residual stress in the absence of the external forces), and also effective at generating both the stress tensor field and the material tensor field throughout the entire body. The destructive techniques, however, provide either local stress tensor fields, or bending and axial stress components only, whereas nondestructive techniques are limited in in terms of depth beyond $10\,cm$ [24]. The only disadvantage of the ECSS method is that it requires full-field displacement and force measurements throughout the entire mesh defining the body.

Like inverse methods, RULFEM and ECSS have some limitations, which are (1) each finite element is made of a uniform material, (2) the measurement of the required force fields imposes a practical limitation, and (3) the coefficient matrix might become rank deficient or have a high condition number. However, the first limitation can be resolved by changing the mesh size and density if doing so yields no clear distinction. An easy solution to the third limitation is to measure additional perturbations, as shown in Example-1 of the validation section, and/or to use numerical preconditioning techniques to reduce the condition number of the coefficient matrix. The second and third limitations can also be addressed in a more detailed fashion, to be addressed in our future work.

Another major benefit of ECSS and RULFEM lies in rapid solution of the attendant linear algebraic problem. With advances in numerical computation, such as iterative methods, preconditioning and parallelization, solving a least-squares problem with severely sparse coefficient matrix is rapidly becoming feasible and practical.

Further, ECSS addresses one of the main limitations of RUFEM; namely, that RULFEM initiates by perturbing the body from a stress-free state, while ECSS does not suffer from this limitation. Moreover, ECSS enjoys the freedom of FEA in meshing virtually any geometry; ECSS can there-

fore be applied to actual parts without any assumptions except linearity within the perturbation step and uniformity of the material within each finite element. The former assumption can be tested inequality Eq. (2.7), and the latter can be tested by re-meshing or mesh refinement. However, once measured full-field displacement and force fields become available, solution of the derived least-squares system of equations is straightforward and efficient.

4.7 Conclusion

A reverse updated Lagrangian finite element method (ECSS) that provides nonlinear element-wise mechanical properties of 3D solid bodies (with deformed configurations tracked by incremental linear steps) and the CSS at each nodes was developed in this study. ECSS is also capable of finding nodal residual stress tensors, a special case of self-equilibrated body under no external loads. Similar to RULFEM method [28], ECSS formulation relies on the solution of a linear least-squares system of equations and yields element-wise, fourth-order incremental elasticity tensors and nodal stress tensors for small displacement (or force) perturbations. The novelty of ECSS is that it neither requires an *a priori* assumed material constitutive law, nor requires assuming stress-free configuration of the body. ECSS only assumes incremental linearity of the deforming material and material uniformity within each element used to discretized the body. The validity of the method was demonstrated by numerical noise-free input examples. Since ECSS and RULFEM [28] are based on ULFEA, the local and global error prediction tools developed in [28] are directly applicable to ECSS.

Similar to RULFEM [28], the accuracy and efficiency of ECSS depend on the accuracy and precision of the input displacement and force measurements. Mesh distortion after several perturbations might necessitate re-meshing. Further, the accuracy of ECSS strongly depends on the perturbation and efficacy of the measuring system to closely track the nodal displacements while the body is incrementally deformed. The sensitivity of ECSS is rooted in the high condition number of the coefficient matrix $\mathcal{G}_1$ or $\mathcal{G}_2$. The linearity of the perturbation can be tested directly by verifying the Eq. (2.7) inequality. Measurement related noise and errors can also cause sever error with high condition numbers of the coefficient matrix ($\mathcal{G}_1$ or $\mathcal{G}_2$) and the force vectors ($\mathcal{B}_1$ or $\mathcal{B}_2$). However, the local and global error prediction tools as well as upper-bound error prediction developed in [28] are directly applicable to ECSS.

Chapter 5

Dynamically Estimating Residual Stress, DERS

5.1 Introduction

The objective of this presentation is to introduce a nondestructive inverse FEA method, named Dynamically Estimating Residual Stress (DERS), capable of predicting (1) residual stress at nodal positions of the discretized body, (2) elemental incremental elasticity tensors, and (3) elemental mass density. Except for elemental mass density, the objective of the present chapter is similar to that of the previous chapter. The input data to the ECSS method are extracted from linear static perturbations; however, the input data to the DRES method are extracted from linear vibratory perturbations, such as modal testing or shaker-table forced vibration testing. Similar to ECSS and most exiting material identification techniques and destructive stress measurement techniques, DERS requires full-field displacement and force of the body after each small (linear) perturbation of the body with respect to its current configuration. Similar DERS does not require *a priori* constitutive assumptions; however, the only assumption is made in development of DERS that the solid bodies are made of materials with negligible damping (viscoelastic) properties. This assumption still covers a large group of metals and composites. In addition to stress tensor field throughout the entire solid body, DERS directly yields the elemental incremental elasticity tensors and elemental mass density. Similar to RULFEM (chapter 3, [28]),

DERS generates an overdetermined linear least-squares type of system of equations without any nonlinear constraints. The coefficient matrix may have a high condition number or become rank insufficient. Hence, a small random error in the nodal displacement measurement and/or nodal force vectors may generate erroneous results. Displacement measurements are acquired with imagining techniques; thus, small measurement errors are inevitable. Global and local error assessment for such system is developed and validated in development of Chapter 3 RULFEM [28]; hence, they are no longer discussed in this exposition. DERS method is developed for dynamics perturbations; hence, several near multiple resonance perturbations are required. The ECSS method is validated in previous chapter. Since ECSS and DERS methods are similar, there is no

need for a validation section in this chapter.

5.2 Theory

As in RULFEM [28] (see Chapter 3) and ECSS (see Chapter 4) the development of the DERS theory follows updated Lagrangian finite element method (ULFEM) formulation (see Chapter 2), theory of linear elasticity with initial stress under dead loading. Because, ECSS and DECSS share very similar objectives, and they are developed from ULFEM, DERS can be considered a special case of ECSS, which is applicable to solids with negligible damping ratio (negligible viscoelastic response). Hence, similar to ECSS, at least *three* sets of measured full-field displacements and *three* corresponding sets of measured tractions are required to determine the six components of nodal Cauchy stresses, local (element-wise) fourth-order incremental elasticity tensors (without any *a priori* assumptions about a particular constitutive model) and elemental mass density. Neither ECSS nor DERS require cost functions or a virtual displacement field. There are, however, two limitations to the method, (1) the first limitation is shared with ECSS and RULFEM, i.e., each finite element is assumed to consist of a single uniform material, (2) the solid body has negligible damping (viscoelasticity) properties. While the former limitation arises from finite element formulation, the latter limitation roots from the perturbing technique. DERS input field data (i.e., displacement and traction force fields) are collected from dynamic (vibratory) experiments with harmonic excitation, such as: modal testing, shaker table testing, actual part responses under different known vibratory harmonic sources, etc.

The goal of the DERS as an inverse problem, is to find the components of the body residual stresses, i.e. the nodal Cauchy stress tensors, $\mathring{\mathbf{T}}_n$, the incremental elasticity tensors, $\mathbb{L}_0^e$, and the elemental density, ρ_0^e for each element e. The unknown nodal state of Cauchy stress is a symmetric matrix; hence, each nodal stress tensor $\mathring{\mathbf{T}}_n$ or node n has six unknowns. Where the vector form of all the nodal Cauchy stress tensors becomes $\left\{\mathring{\mathbf{T}}\right\}$ and its size is $(6N_n) \times 1$. The other unknown is the elemental incremental elasticity tensor, $\mathbb{L}_0^e$, that posses minor symmetry [19]; hence, it has total of 36 unknowns per elements. Where the vector form of all the elemental incremental elasticity tensors becomes $\{\mathbb{L}_0\}$ and its size is $(36N_e) \times 1$. Lastly, there are N_e number of unknown elemental densities, ρ_0^e. Total number of unknowns in the inverse problems becomes $6N_n + 37N_e$, which is more than twice as much as total number of equations provided by the weak form of the momentum balance (including the inertia term), Eq. (2.40). Thus, the minimum number of independent perturbations are required to obtain minimum number of independent equations is three; provided the body Ω at configuration R_0 is discretized with 64-node hexagonal elements. Where each known perturbation provides a pair of displacement, $\{\mathbf{u}_h\}_{n+1}^n$ and force $\{\mathbf{f}_h\}_{n+1}^n$ full field data. Ultimately, the total unknown vectors become $\left\{\rho_0, \mathring{\mathbf{T}}, \mathbb{L}_0\right\}^T$.

The DERS formulation starts from the weak form integration equation Eq. (2.40), where in short it shown in matrix form presented in Eq. (2.44). The linearized first Piola–Kirchhoff stress [Eq. (2.13)] in the stiffness term, $\{\Pi(\mathbf{u})\}_1^0$, and force vector term, $\{\mathbf{f}\}_0^0$, are developed in Chapters 2, 3, and 5.

$$\begin{aligned}
&\mathop{\mathcal{A}}_{e=1}^{N_e}\left\{\int_{R_0}\left([\boldsymbol{\phi}^e]^T\rho_n^e[\boldsymbol{\phi}^e]\right)d\mathrm{V}_n^e\right\}\{\mathbf{a}_h^e\}_1^0+\mathop{\mathcal{A}}_{e=1}^{N_e}\left\{\int_{R_0}\left([\mathbf{B}^e]^T\left(\mathbf{I}+[\mathbf{B}^e]\{\mathbf{u}_h^e\}_1^0\right)[\boldsymbol{\phi}^e]\right)d\mathrm{V}_0^e\right\}\left\{\overset{\circ}{\mathbf{T}}\right\}\\
&\quad+\mathop{\mathcal{A}}_{e=1}^{N_e}\left\{\int_{R_0}\left(\left[\mathbf{B}_{sym}^e\right]^T[\mathbb{L}_0^e]\left[\mathbf{B}_{sym}^e\right]\right)d\mathrm{V}_0^e\right\}\{\mathbf{u}_h\}_1^0\\
&=\mathop{\mathcal{A}}_{e=1}^{N_e}\left\{\int_{\Gamma_{q0}^e}\left([\boldsymbol{\phi}^e]^T\left(\mathbf{I}+[\mathbf{B}^e]\{\mathbf{u}_h^e\}_1^0\right)\Psi_0\left(\mathbf{N}_0^0\right)\right)d\mathrm{A}_0^e\right\}\left\{\overset{\circ}{\mathbf{T}}\right\}+\mathop{\mathcal{A}}_{e=1}^{N_e}\left\{\int_{\Gamma_{q0}^e}\left([\boldsymbol{\phi}^e]^T\bar{\mathbf{s}}\right)d\mathrm{A}_0^e\right\}
\end{aligned}\tag{5.1}$$

However, for residually stressed solid body as discussed in Chapter 2, in the absence of body forces and tractions, i.e., $\left(\overset{\circ}{\mathbf{b}},\overset{\circ}{\mathbf{t}}\right)=(\mathbf{0},\mathbf{0})$, $\overset{\circ}{\mathbf{T}}$ is the residual stress. Thus Eq.(2.1) and its weak form become

$$div\left(\overset{\circ}{\mathbf{T}}\right)=\mathbf{0};\tag{5.2}$$

$$\mathop{\mathcal{A}}_{e=1}^{N_e}\left\{\int_{R_0}\left([\mathbf{B}^e]^T[\boldsymbol{\phi}^e]\right)d\mathrm{V}_0^e\right\}\left\{\overset{\circ}{\mathbf{T}}\right\}=\mathop{\mathcal{A}}_{e=1}^{N_e}\left\{\int_{\Gamma_{q0}^e}\left([\boldsymbol{\phi}^e]^T\Psi_0\left(\mathbf{N}_0^0\right)\right)d\mathrm{A}_0^e\right\}\left\{\overset{\circ}{\mathbf{T}}\right\}\tag{5.3}$$

hence the two equal terms shown in Eq. (5.3) are canceled out from the two sides of Eq. (5.1) and it yields:

$$\begin{aligned}
&\underbrace{\mathop{\mathcal{A}}_{e=1}^{N_e}\left\{\int_{R_0}\left([\boldsymbol{\phi}^e]^T\rho_n^e[\boldsymbol{\phi}^e]\right)d\mathrm{V}_n^e\right\}\{\mathbf{a}_h^e\}_1^0}_{[\mathbf{M}]_0^0\{\mathbf{a}_h^e\}_1^0}+\underbrace{\mathop{\mathcal{A}}_{e=1}^{N_e}\left\{\int_{R_0}\left([\mathbf{B}^e]^T\left([\mathbf{B}^e]\{\mathbf{u}_h^e\}_1^0\right)[\boldsymbol{\phi}^e]\right)d\mathrm{V}_0^e\right\}}_{\mathbf{Z}\left(\{\mathbf{u}_h^e\}_1^0\right)=\mathbf{Z}_1^0}\left\{\overset{\circ}{\mathbf{T}}\right\}+\\
&\underbrace{\mathop{\mathcal{A}}_{e=1}^{N_e}\left\{\int_{R_0}\left(\left[\mathbf{B}_{sym}^e\right]^T[\mathbb{L}_0^e]\left[\mathbf{B}_{sym}^e\right]\right)d\mathrm{V}_0^e\right\}}_{\mathbf{K}_0}\{\mathbf{u}_h\}_1^0\\
&=\underbrace{\mathop{\mathcal{A}}_{e=1}^{N_e}\left\{\int_{\Gamma_{q0}^e}\left([\boldsymbol{\phi}^e]^T\left([\mathbf{B}^e]\{\mathbf{u}_h^e\}_1^0\right)\Psi_0\left(\mathbf{N}_0^0\right)\right)d\mathrm{A}_0^e\right\}}_{\mathbf{Y}\left(\{\mathbf{u}_h^e\}_1^0,\mathbf{N}_0^0\right)=\mathbf{Y}_1^0}\left\{\overset{\circ}{\mathbf{T}}\right\}+\underbrace{\mathop{\mathcal{A}}_{e=1}^{N_e}\left\{\int_{\Gamma_{q0}^e}\left([\boldsymbol{\phi}^e]^T\bar{\mathbf{s}}\right)d\mathrm{A}_0^e\right\}}_{\{\mathbf{f}_h^{ext}\}_1^0}
\end{aligned}\tag{5.4}$$

The elemental incremental elasticity tensors are decoupled in the third term of the left hand-side of Eq. (5.4) as shown in chapter 4 and shown in development of Eq. (3.9). Harmonic excitation of the body allows ignoring the body force term; hence, the concise form of Eq. (5.4) become

$$[\mathbf{M}]_0^0\{\mathbf{a}_h\}_1^0+\left[\mathbf{Z}_1^0-\mathbf{Y}_1^0\right]\left\{\overset{\circ}{\mathbf{T}}\right\}+\mathbf{A}_1^0\{\mathbb{L}_0\}=\{\mathbf{f}_h^{ext}\}_1^0\tag{5.5}$$

Harmonic excitation force can be written as $\left\{\mathbf{f}_h^{ext}\right\}_1^0=\mathbf{F}_1^0\exp(i\omega_1 t)$, where $i=\sqrt{-1}$, $\mathbf{F}_1^0$ and ω_1 are the excitation force amplitude and angular frequency, respectively. Therefore, the displacement response vector is harmonic [25] i.e.

$$\{\mathbf{u}_h\}_1^0 = \{\mathbf{U}_h\}_1^0 \exp(i\omega_1 t + \theta) \tag{5.6}$$

where $\{\mathbf{U}_h\}_1^0$ is the displacement response amplitude and $\theta \approx 0$, because the body's damping is negligible. The harmonic displacement response yields the harmonic acceleration of

$$\{\mathbf{a}_h\}_1^0 = -\omega^2 \{\mathbf{U}_h\}_1^0 \exp(i\omega_1 t + \theta) = -\omega^2 \{\mathbf{u}_h\}_1^0 \tag{5.7}$$

Making use of Eq. (5.4), (5.7) and (5.6) in Eq. (5.5) or Eq. (5.4) yields the following time independent equation:

$$\begin{aligned} -\omega^2 [\mathbf{M}]_0^0 \{\mathbf{U}_h\}_1^0 \exp(i\omega_1 t) + \left[\bar{\mathbf{Z}}_1^0\left(\{\mathbf{U}_h\}_1^0\right) - \bar{\mathbf{Y}}_1^0\left(\{\mathbf{U}_h\}_1^0\right)\right]\left\{\mathring{\mathbf{T}}\right\}\exp(i\omega_1 t) \\ + \bar{\mathbf{A}}_1^0\left(\{\mathbf{U}_h\}_1^0\right)\{\mathbb{L}_0\}\exp(i\omega_1 t) = \{\mathbf{F}_h^{ext}\}_1^0 \exp(i\omega_1 t) \end{aligned} \tag{5.8}$$

where $\bar{\mathbf{Z}}_1^0$, $\bar{\mathbf{Y}}_1^0$, and $\bar{\mathbf{A}}_1^0$ are defined matrices in Eq. (5.4) and are functions of the harmonic displacement amplitude. This presentation of Eq. (5.8) indicates that the exponent term can be canceled from both side of the equation yielding a time independent relationship of

$$-\omega_1^2 [\mathbf{M}]_0^0 \{\mathbf{U}_h\}_1^0 + \left[\bar{\mathbf{Z}}_1^0 - \bar{\mathbf{Y}}_1^0\right]\left\{\mathring{\mathbf{T}}\right\} + \bar{\mathbf{A}}_1^0 \{\mathbb{L}_0\} = \{\mathbf{F}_h^{ext}\}_1^0 \tag{5.9}$$

The elemental density is in the first term of Eq. (5.9), i.e. mass matrix ($[\mathbf{M}]_0^0$), which can be decoupled by the technique presented in Section 4.3 as

$$\sum_{e=1}^{Ne} \frac{\partial [\mathbf{M}]_0^0}{\partial \rho^e} \{\mathbf{a}_h\}_1^0 = [\mathbf{G}]_1^0 \{\boldsymbol{\rho}_0\} \tag{5.10}$$

where $[\mathbf{G}]_0^0$ is a matrix of size $(3N_n) \times N_e$, and $\{\boldsymbol{\rho}_0\}$ is the unknown elemental density vector or size $N_e \times 1$. Hence, the matrix form of Eq. (5.9) with the inverse unknown vector of $\left\{\rho_0, \mathring{\mathbf{T}}, \mathbb{L}_0\right\}^T$ becomes

$$\underbrace{\begin{bmatrix} -\omega_1^2\mathbf{G}_1^0 & \mathbf{Z}_1^0 - \mathbf{Y}_1^0 & \mathbf{A}_1^0 \end{bmatrix}}_{3N_n \times (6N_n + 37N_e)} \underbrace{\begin{Bmatrix} \boldsymbol{\rho}_0 \\ \mathring{\mathbf{T}} \\ \mathbb{L}_0 \end{Bmatrix}}_{(6N_n+37N_e)\times 1} = \{\mathbf{F}_h^{ext}\}_1^0 \tag{5.11}$$

Since the number of unknowns $(6N_n) + (37N_e)$ is larger than the number of equations $(3N_n)$, i.e., number of DOF, more equations are necessary. At least total of three independent set of equations are required that can be generated by three independent perturbations. Since the body eigenvectors are orthogonal, the most suitable three perturbations can be obtained by exciting the solid body at vicinity of the first three eigenvalues (natural frequencies). Theoretically, any three or more independent natural natural frequencies provides sufficient independent sets of equations;

however, larger excitation energy is required to excite the modes with higher natural frequencies. Thus, the response amplitudes are expected to suffer at higher natural modes (higher frequencies). For sake of demonstration, suppose body Ω shown in Fig. 4.2 at its configuration R_0 is excited at its first three non-rigid body natural frequencies of ω_1, ω_2, and ω_3 attaining configurations R_1, R_2, and R_3, respectively, at their maximum response amplitudes. The three harmonic excitations yield three harmonic sets of displacement and force measurement vectors with harmonics amplitudes of $\left(\{\mathbf{U}_h\}_1^0, \left\{\mathbf{F}_h^{ext}\right\}_1^0\right)$, $\left(\{\mathbf{U}_h\}_2^0, \left\{\mathbf{F}_h^{ext}\right\}_2^0\right)$, and $\left(\{\mathbf{U}_h\}_3^0, \left\{\mathbf{F}_h^{ext}\right\}_3^0\right)$ corresponding to the three excitation frequencies of ω_1, ω_2, and ω_3. The three measurement sets can form three sets of equations as formulated in Eq. (5.11) and they are combined as one system of equations of

$$\underbrace{\begin{bmatrix} -\omega_1^2\mathbf{G}_1^0 & \bar{\mathbf{Z}}_1^0 - \bar{\mathbf{Y}}_1^0 & \mathbf{A}_1^0 \\ -\omega_2^2\mathbf{G}_2^0 & \bar{\mathbf{Z}}_2^1 - \bar{\mathbf{Y}}_2^0 & \mathbf{A}_2^0 \\ -\omega_3^2\mathbf{G}_3^0 & \bar{\mathbf{Z}}_3^2 - \bar{\mathbf{Y}}_3^0 & \mathbf{A}_3^0 \end{bmatrix}_{9N_n\times(6N_n+37N_e)}}_{\mathcal{G}_d} \underbrace{\begin{Bmatrix} \boldsymbol{\rho}_0 \\ \mathring{\mathbf{T}} \\ \mathbb{L}_0 \end{Bmatrix}_{(6N_n+37N_e)\times 1}}_{\mathcal{X}_d} = \underbrace{\begin{Bmatrix} \left\{\mathbf{F}_h^{ext}\right\}_1^0 \\ \left\{\mathbf{F}_h^{ext}\right\}_2^0 \\ \left\{\mathbf{F}_h^{ext}\right\}_3^0 \end{Bmatrix}_{9N_n\times 1}}_{\mathcal{B}_d} \tag{5.12}$$

or in short:

$$\mathcal{G}_d\mathcal{X}_d = \mathcal{B}_d \tag{5.13}$$

Eq. (5.13) is a least-squares problems that might have insufficient rank. Depending on the number of elements, N_e, three or four sets of perturbations are necessary to generate equal or larger number of equations as number of unknowns. Additional excitation at the vicinity of the forth natural frequency provides another set of equations.

5.3 Discussion

DERS, the developed method in this chapter, utilizes finite element capabilities to compute the residual stress tensors at each node, the local material density and local incremental elasticity tensors at each element. Displacement and force full-field measurements are required for three or more linear harmonic perturbations as inputs to DERS. Similar to the other methods (i.e., FEMU, CEGM, VFM, EGM, and RGM), where balance laws of mechanics are solved using a numerical technique, such as finite differences, boundary element and FEM, to determine material property parameters, RULFEM, ECSS and DERS methods forms a least-squares set of equation based on the finite element equilibrium formulation state solving the unknown vector. Except for VFM, RULFEM and ECSS, the other methods turns numerical form of the balance laws into an optimization problem with different cost functions. Contrary to previous methods (including VFM) DRES, ECSS and RULFEM directly forms and solves a least-squares set of equations without any *a priori* assumption on constitutive response of the material beyond harmonically linear response or incremental linearity. RULFEM computes the 9×9 elemental elasticity tensor ($\mathbb{C}^e$). ECSS

computes the current nodal stress tensors (CSS) and the 6×6 material incremental elasticity tensor ($\mathbb{L}^e$). Whereas, DRES computes the nodal residual stress tensors (RS), the 6×6 material incremental elasticity tensor ($\mathbb{L}^e$) and material density at each element. DRES, however, is only applicable to solid materials with low damping coefficient (elastically dominant solids). All of other methods, however, solve for the material constants of an *a priori* assumed constitutive model. Though, VFM does not solves an optimization problems to determine the material constants, it requires an optimized particular (virtual) displacement field to achieve acceptable accurate results.

DRES and ECSS yields the elemental incremental elasticity tensor, $\mathbb{L}^e$, which is a fourth order tensor with minor symmetry that can be represented with a 6×6 matrix. Whereas, RULFEM yields elemental $\mathbb{C}^e$, which is a fourth order tensor with no symmetry that can be represented with a 9×9 matrix. Hence, application of RULFEM to bodies with unknown stresses within the body at initial configuration results in erroneous elements of $\mathbb{C}^e$, since $\mathbb{C}_0\,[\mathbf{H}] = \mathbf{H}\overset{\circ}{\mathbf{T}} + \mathbb{L}_0\,[\mathbf{E}]$ [19, 28].

ECSS can compute the nodal Cauchy stress tensors of a body under any unknown internal or external loading. Residual stresses , which is the Cauchy stress tensors in the absence of the external forces, is a special case in which both ECSS and DRES can determine. The existing destructive (HDM, RCM, DHM, ST, CM, etc.) and nondestructive (X-ray, neutron diffraction, eddy current, ultrasound) stress or residual stress measurement techniques assume *a priori* knowledge of the material constitutive model of the body. Whereas, ECSS and DRES do not require any *a priori* knowledge or assumption of the material constitutive model of the body.

Similar ot ECSS, DRES method is not only a nondestructive method of determining the residual stress tensor field, but also an effective method to find the full material tensor distribution fields throughout the entire body. The destructive techniques, however, provide either local stress tensor fields, or bending and axial stress components only. While the nondestructive techniques are limited in depth and cannot measure stresses beyond $10\,cm$ depth [24]. The only disadvantage of ECSS and DRES method is that they require full-field displacement and force measurement throughout the entire mesh defining the body.

Similar to any inverse methods, RULFEM, ECSS and DRES have some limitations, which are (1) each finite element is made of a uniform material, (2) the force field measurements pose some practical challenges, and (3) the coefficient matrix might become rank deficient or have high condition number. The first limitation can be resolved by changing the mesh size and density if no clear distinction is found between materials. An easy solution to the third limitation is to measure additional perturbations, as discussed in previous section and shown in Example-1 in validation section of chapter 4, and/or use numerical preconditioning techniques to reduce the condition number of the coefficient matrix. Nonetheless, the second and third limitations can also be addressed in more detailed fashion as they are more involved, and hence, to be addressed further in our future work.

Another major benefit of DRES, ECSS and RULFEM is their speed in solving the linear algebraic problem yielding the desirable results. With current numerical and computation advancements, such as iterative methods, preconditioning and parallelization, solving a least-squares problem with severely sparse coefficient matrix is becoming cheaper and faster everyday.

Similar to ECSS, DRES address one of the main limitations of RUFEM, that is RULFEM

initiates perturbing the body from its presumably stress-free state, while ECSS and DRES have address this limitations. Moreover, DRES enjoys the freedom of FEA in meshing any geometry; hence, it can be applied to actual parts without any assumptions except each finite element is made of a uniform material with negligible damping properties.

5.4 Conclusion

A reverse updated Lagrangian finite element method, DRES, is developed capable of determining element-wise material density, mechanical properties of 3D solid bodies and the residual stress tensors at each nodes by dynamic perturbation of the body. Similar to RULFEM method [28] and ECSS (chapter 4), DRES formulation relies on the solution of a linear least-squares system of equations and yields element-wise, material density, the fourth-order incremental elasticity tensors and nodal stress tensors for linear harmonic displacement (or force) perturbations. The novelty of DRES is that it neither requires an *a priori* assumed material constitutive law, nor requires assuming stress-free configuration of the body in the absence of the external loading. DRES only assumes harmonic linearity of the deforming material and material uniformity within each element used to discretized the body. Due to similarity of ECSS and DRES, the validity of the method is not demonstrated. Since ECSS and RULFEM [28] are based on ULFEA, the local and global error prediction tools developed in [28] and chapter 3 are directly applicable to DRES.

Similar to RULFEM [28], the accuracy and efficiency of DRES depend on the accuracy and precision of the input displacement and force measurements. The accuracy of DRES strongly depends on the perturbation and efficacy of the measuring system to closely track the nodal displacements while the body is harmonically excited. The sensitivity of DRES is rooted in the high condition number of the coefficient matrix $\mathcal{G}_d$. The linearity of the perturbation can be tested directly by verifying the Eq. (2.7) inequality. If the body is harmonic excited in the vicinity of its natural frequencies, the orthogonality of the displacement eigenvectors (mode-shapes) minimizes the least-squares equations dependncy. Hence, DRES method is anticipated to be less sensitive to measurement errors and noise. However, the local and global error prediction tools as well as upper-bound error prediction developed in chapter 3 [28] are directly applicable to DRES.

Chapter 6

Conclusion and Future Directions

6.1 Conclusion

Part failure analysis under working conditions requires a detailed stress analysis, which requires accurate material constitutive laws and knowledge of the initial stress state. Standardized experiments are commonly used to determine the parameters of a material constitutive law, and a material constitutive model is selected by fitting the extracted data. Despite significant efforts of prestigious societies (e.g., ASME and ISO) to develop standardized testing protocols, unpredicted manufacturing and working conditions often give rise to additional stresses (residual stresses) in the absence of any external loading, which may lead to premature failure, even at part locations where stresses (strains) are not maximum.

Innovative methods have been developed to predict the true material properties of parts and residual stresses. Such methods have particularly been applied to biological tissues. Material structure complexity necessitates cumbersome mathematical treatments and measurement techniques. Avril et al. (2008) **??** developed a complete list of material identification methods, including (1) FEM updating method (FEMU), (2) constitutive equation gap method (CEGM), (3) virtual field method (VFM), (4) equilibrium gap method (EGM), and (5) reciprocity gap method (RGM). The governing equations in these methods are derived from the balance of linear momentum, the principle of virtual work, the Maxwell–Betti reciprocity principle, and the total potential energy principle, using standard numerical techniques, such as the FEM and finite differences method. A central commonality among these material identification methods is the *a priori* assumption of a constitutive model and the use of a numerical analysis of mechanical balance laws. Although these methods provide useful material parameter identification approaches, modeling assumptions imposed in the case of unknown or damaged materials entail a high degree of subjectivity and may yield biased results. All of the above mentioned methods rely on assumptions about the constitutive law that may not be optimal for the material under given conditions. Moreover, none of the existing methods provides a means of estimating the overall error. In fact, a systematic methodology to assess the selection of the constitutive model and the error in the predicted parameters due to measurement errors has yet to be developed. Except VFM, all the other methods use cost

functions, which may require extensive computational power to achieve the optimized solution. None of the existing methods, however, takes into account the state of stress field throughout the specimen body.

The RULFEM method developed in Chapter 3 3 **??** eliminates the need for an *a priori* presumed material constitutive model and furnishes material elasticity tensors for each finite element; however, RULFEM does not take into account the residual stresses of the body. The ECSS method developed in Chapter 4 is an improved version of the RULFEM, which yields the residual stresses at all nodes of the finite element mesh. Both RULFEM and ECSS require full-field displacement and force data obtained from (pseudo)static perturbations, assuming incrementally linear material behavior and uniform material elements with elasticity characteristics independent of neighboring finite elements.

A large number of engineering materials exhibit predominantly elastic responses under working conditions, that is, their viscoelastic or damping response is negligible. Dynamic testing, such as modal analysis, shaker table testing, etc., are used to measure material parameters. The DRES method introduced in Chapter 5 is an extension of the ECSS method and assumes linear harmonic response of the body. This method determines the material density and incremental elasticity tensor of each finite element used to discretize the body and nodal residual stress tensors.

The two general stress measurement techniques are categorized as constructive and nonconstructive. Figures 1.2 and 1.7 provide a summary of all existing techniques and their capabilities. To this end, there are no destructive or nondestructive methods that can yield the residual stress tensors throughout the entire body. However, the ECSS and DRES methods introduce two nondestructive methods for determining the stress tensors throughout the entire solid body regardless of material and geometrical shape complexities or the stress history. A summary of the capabilities of the material identification models and residual stresses techniques is given in Table 6.1.

The methods developed in this thesis (i.e., RULFEM, ECSS, and DRES) construct a linear least-squares set of equations. However, the finite element mesh, the geometry, and, most importantly, the similarity of the perturbations may cause the coefficient matrix of the least-squares equation to become ill-conditioned (i.e., high condition numbers). Therefore, local and global upper bound errors were introduced to assess the accuracy of each method. These assessment tools provide directions to design additional perturbations, furnishing a set of equations that improve the condition number of the coefficient matrix. Hence, more accurate results can be achieved without the need to improve the measurement accuracy.

Full-field 3D displacement and traction force measurements may pose practical challenges; hence, full-field measurements might be considered a common limitation of RULFEM, ECSS, and DRES. Consequently, a general framework for inverse finite element problems was developed and validated, which can be extended to thin bodies acting as 2D solids where the full-field data become attainable on the solid surfaces.

Methods		Existing ID Methods		Residual Stress Methods		Present developed methods		
Capabilities and Limitations		VFM	Others	Destructive	Nondes.	RULFEM	ECSS	DERS
Material Model	Parameters				✓	None	None	None
	Constitutive model required	✓	✓	✓		None	None	None
Complex geometry				✓	✓	✓	✓	✓
Requires certain specimen shape		✓	✓					
Solves optimization problem								
Requires virtual displacement field		✓						
Displacement field	Full-field	✓	✓			✓	✓	✓
	Partial-field	✓	✓	✓				
Traction/force field	Full-field					✓	✓	✓
	Partial or local -field	✓	✓	✓				
Solves optimization problem			✓					
Least-squares or linear system of equations						✓	✓	✓
Performance		moderate	slow	moderate	fast	fast	fast	fast
Material density								✓

Table 6.1: Qualitative Table of Reverse Methods

6.2 Future Directions

The RULFEM method may produce coefficient matrices with higher condition numbers compared to the ECSS and DERS methods. Despite the error assessment tools adapted, explained, and employed in Chapter 3 3, application of other beneficial numerical tools and techniques are yet to be explored for solving least-squares set of equations with poor condition number. For instance, the condition number can be improved, often significantly, by generating proper preconditioning matrices [26].

The size of the linear least-squares systems in RULFEM is equal to the total DOFs of the system. This can become very large for bodies with large mesh densities. The size of the system of equations becomes three or four times the total system DOFs in the ECSS and DERS methods. Sequential direct methods are not proper solution techniques for large systems of equations. Hence, the multigrid iterative method shall be studied, tested, and selected for these finite element-based systems of equations.

Moreover, proper experiments must be designed to validate the developed methods experimentally and compare them with existing leading methods. Biological tissues can exhibit nonlinear responses and 3D imaging is possible by means of magnetic resonance imaging (MRI) techniques. Thus, the current ECSS and RULFEM methods can be validated using other experimental techniques and tissue slitting.

Full-field displacement measurement in thick materials, depending on the material, can be acquired using X-ray or special MRI (Magnetic Resonance Imaging) techniques) sequence, known as DENSE MR, for non-metallic components.

Bibliography

[1] S. Avril, M. Bonnet, A. Bretelle, M. Grédiac, F. Hild, P. Ienny, F. Latourte, D. Lemosse, S. Pagano, E. Pagnacco, et al. Overview of identification methods of mechanical parameters based on full-field measurements. *Experimental Mechanics*, **48**(4):381–402, (2008).

[2] S. Avril and F. Pierron. General framework for the identification of constitutive parameters from full-field measurements in linear elasticity. *International Journal of Solids and Structures*, **44**(14):4978–5002, (2007).

[3] K. J. Bathe, E. Ramm, and E. L. Wilson. Finite element formulations for large deformation dynamic analysis. *International Journal for Numerical Methods in Engineering*, **9**(2):353–386, (1975).

[4] M. P. Blodgett and P. B. Nagy. Eddy current assessment of near-surface residual stress in shot-peened nickel-base superalloys. *Journal of nondestructive evaluation*, **23**(3):107–123, (2004).

[5] D. J. Buttle, C. B. Scruby, G. A. D. Briggs, and J.P. Jakubovics. The measurement of stress in steels of varying microstructure by magnetoacoustic and barkhausen emission. *Proceedings of the Royal Society of London. A. Mathematical and Physical Sciences*, **414**(1847):469–497, (1987).

[6] S. Chandrasekaran and I. C.F. Ipsen. On the sensitivity of solution components in linear systems of equations. *SIAM Journal on Matrix Analysis and Applications*, **16**(1):93–112, (1995).

[7] M. Daymond and L. Edwards. Scientific review: Engin-x: A fully refined diffractometer designed specifically for measurement of stress. *Neutron News*, **15**(1):24–29, (2004).

[8] Buschow K.H.J. (Ed.) et al. Dobmann G. *Encyclopedia of materials: science & technology*. Elsevier: Oxford, (2001).

[9] M. Grédiac and F. Pierron. Applying the virtual fields method to the identification of elasto-plastic constitutive parameters. *International Journal of Plasticity*, **22**(4):602–627, (2006).

[10] M. Grédiac, E. Toussaint, and F. Pierron. Special virtual fields for the direct determination of material parameters with the virtual fields method. 2—-application to in-plane properties. *International Journal of Solids and Structures*, **39**(10):2707–2730, (2002).

[11] A. Hoger. Positive definiteness of the elasticity tensor of a residually stressed material. *Journal of elasticity*, **36**(3):201–226, (1994).

[12] G. A. Holzapfel and R. W. Ogden. Constitutive modelling of passive myocardium: a structurally based framework for material characterization. *Philosophical Transactions of the Royal Society A: Mathematical, Physical and Engineering Sciences*, **367**(1902):3445–3475, (2009).

[13] G. A. Holzapfel and R. W. Ogden. Modelling the layer-specific three-dimensional residual stresses in arteries, with an application to the human aorta. *Journal of the Royal Society Interface*, page rsif20090357, (2009).

[14] M. T. Hutchings, P. J. Withers, T. M. Holden, and T. Lorentzen. *Introduction to the characterization of residual stress by neutron diffraction*. CRC Press, (2004).

[15] T. R. Hyde, J. T. Evans, and B. A. Shaw. Effect of stress and heat treatment on magnetic barkhausen emission in case carburized steels. *Materials evaluation*, **58**(8):985–990, (2000).

[16] M. Ikehata. Inversion formulas for the linearized problem for an inverse boundary value problem in elastic prospection. *SIAM Journal on Applied Mathematics*, **50**(6):1635–1644, (1990).

[17] M. R. Labrosse, E. R. Gerson, J. P Veinot, and C. J. Beller. Mechanical characterization of human aortas from pressurization testing and a paradigm shift for circumferential residual stress. *Journal of the mechanical behavior of biomedical materials*, **17**, pages=44–55, year=(2013), publisher=Elsevier.

[18] P Ladevèze, D Nedjar, and M Reynier. Updating of finite element models using vibration tests. *AIAA journal*, **32**(7):1485–1491, (1994).

[19] C. S. Man and D. E. Carlson. On the traction problem of dead loading in linear elasticity with initial stress. *Archive for rational mechanics and analysis*, **128**(3):223–247, (1994).

[20] J. T. Oden. *Finite elements of nonlinear continua*. Courier Dover Publications, (2006).

[21] E. Pagnacco, D. Lemosse, F. Hild, and F. Amiot. Inverse strategy from displacement field measurement and distributed forces using fea. In *2005 SEM annual conference and exposition on experimental and applied mechanics, Portland*, pages 7–9, (2005).

[22] M. B. Prime. The contour method: a new approach in experimental mechanics. In *Proceedings of the SEM Annual Conference. Albuquerque, NM, USA*, (2009).

[23] E. K. Rodriguez, J. H. Omens, L. K. Waldman, and A. D. McCulloch. Effect of residual stress on transmural sarcomere length distributions in rat left ventricle. *American Journal of Physiology*, **264**:H1048–H1048, (1993).

[24] N.S. Rossini, M. Dassisti, K.Y. Benyounis, and A.G. Olabi. Methods of measuring residual stresses in components. *Materials & Design*, **35**:572–588, (2012).

[25] A. Shabana. *Vibration of discrete and continuous systems*, volume **2**. Springer, (1997).

[26] J. R. Shewchuk. An introduction to the conjugate gradient method without the agonizing pain, (1994).

[27] M. Takaza, K. M. Moerman, J. Gindre, G. Lyons, and C. K. Simms. The anisotropic mechanical behaviour of passive skeletal muscle tissue subjected to large tensile strain. *Journal of the mechanical behavior of biomedical materials*, **17**:209–220, (2013).

[28] M. Tartibi, D.J. Steigmann, and K. Komvopoulos. A reverse updated lagrangian finite element formulation for determining material properties from measured force and displacement data. *Computational Mechanics*, **54**(6):1375–1394, (2014).

[29] N Tebedge, G Alpsten, and L Tall. Residual-stress measurement by the sectioning method. *Experimental Mechanics*, **13**(2):88–96, (1973).

[30] R. N. Vaishnav and J. Vossoughi. Residual stress and strain in aortic segments. *Journal of biomechanics*, **20**(3):235–239, (1987).

[31] T. Waffenschmidt and A. Menzel. Extremal states of energy of a double-layered thick-walled tube–application to residually stressed arteries. *Journal of the mechanical behavior of biomedical materials*, **29**:635–654, (2014).

[32] H. M. Wang, X. Y. Luo, H. Gao, R. W. Ogden, B. E. Griffith, C. Berry, and T. J. Wang. A modified holzapfel-ogden law for a residually stressed finite strain model of the human left ventricle in diastole. *Biomechanics and modeling in mechanobiology*, **13**(1):99–113, (2014).

[33] P.J. Withers. Residual stress and its role in failure. *Reports on Progress in Physics*, **70**(12):2211, (2007).

[34] P.J. Withers and H.K.D.H. Bhadeshia. Residual stress. part 1–measurement techniques. *Materials science and Technology*, **17**(4):355–365, (2001).

[35] P.J. Withers, M. Turski, L. Edwards, P.J. Bouchard, and D.J. Buttle. Recent advances in residual stress measurement. *International Journal of Pressure Vessels and Piping*, **85**(3):118–127, (2008).